Università degli Studi di Padova
Dipartimento di Ingegneria Industriale

Master's degree in
Chemical and Process Engineering

Exploring the strength of wet granular materials via dynamic ball indentation

Supervisor Prof. Andrea Claudio Santomaso
Dipartimento di Ingegneria Industriale

Co-supervisor Prof. Erica Franceschinis
Dipartimento di Scienze del Farmaco

Graduating student Lorenzo Schiavo
Matriculation number 2121753

Academic year 2024/2025

Abstract

The aim of this work is to validate the applicability of the Dynamic Ball Indentation (DBI) technique to the study of wet powder dynamics. Up to now, this method has been applied only to dry powders in initial studies.

This work is divided in two main parts. The first, and core one, is focused on the study of wet pharmaceutical powders, with the goal of identifying the key variables and dimensionless groups governing the mechanical response of partially saturated powders under the indenter stress. The second part, extend the state of the art in the application of DBI to dry powders, retrieving the flow functions of 9 different powders relying solely on data from DBI.

For wet powders, DBI successfully reproduced classical trends from literature, such as the identification of flow regimes based on the inertial number (I) and the analytical relationship between the dimensionless strength (Str^*) and the capillary number (Ca), validating its applicability to partially saturated systems. Furthermore the classical relationship between Str^* and Ca has been expanded by accounting for inertial effects through the inertial number, leading to an excellent data collapse onto a master curve described by Str^* as a function of $I^{0.8} \cdot Ca^{0.13}$.

For dry powders, a new definition of the constraint factor C has been proposed, based on the theoretical definition of flowability. This formulation allows the flow function of a powder to be derived directly from indentation data. The proposed C definition was first validated against the classical one, and then used to derive flow functions, which were compared with reference shear cell results. The DBI-based classification matched the benchmark in 7 out of 9 cases, with minor discrepancies in the remaining two.

In conclusion DBI is a novel method with highly promising features, its ability to study both wet and dry powder makes it unique. Moreover, the newly proposed definition of Str^*, integrating capillary and inertial effects, opens promising directions for quantitative prediction of wet powder behavior. Future work should aim to refine the apparatus and compaction protocol, establish quantitative correlations between hardness and torque rheometry, and further validate both the analytical relationship between Str^* and $I^{0.8} \cdot Ca^{0.13}$ and the DBI-derived method for flow functions characterization.

Contents

Introduction

Particulate materials are defined as systems made of large numbers of macroscopic particles, whose rheological properties are determined both by the physical nature of the material and by the unique characteristics of the single units.

They are fundamental in many industrial processes, especially within the pharmaceutical, chemical, and food industries, but they are difficult to handle and to process.

Particle size enlargement techniques can help in dealing with powder materials, they are used in almost every processing industry which works with particulate feeds, intermediates or products.

There are many reasons why we may wish to increase the mean size of a product or intermediate. These include reduction of dust hazard (explosion hazard or health hazard), reduce caking and lump formation, to improve flow properties, increase bulk density for storage, creation of non segregating mixtures of ingredients of differing original size, to provide a defined metered quantity of active ingredient (e.g. pharmaceutical drug formulations), and control of surface to volume ratio (e.g. in catalyst supports), (Rhodes, 2008).

Size enlargement can be divided into two categories:

- Granulation: it uses a liquid binder to form interparticle bonds. This class of processes include fluidized beds, tumbling drums and mixer granulators.
- Compression: use pressure to promote interparticle bonds. This type of processes are usually performed dry. If liquid is added is to promote powder flow. In this class of processes there are roll pressing, extrusion and tabletting.

Granulation processes are inherently complex to understand, as they are rate dependent phenomena in which multiple competing mechanisms occur simultaneously. These are (Litster & Ennis (2004)):

1. wetting, nucleation and binder distribution;
2. consolidation and growth;
3. attrition and breakage.

Predicting the outcomes of granulation processes is inherently challenging, because they depend in a lot of parameters.

Models capable of describing the rate processes are of great interest, as they provide a deeper understanding of the mechanisms occurring during granulation and help anticipate the nature and quality of the resulting granules.

Scope and objectives

The scope of this thesis is investigating the mechanical response of wet granular powders under dynamic loading conditions.

The dynamic loading aim to express in a more representative way what can be the stress that the powder is subjected to in high shear wet granulator.

Although it is known that capillary bridges are responsible for the cohesion in wet powders, we are looking for a predictive link between microscopic physical properties, such as binder viscosity, surface tension and particle size to the macroscopic strength of wet compacts, some studies has been already completed on this topic, but here a new characterization technique is used: the dynamic ball indentation.

The ultimate objective is to establish an empirical relationship between the measured dynamic strength and a dimensionless number that characterizes the system, this will help to predict the granulation behavior of powders in high shear wet granulators.

Structure of the thesis

This thesis is organized into five chapters.

Chapter 1 provides the theoretical background and literature review necessary to understand the framework of this work.

Chapter 2 describes the materials employed and the experimental methods used to characterize the properties of powders and binders.

Chapter 3 represents the core of the thesis, focusing on the analysis of dynamic indentation experiments on wet powders and comparing the results with established benchmark techniques.

Chapter 4 deals with the characterization of dry powders, where indentation experiments are compared with shear cell results. Although this was not the main scope of the thesis, the findings were noteworthy and are therefore reported.

Finally, the conclusions are summarized, followed by appendices, lists of symbols, figures, and tables, and the bibliography.

Chapter 1

Background and theoretical framework

1.1 Basics of powder flow and strength

In powder systems, most properties, such as size, shape, surface roughness, and even surface energy can vary significantly from particle to particle. This inherent heterogeneity means that interparticle interactions are not characterized by a single value, but rather by a distribution of properties, (Goh et al., 2018).

The mechanical behavior of particles is strongly influenced by the interaction between individual particles and fluids if they are present.

When the interparticle forces become stronger than external forces such as gravity, the behavior of the powder changes significantly and they begin to exhibit cohesive behavior, becoming "mutually sticky."

In dry systems, the dominant interparticle forces are typically Van der Waals interactions and, in some cases, electrostatic forces.

Humidity can significantly alter powder behavior by promoting capillary bridges between particles, increasing cohesion and sometimes leading to poor flow.

1.2 Forces acting in partially saturated powders

The mechanical behavior of partially saturated powders is governed by a complex interplay of forces that arise due to the simultaneous presence of solid particles and an interstitial liquid phase. As soon as a small amount of liquid is added to a dry powder,

new interactions emerge between particles, altering the system's cohesion, flowability, and response to external stresses.

These interactions are not only determined by the solid phase characteristics (such as particle size, shape, and surface roughness), but also strongly influenced by the distribution, amount, and physicochemical properties of the liquid phase. Understanding these forces is essential for interpreting and predicting the macroscopic behavior of wet granular materials in processes such as granulation, agglomeration, powder compaction, and additive manufacturing.

In general, the dominant contributions to the interparticle force network in partially saturated systems can be categorized into three main types:

1. Frictional forces due to direct contact and relative motion between solid surfaces;
2. Capillary and surface tension forces, arising from the formation of liquid bridges at the particle contacts;
3. Viscous forces resulting from the flow of liquid within the narrow gaps or bridges between particles during deformation or rearrangement.

The first two are interrelated, since the tensile force of the liquid bridge acts to pull particles together and this normal force at particle contacts activates interparticle friction. Surface tension and capillary forces always act to pull particles together. Frictional and viscous forces are dissipative, always acting against interparticle motion. The complex interdependence of these different forces means that it is often impossible to predict a priori the effect of changing any particular granule or binder property.

Each of these forces plays a distinct role, whose relative impact depends on the wetting regime, particle properties, liquid properties, and the external loading conditions applied during processing. In the following sections, each force contribution is discussed in detail.

1.2.1 Interparticle friction

Internal friction in a granular body is in general described using the Coulomb relationship.

$$\tau = \mu_f \sigma + c \tag{1.1}$$

where τ is the shear stress at failure, σ is the normal stress and μ_f and c are respectively the coefficient of internal friction and the powder cohesion.

In an ensemble of particles as found in a granule, resistance to shear deformation arises from true tribological interaction between touching particles, and also particle interlocking. Particle interlocking is a macroscopic feature of the packing of particles and will depend on size and shape distribution.

It has been shown that the presence of lubricating films will lower friction at particle and macroscopic levels (Cain et al., 2000). It would be expected that this would occur in the presence of a binder. In the present context, the important features of internal friction in a granular body are that it is dissipative and not strongly strain-rate dependent at strain rates commonly experienced in granulation processes.

1.2.2 Liquid bridges and capillary cohesion

The main cohesive force acting in partially saturated powders is related to the formation of liquid bridges between adjacent particles. These liquid bridges, typically generated during wet granulation or under ambient humidity conditions, introduce attractive forces that significantly influence the mechanical behavior of the powder bed.

Capillary forces have origins on thermodynamics. A basic principle in thermodynamic is that system tend to evolve in configurations that minimize their free energy, achieving a stable equilibrium.

In a biphasic systems, such as liquid in contact with air, molecules in the bulk of the liquid experience attractive forces in all direction, that lead to a low energy state. In the other hand particles at the interface, are not completely surrounded by neighbors, generating unbalanced forces, (Figure 1.1), that lead to a higher energy state.

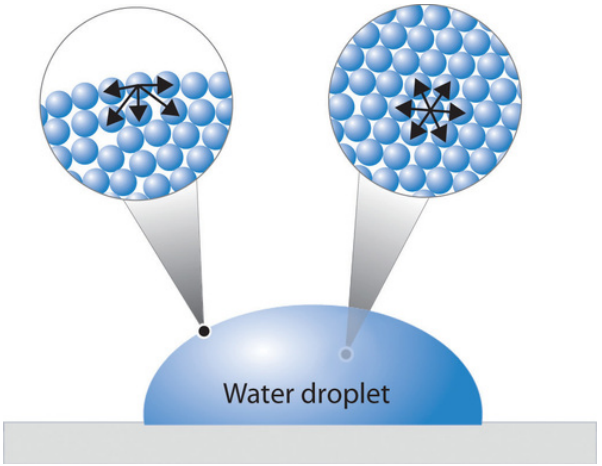

FIGURE 1.1: Unbalanced forces at liquid vapour interface

The surface tension is a contractive force that act on the surface of the liquid, tending to minimize the molecules at the interface in order to reach a lower energetic state.

Surface tension allows the liquid to resist external disturbances such as gravity, and it plays a crucial role in the formation and strength of liquid bridges that hold particles together in wet powders.

There are two complementary definitions of surface tension, an operative and a thermodynamic one.

The operative definition define surface tension as the force per unit length acting along the surface of a liquid (Fig.1.2).

$$F = 2\gamma L \rightarrow \gamma = \frac{1}{2}\frac{F}{L} \tag{1.2}$$

In expression 1.2 the coefficient 2 is due to the fact that the film of liquid has two surfaces.

FIGURE 1.2: Surface tension definition's geometry

The thermodynamic definition, describe surface tension as the amount of work required to increase the surface area by one unit.

$$dW = 2\gamma dA \rightarrow \gamma = \frac{1}{2}\frac{dW}{dA} \tag{1.3}$$

Surface tension can be interpreted also as the excess Gibbs free energy per unit area at the interface between two phases, and so can be calculated as: $\gamma = (\frac{\partial G}{\partial A})_{T,P,n_j}$ where T, P, and n_j refers to constant temperature, pressure and the total number of moles of the j component, (Navascues, 1979).

The generation of this contractive force is described by the Young-Laplace's equation, that for simple surface geometries can be written as:

$$\Delta P = k\frac{\gamma}{R} \tag{1.4}$$

where k is a parameter that depends on the geometry and number of interfaces (e.g. $k = 4$ for a soap bubble or $k = 2$ for a liquid droplet or gas bubble immersed in a liquid).

In our cases, we are more interested on a catenoid like geometry (Fig.1.3) because the capillary bridges that forms between powder particles have approximately this shape, in such cases the Young-Laplace's equation became:

$$\Delta P = \gamma\left(\frac{1}{R_1} + \frac{1}{R_2}\right) \tag{1.5}$$

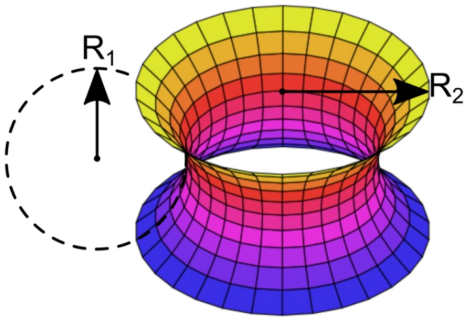

FIGURE 1.3: Catenoid geometry

The strength of pendular liquid bridges has been the subject of an extensive number of theoretical and experimental studies, it consist on three components, (Iveson et al., 2002):

1. surface tension at the contact line between the liquid and solid;
2. hydrostatic force due to the capillary suction pressure generated by the curvature of the liquid profile;
3. buoyancy forces due to the partial submersion of the solid in the liquid phase.

.

Surface tension strongly contributes to the wettability of solid surfaces by a liquid, there are multiple wetting mechanisms, like spreading, capillary rise, immersional, and condensational wetting, (Lazghab et al., 2005).

Each mechanism may dominate depending on the application context, for example, capillary rise is central in powder agglomeration, while spreading is more relevant in coating processes. In the following subsections, each mechanism is discussed in detail.

1.2.2.1 Spreading mechanism

Spread wetting refers to the process by which a liquid droplet expands over the surface of a solid substrate. A classical and widely adopted model to describe this phenomenon

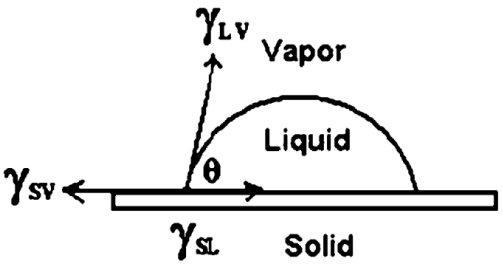

FIGURE 1.4: Sessile drop spread wetting

is the sessile drop method. In this framework, a liquid drop is gently deposited on a horizontal, ideally flat, chemically homogeneous, and smooth solid surface exposed to the surrounding vapour phase. Upon deposition, the droplet assumes the shape of a spherical cap, constrained by the so-called three-phase contact line, which marks the boundary between the solid, liquid, and vapour phases.

As the droplet spreads, the contact line advances over the solid surface, displacing the solid–vapour interface. The angle formed at any point along this three-phase boundary is known as the contact angle, spreading proceeds until an equilibrium contact angle is reached, typically denoted by θ, (Fig.1.4).

At this point, a balance is established between the cohesive forces within the liquid, which favor retention of the spherical shape, and the adhesive forces between the liquid and the solid, which promote spreading.

The force balance (at equilibrium) is described by the Young-Dupre equation:

$$l \cdot \gamma_{SV} = l \cdot \gamma_{LV} \cdot \cos\theta + l \cdot \gamma_{LS} \tag{1.6}$$

where $\gamma_{SV}, \gamma_{SL}, \gamma_{LV}$ represents in order, the surface tension between solid-vapour, solid-liquid and liquid-vapour phases, l is the length of the three-phase contact line (it will cancels out on both sides), while $\cos\theta$ describe the wettability of the liquid-solid system. Four cases are possible, depending on θ:

1. $\theta = 0$ complete wettability, means that the liquid spread completely on the surface
2. $0 < \theta < 90$ good wettability
3. $90 < \theta < 180$ poor wettability
4. $\theta = 180$ non wettability, this happen in system where the interaction between liquid and solid are very poor, usually when liquid has a high surface tension

meaning that the lowest energy state is reached when the liquid drop remains in a spherical form (e.g. mercury drop on glass surface).

In eq.1.6, γ_{SL} and γ_{SV} are difficult to be measured.

An alternative and easier equation is the Antonow and Berthelot equation:

$$\cos\theta = 2\frac{\gamma_{SV}}{\gamma_{LV}} - 1 \tag{1.7}$$

where the dependence on γ_{SL} is removed, furthermore γ_{SV} can be extrapolated at $\cos(\theta) = 1.0$ from the Zisman plot, an example of it is shown in Fig.1.5.

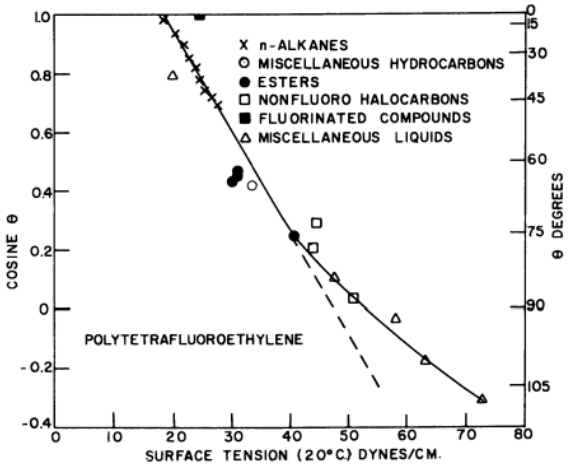

FIGURE 1.5: $\cos\theta$ vs γ_{SL} of various liquid spreaded on PTFE, (Zisman, 1964)

.

1.2.2.2 Capillary rise mechanism

Capillary rise is a classical phenomenon that occurs when a liquid spontaneously ascends inside a narrow tube or porous medium due to intermolecular interactions. In granular systems, this mechanism governs the migration of binder liquid into pores and interstices between particles, which directly influences the formation of capillary bridges and the strength of wet agglomerates.

The driving force behind capillary rise is the balance between surface tension, adhesive forces between the liquid and the solid, and gravitational forces acting on the liquid column.

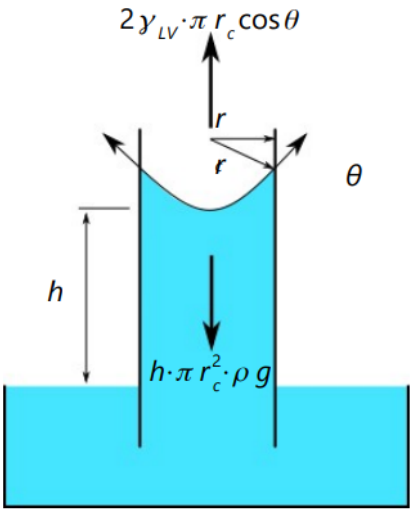

FIGURE 1.6: Capillary geometry

Using the notation in Fig.1.6, the capillary rise can be retrieved at equilibrium using the first newton law, $F_{cz} = F_g$, where F_{cz} is the capillary force acting along the z direction,

$$F_{cz} = \Delta P A_c = \frac{2\gamma_{LV}}{r}\pi r_c^2 \tag{1.8}$$

the curvature radius r is related to the capillary radius, $r\cos\theta = r_c$, substituting the latter in eq.1.8, the following equation is obtained

$$F_{cz} = 2\gamma_{LV}\pi r_c \cos\theta \tag{1.9}$$

substituting this in the force balance, and expanding F_g, we get

$$2\gamma_{LV}\pi r_c \cos\theta = h\pi r_c^2 \rho g \tag{1.10}$$

and the capillary rise h is retrieved

$$h = \frac{2\gamma_{LV}\cos\theta}{r_c \rho g} \tag{1.11}$$

The extent of capillary rise is strongly influenced by the mutual chemical nature of the liquid and the solid; for example, polar liquids tend to rise more effectively in polar solids due to stronger adhesive interactions, while poor wetting occurs in polar–apolar combinations.

1.2.2.3 Immersional mechanism

Immersional wetting refers to the phenomenon that occurs when a solid surface is progressively immersed into a liquid. Unlike spreading or capillary rise, which involve horizontal motion of the liquid across or into the solid, immersional wetting considers vertical interaction, where the solid penetrates the liquid phase, displacing it and generating a new solid–liquid interface.

The immersional process is made of different stages:

1. Wetting and sinking
2. Immersion
3. Dispersion and/or dissolution

In the sinking stage the solid–vapour interface disappears,while at the same time a new solid–liquid interface is created.

When the surface tension of the liquid is overcome by the solid, the particle continues to submerge into the liquid. This transition indicates that the interactions between the solid and the liquid are stronger than the cohesive forces within the liquid itself. As a result, the system minimizes its interfacial energy by promoting immersion.

The sinking condition is that $F_{cz} < F_g$. At equilibrium, assuming a spherical particle, and considering the instant just before the interface rupture, the balance become $F_{cz} = F_g$ By expanding both terms and assuming complete wettablity ($\theta = 0$) at this stage, the following expression is retrieved,

$$\gamma_{LV}\pi d_{crit} = V\rho g = \frac{\pi}{6} d_{crit}^3 \rho g \tag{1.12}$$

From this relationship, the critical particle diameter leading to sinking can be derived as,

$$d_{crit} = \sqrt{\frac{6\gamma_{LV}}{\rho g}} \tag{1.13}$$

1.2.2.4 Condensational (or adsorptive) wetting

Condensational wetting concerns the adsorption of vapour on the solid substrate. Adsorption can proceed until the formation of drops or a continuous liquid film. Generally, higher rates of vapour adsorption on the solid surface lead to better wetting. When a solid, initially in vacuum, is covered with a liquid film in equilibrium with saturated

vapour p°, the associated free energy change is given by:

$$\Delta G_{ads} = \gamma_S - \gamma_{SL}$$

In this equation, γ_S is the solid surface energy in vacuum, which differs from the surface tension for a solid in equilibrium with a vapour. In fact, when the solid is covered with a layer of vapour, its surface free energy γ_{SL} is reduced. This reduction in surface energy is taken into account by the concept of an equilibrium spreading pressure, Π, such that when the vapour obeys the ideal gas law we have:

$$\Pi = \gamma_S - \gamma_{SL} = RT \int_0^{pv_e} \Gamma d(\ln p_v)$$

where p_v is the vapour pressure, p_{ve} is the equilibrium vapour pressure, R is the gas constant, T is the absolute temperature and Γ is the surface concentration of adsorbed vapour. This equation is often referred to as the Gibbs adsorption equation. Generally, Π is directly related to the affinity of a solid with respect to a liquid and is a good measure of this affinity, (Lazghab et al., 2005).

1.2.3 Viscous force

The third contribution in the interparticle force network in partially saturated systems, is due to the introduction of the liquid phase that leads to the formation of capillary bridges between adjacent particles. When particles move relative to each other, the viscous resistance of the liquid within these bridges contributes significantly to the overall mechanical response of the system, especially under dynamic loading conditions.

A common approach to estimate the viscous force arising during axial stretching or compression of a liquid bridge between two spherical particles is based on lubrication theory. Assuming a pendular bridge configuration and asymmetric flow, the viscous force F_V can be estimated

$$F_V = \frac{3\pi\eta a^2}{2h}\left(\frac{dh}{dt}\right) \tag{1.14}$$

where

- η is the liquid viscosity;
- a is the harmonic mean particle radius ($1/a = 1/a_1 + 1/a_2$);
- $2h$ is the gap between two particles;

- $\frac{dh}{dt}$ is the time derivative of h, the velocity of approach or separation between the particles.

This expression captures the resistance to axial motion due to viscous flow within the thin liquid film and has been experimentally validated for small gaps between particles.

Liquid bridges will also have a viscous resistance to shear as well as to axial strain. Again, there is no rigorous analytical solution for this shear strength, but using lubrication theory the following relationship may be derived for sufficiently small separation distances

$$F_V = 6\pi\eta a\nu_t \left[\frac{8}{15}\ln\left(\frac{a}{2h}\right) + 0.9588\right] \tag{1.15}$$

where where ν_t is the relative velocity of the two spheres.

Equation 1.15 has not been well verified, (Iveson et al., 2002; Goldman et al., 1967).

Although this second formulation lacks comprehensive experimental validation, it is worth noting that both expressions exhibit a clear linear dependence on the liquid viscosity, η, underlining its role as a key parameter for viscous energy dissipation in wet granular systems.

1.2.4 Mechanical consequences of partial saturation

Since now, the behavior of single powder particles with binder has been investigated, now the binder effect on the bulk powder is presented.

The mechanical behavior of the bulk is strongly affected by the presence of liquid.

As the degree of saturation increases, the morphology and connectivity of the liquid phase evolve, leading to distinct regimes that influence interparticle cohesion and the macroscopic strength of the powder bed.

Liquid saturation (S) is defined as:

$$S = \frac{w\rho_s(1-\mathcal{E}_{pore})}{\rho_l \cdot \mathcal{E}_{pore}} \tag{1.16}$$

Where

- w is the ratio between liquid and solid mass;
- ρ_s is the solid density;
- ρ_l is the liquid density;
- $\mathcal{E}_{pore}$ is the bed porosity.

As granule saturation increases, the structure of the liquid phase within the pores changes according to four characteristic wetting regimes, represented in Figure 1.7:

a. At low saturation, at the so called pendular state, particles are held together by isolated liquid bridges at their contact points; the majority of pore space remains filled with air.

b. As saturation increases, the system enters the funicular state, a transition regime between the pendular and capillary states, in which some pores are filled with liquid while others remain partially filled.

c. In the capillary state, all voids are fully saturated with liquid, and surface liquid is drawn back into the pore space due to capillary action.

d. At high saturation (droplet or slurry state), excess liquid accumulates outside the pore network, and particles are suspended within or attached to free liquid droplets.

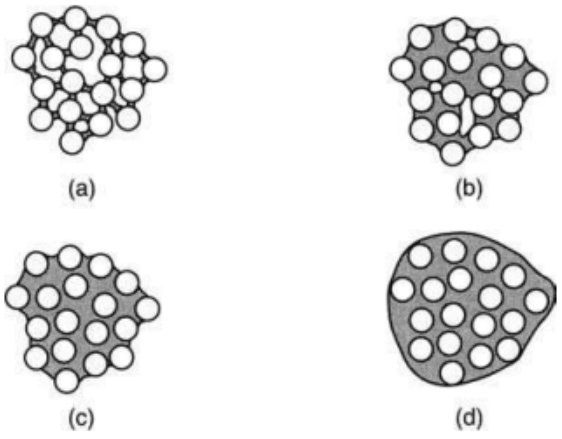

FIGURE 1.7: Wetting regimes

These regimes are fundamental in wet granulation processes. The binder content is an important variable, upon which depends the final product characteristics.

The optimal binder concentration typically corresponds to the one of the funicular state, where sufficient interparticle liquid promotes aggregation without overwetting. During granulation, particle rearrangement and consolidation tend to squeeze the bulk, reducing pore volume, increasing local saturation. If the process starts already in the capillary state, consolidation may push the system into the droplet state, resulting in a slurry like, overwet mass, that generally must be avoided.

In order to know which is the optimal binder quantity, a well known method is the mixer torque rheometer. This tool allows to measure the torque needed to mix a powder varying the liquid content in it, and by calculating the second derivative of the torque profile is possible to understood the optimal L/S ratio to granulate (corresponding to the funicular regime).

1.2.5 Consolidation and growth

As explained in the introduction, granulation is a complex operation, composed by a wide range of rate dependent phenomena, each one is difficult to be understand and modeled. This work is mainly focused on variables affecting the consolidation and growth step, crucial because usually defines the final granule properties.

Many different type of growth behavior have been observed, and so a lot of corresponding macroscopic mechanisms have been proposed, however the general behavior can be understood by answering the question. Will two granules which collide in the granulator stick together or rebound?

In general is not possible yet to predict quantitatively the mechanical behavior of the powder assembly. Instead the granule is considered as an elastic-plastic solid.

After a compression, energy is firstly stored as elastic deformation, that can be recovered if the load is removed, but once the dynamic yield stress is reached the assembly deform plastically.

The main properties that determines the behaviour of granules on impact are its elastic modulus E and the dynamic plastic yield stress Y.

There are several complications, to this simple model, firstly the dynamic yield stress is probably strain rate dependent,(Fig.1.8(b)), secondly the assembly may strain harden or strain weaken, (Fig.1.8(c)): strain hardening refers to the increase in resistance to deformation as the material is progressively loaded, typically due to enhanced particle interlocking or compaction. In contrast, strain weakening describes a reduction in resistance with continued deformation, which may arise from structural rearrangements.

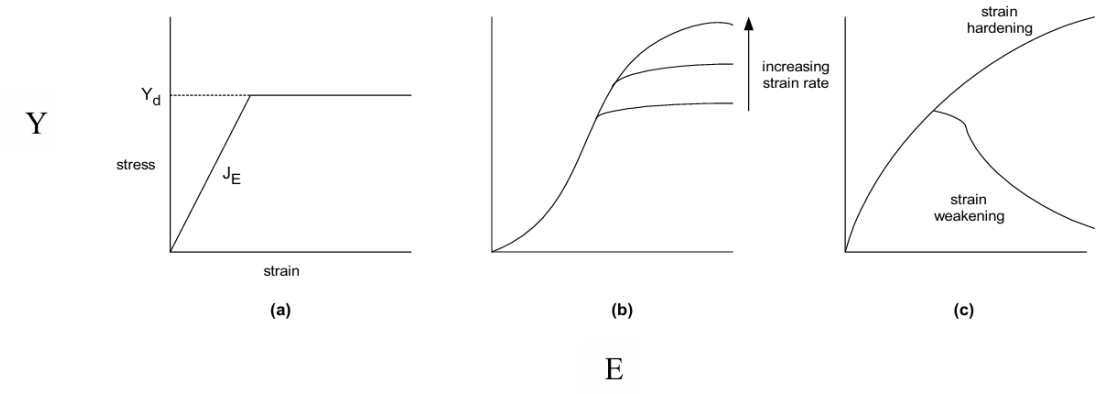

FIGURE 1.8: Possible granule stress-strain behaviours (a) Simple elastic-plastic solid, (b) with strain rate dependent yield stress, (c) with strain hardening or strain weakening (Litster & Ennis, 2004)

.

During a collision between particles or between a particle and a piece of equipment if the yield stress is exceeded, the granule will be deformed.

The deformation of a granule during an impact in the granulator will be a function of the granule yield stress compared to the kinetic energy absorbed plastically during the collision. This ratio is called the Stokes deformation number St_{def}, (Tardos et al., 1997; Iveson & Litster, 1998).

$$St_{def} = \frac{\rho_g U_c^2}{2Y} \tag{1.17}$$

where:

- ρ_g is the granule density;
- Y is the granule dynamic yield stress;
- U_c is a representative collision velocity.

Usually the yield stress of a powder compact is measured by uniaxial or triaxial compression tests. The problem with those tests is that low strain are used and they are essentially static, a non representative situation of what occurs during mixing granulation.

Iveson has demonstrated the possibility to infer the dynamic yield strength by means of relationships that consider binder and powder properties, such as binder viscosity, surface tension, contact angle, powder diameter, and strain rate.

This relationship is retrieved from a load frame compression of a wet pellet test.

At the end the Stokes deformation number is used in a map to predict the growth behavior of powder materials in high shear wet granulators (HSWG), the latter is shown in Figure 1.9, ((Litster & Ennis, 2004)).

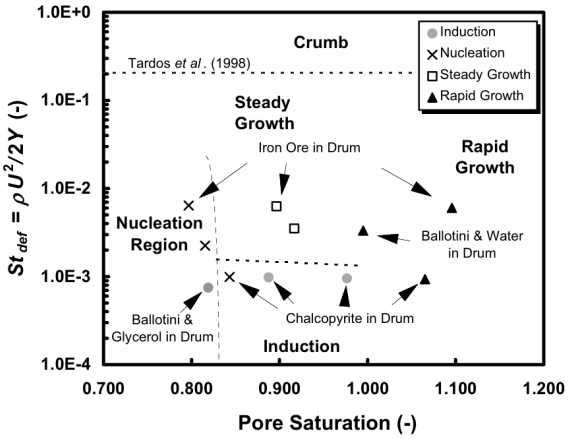

FIGURE 1.9: Growth regime map for granulation of a wide range of materials

1.3 Dynamic indentation of granular materials

From the origin, indentation is a process in which a rigid indenter is driven into a deformable medium under a controlled force or displacement. Indentation testing is a widely adopted method for probing the mechanical behavior of materials under localized loading.

By applying a controlled force to an indenter of known geometry and recording the resulting penetration depth, one can derive critical mechanical properties such as hardness, elastic modulus, and yield strength, (Oliver & Pharr, 1992). The technique requires minimal sample preparation, and can be applied to a wide range of materials, from bulk metals to thin films, polymers, and granular matter.

1.3.1 Fundamentals of Indentation Mechanics

The response of granular matter has been, and is today object of interesting, understanding the intrusion of solid objects is key point to model many aspects of behavior of granular matter, including plastic flow.

The development of indentation mechanics in quasi-static regimes has its theoretical foundation in the work of Prandtl, (Prandtl, 1920), who proposed a slip-line solution for the indentation of a rigid wedge into an ideal plastic material.

The solution has been then proved using DEM simulations almost 100 years later.

The mechanical response of the material beneath the indenter depends on the local stress and strain fields, which evolve as the penetration progresses. Figure 1.10, schematically represents the deformation field during quasi-static indentation with a conical indenter.

At the initial contact, the indenter penetrates the material, generating a highly stressed zone beneath the tip. As the depth increases, the material around the indenter undergoes plastic deformation and is displaced both downward and radially outward. This results in the formation of a plastic zone with a characteristic conical shape (highlighted in pink, angle 2β), surrounded by a broader zone of deformed material (cyan), which includes both plastic and elastic contributions.

Importantly, the image shows how the deformation field extends well beyond the immediate contact area, mobilizing a large volume of material, particularly in granular materials. The cyan region illustrates the progressive mobilization of particles under the applied force F_z , with deformation propagating radially as indentation depth increases.

This study was carried out under quasi-static conditions, where rate dependent effects are negligible. The geometry used allows for simplified analytical treatment, but the main features of the deformation field are known to be qualitatively valid for other indenter geometries as well, including spherical or pyramidal tips, (Kang et al., 2018).

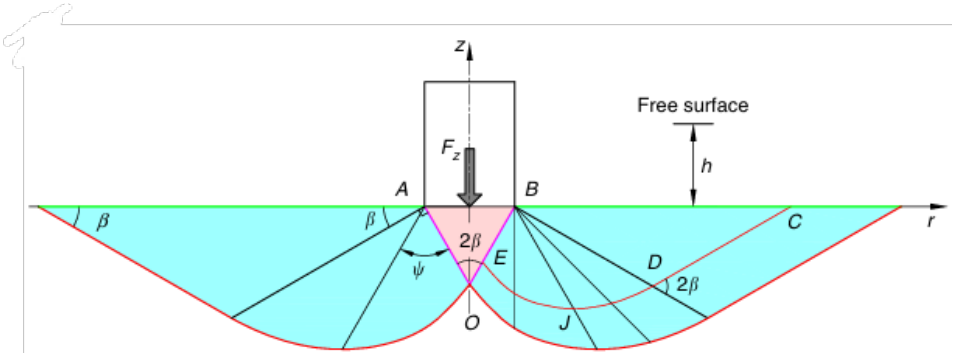

FIGURE 1.10: Deformation field during static indentation

1.3.2 Quasi-static vs dynamic indentation

In metal indentation there are a lot of quasi-static techniques, some widely known like Vickers, Brinell, Knopp, which differ primarily in the geometry and size of the indenter as well as the applied load.

- The Vickers test uses a pyramidal diamond indenter and is suitable for a wide range of materials, including very hard ones.

- The Brinell test uses a relatively large spherical indenter, typically for softer metals, and provides an average hardness over a larger area.

- The Knoop test employs an elongated pyramidal indenter and is mostly used for micro-hardness testing, particularly for thin coatings or brittle materials.

There are formulas to convert the results from one scale to the other.

These quasi-static tests assume negligible inertial and rate dependent effects, making them ideal for determining intrinsic material properties such as hardness and elastic modulus in materials that do not present behaviors dependent on time, (Pasha et al., 2015; Hassanpour & Ghadiri, 2007).

Since granulation of powders is a rate dependent process, classical quasi static indentations techniques do not describe well the properties of powder during this process.

For this reason dynamic indentation seems to represent better the time dependent powders behavior.

In the specific configuration adopted in this work, the Dynamic Ball Indentation method is employed, (Tirapelle et al., 2020). Here, a spherical indenter is released from a known height, impacting the powder bed. This approach enables the simultaneous evaluation of penetration depth, impact velocity, and deceleration profile, which can be related to force and hardness, (Santomaso, 2025).

Dynamic indentation, in contrast to the quasi-static one, involves the application of load over short timescales, also at high strain rates.

An important distinction is made between quasi-static and dynamic indentation. With quasi-static indentation the indenter is driven at a constant rate, the penetration depth is controlled and the loading force is measured. Whereas with the dynamic approach the indenter is released and accelerates under gravity. In this case the penetration depth cannot be controlled: it depends on the indenter kinetic energy and powder flow properties (Tirapelle et al., 2020).

Up to now, the application of the Dynamic Ball Indentation method has been limited to dry powders. In this work, for the first time, this technique will be applied to wet powders, in order to characterize their mechanical response in function of different binder types and quantity. This represents a novel extension of the method, since the presence of liquid bridges and capillary effects introduces additional time- and rate-dependent mechanisms that cannot be captured by classical quasi-static approaches. Previous studies will be used as a benchmark to interpret the obtained results.

Chapter 2

Materials, apparatus and analysis procedure

This chapter describes the experimental setup and the methodology of the Dynamic Ball Indentation (DBI) method. The technique has been applied to different powder types and binder formulations, tested at various liquid contents in order to investigate the influence of binder amount on the mechanical response of wet powders under indentation. Different initial compaction states were also explored to assess their impact on the measured properties.

In addition to the materials and experimental procedures adopted, the computational workflow used for data extraction and analysis is also presented.

2.1 Materials

In this study both powders and binders of pharmaceutical interest were investigated, together with reference systems for comparison. The selected materials are listed below with their main characteristics.

2.1.1 Microcrystalline cellulose (MCC)

A purified, partially depolymerized cellulose that occurs as a white, odorless, tasteless, crystalline powder composed of porous particles. Its structural formula is shown in Figure 2.1, A widely used pharmaceutical excipient, primarily as a binder/diluent in oral tablet and capsule formulations where it is used in both wet-granulation and direct compression processes.

It is also used in tableting due to its lubricant and disintegrant properties.

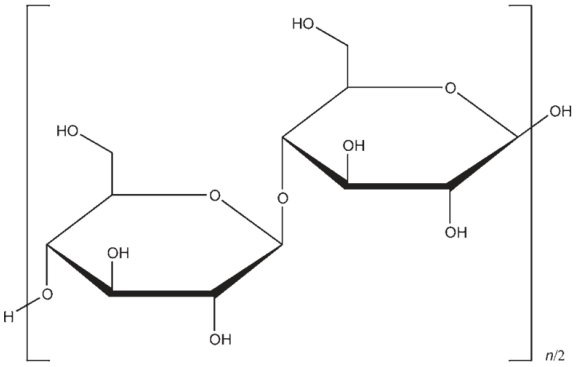

FIGURE 2.1: Structural formula of MCC

Upon wetting it swells, altering porosity and mechanical response during granulation, (Nicklasson & Alderborn, 1999).

Particle size distribution (PSD), based on volume, was measured using a Laser Diffraction Particle Size Analyzer, Mastersizer Hydro 2000SM (methodology described in Chapter 2.2.1). The results are shown in Fig. 2.2.

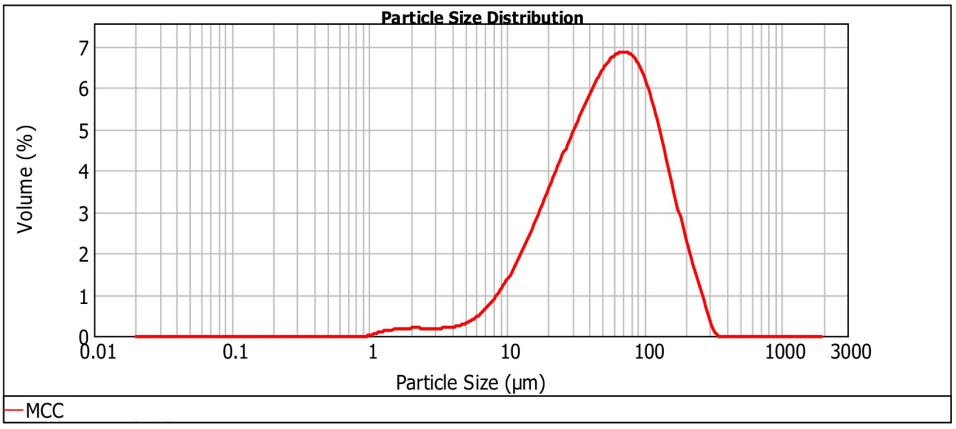

FIGURE 2.2: PSD of MCC powder

The PSD is narrow, covering a size range from $14.923\,\mu m$ to $147.951\,\mu m$, with a median particle size of $d_{50} = 54.842\,\mu m$. It is monomodal, and the particles have a mean specific surface area of $SSA = 0.209\,\mathrm{m}^2/\mathrm{g}$.

Furthermore mages of MCC structure are shown in Figure 2.3, the latter have been taken using an Environmental Scanning Electron Microscope (ESEM), which method is presented later in the methods section 2.2.2. Is possible to notice the fibrous and crystalline structure that characterize MCC, that help the formation of mechanical interlocking between particles.

Furthermore thanks to its surface hydroxyl groups, MCC is able to establish hydrogen bonds between particles, creating strong bonds that leads to high resistance to external forces (Rowe et al., 2006).

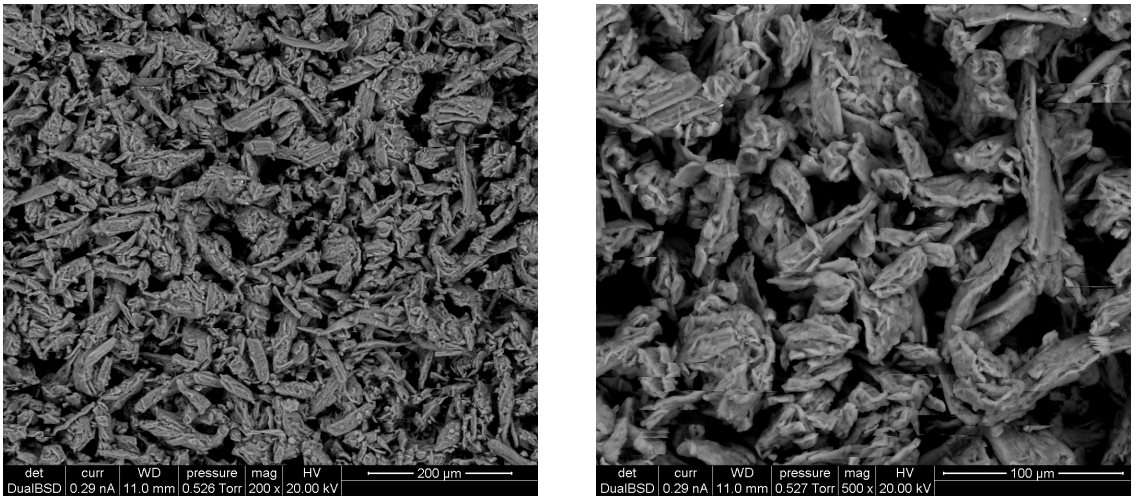

(a) Magnification 200× **(b)** Magnification 500×

FIGURE 2.3: Structural ESEM image of MCC powder

2.1.2 Calcium Phosphate, Dibasic Anhydrous, $CaHPO_4$ A or DI-CAFOS A

A brittle, non-swelling excipient. Generally used as tablet and capsule diluent, or as a source of calcium in nutrition supplement.

Its molecular structure is shown in Fig.2.4

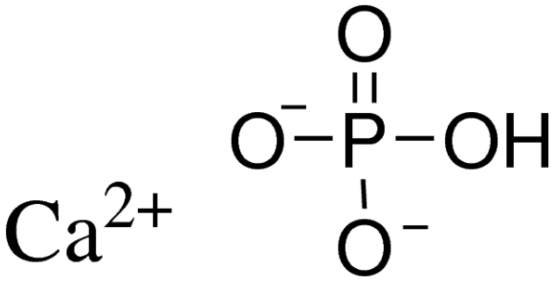

FIGURE 2.4: Structural formula of $CaHPO_4$

The predominant deformation mechanism of anhydrous dibasic calcium phosphate coarse-grade is brittle fracture and this reduces the strain-rate sensitivity of the material.

Two particle-size grades of anhydrous dibasic calcium phosphate are used in the pharmaceutical industry. Milled material is typically used in wet-granulated or roller-compacted formulations. The 'unmilled' or coarse-grade material is typically used in

direct compression formulations. Anhydrous dibasic calcium phosphate is nonhygroscopic and stable at room temperature. It does not hydrate to form the dihydrate and is nearly insoluble in water (Rowe et al., 2006).

In this study, two different particle size grades were used: a fine one, whose PSD is shown in Fig. 2.5, and a coarser one, reported in Fig. 2.6.

In order to properly evaluate the PSD of $CaHPO_4$ A12, the suspension was sonicated prior to the measurement. This step was necessary because the fine particles tend to stick to each other due to van der Waals or electrostatic forces, leading to the formation of agglomerates. Sonication helps to break these agglomerates, providing a more accurate and representative PSD measurement.

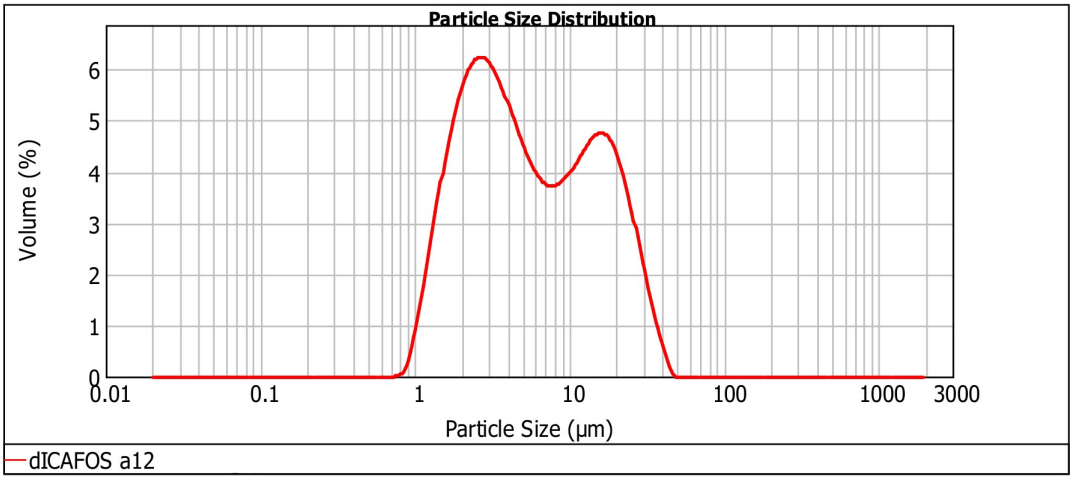

FIGURE 2.5: PSD of DI-CAFOS A12

The finer grade exhibits a bimodal PSD, with the first peak at $2.5\,\mu m$ and a smaller secondary peak at $10.5\,\mu m$. Overall, the distribution is broad, with a median particle size of $d_{50} = 4.98\,\mu m$ and a high specific surface area of $SSA = 1.6\,\mathrm{m}^2/\mathrm{g}$.

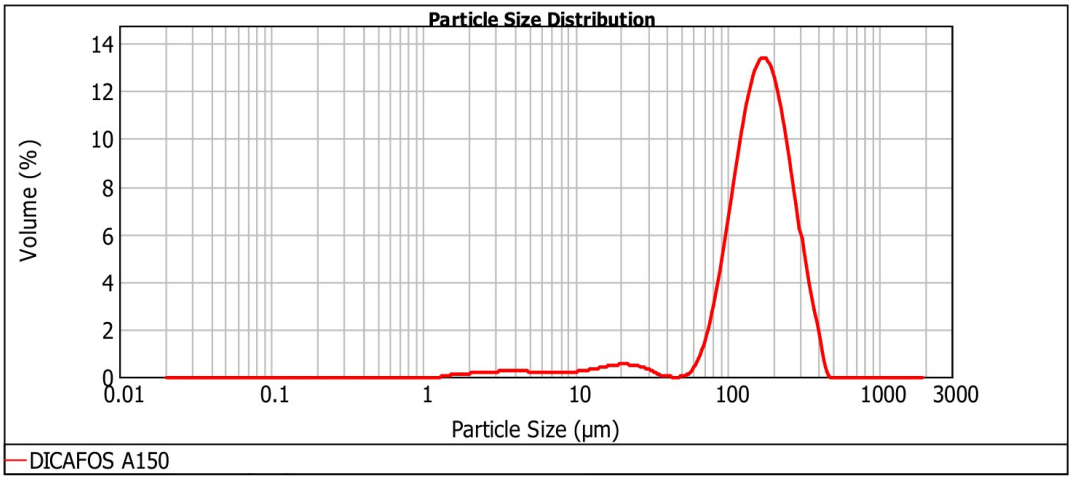

FIGURE 2.6: PSD of DI-CAFOS A150

Conversely, the DI-CAFOS A150 grade shows a monomodal PSD, with a median particle size of $d_{50} = 167.168\,\mu m$ and a specific surface area of $SSA = 0.0857\,\mathrm{m}^2/\mathrm{g}$.

ESEM results for $CaHPO_4$ A12 is reported in Fig.2.7

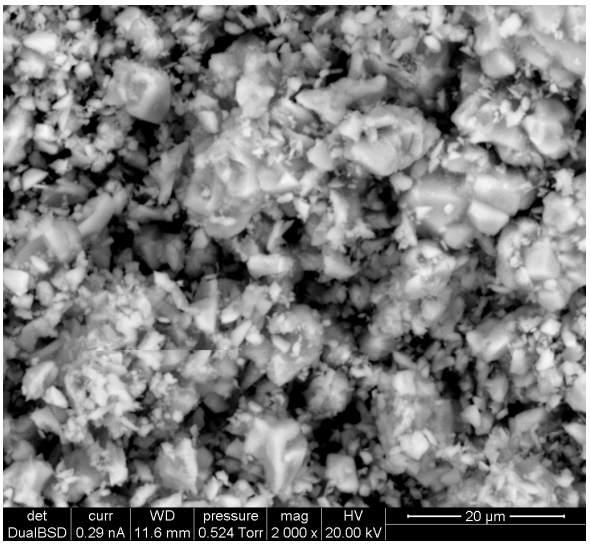

(a) Magnification 2.000×

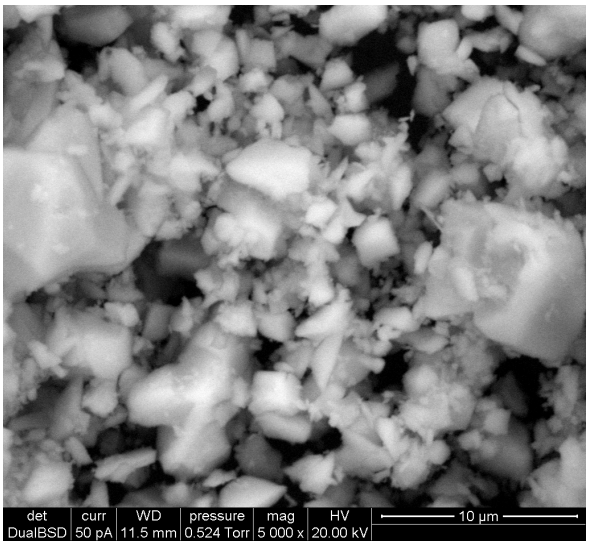

(b) Magnification 5.000×

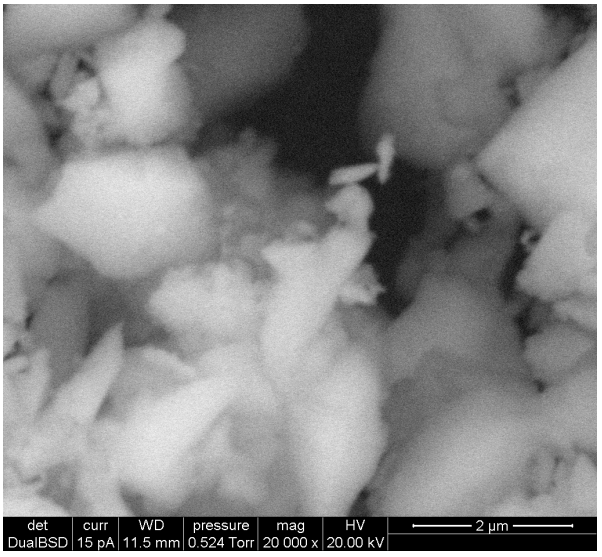

(c) Magnification 10.000×

FIGURE 2.7: Structural ESEM image of $CaHPO_4$ A12 powder

From Figure 2.7(c) is interesting to notice that $CaHPO_4$ have a wide PSD as resulted from PSD measurements, also with very small powder size ($d \sim 1\,\mu m$), in the same figure is possible to notice that very fine powders, like this have strong Van Der Waals and electrostatic contribution in terms of binding forces. In all the ESEM images is possible to see the triclinic crystals form, its crystalline surface limits the formation of hydrogen bonds thus resulting in weak binder–particle interactions in water based media.

The same analysis has been conducted for $CaHPO_4$ A150, shown in Figure 2.8.

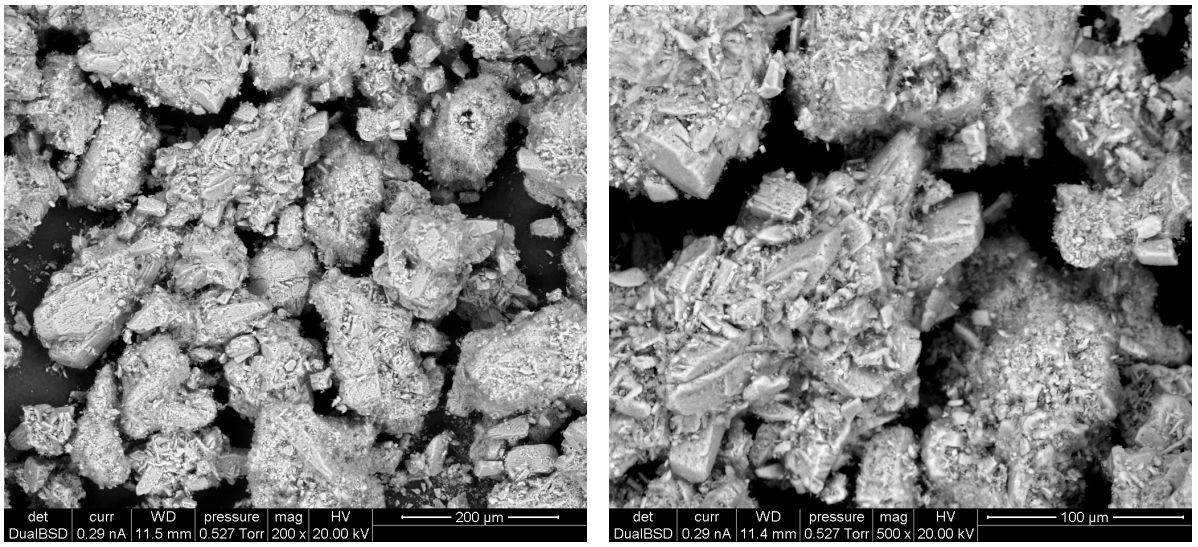

(a) Magnification 2.000× (b) Magnification 5.000×

FIGURE 2.8: Structural ESEM image of $CaHPO_4$ A150 powder

In Figure 2.8 is noticeable the crystalline structure, in bigger agglomerate form with respect to A12 grade.

2.1.3 Silica Sand

An inert, non-pharmaceutical powder, non-porous and non-swelling. This particular type comes from France and is a Fontainebleau sand. Its rigid morphology and absence of chemical or capillary interactions with binders make it a reference material to highlight purely mechanical responses.

The PSD is shown in Fig. 2.9. It is monomodal and narrow, with a median particle size of $d_{50} = 247.121\,\mu m$ and a specific surface area of $SSA = 0.0253\,\mathrm{m}^2/\mathrm{g}$.

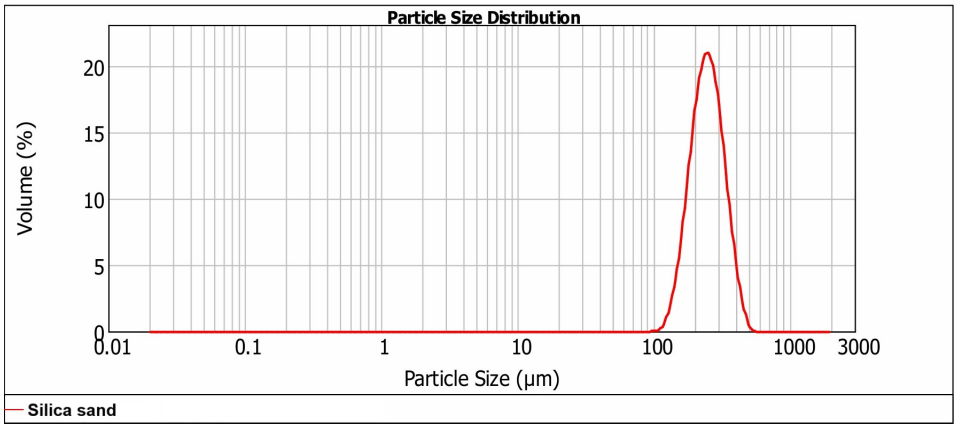

FIGURE 2.9: PSD of silica sand

ESEM images are reported in Figure 2.10.

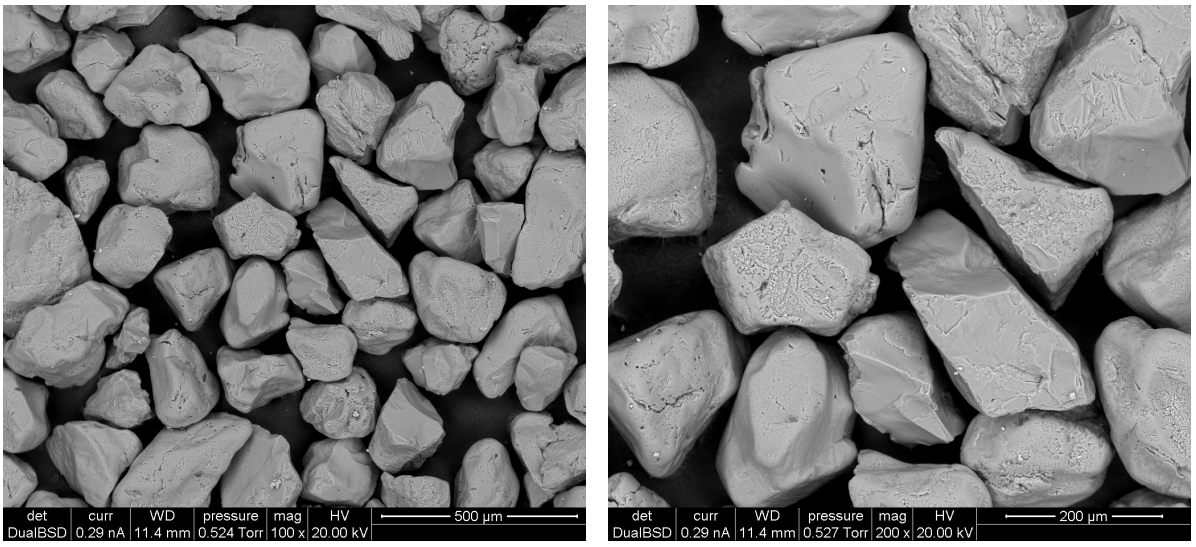

(a) Magnification 100× (b) Magnification 200×

FIGURE 2.10: Structural ESEM image of silica sand

With a special feature of the Environmental Scanning Electron Microscope, has been possible to investigate also the sand' superficial composition, the result highlight that the superficial composition is 98.3$wt\%$ Silicon and 1.7$wt\%$ Aluminum.

Binders

2.1.4 Water

A reference polar binder, Newtonian with constant viscosity $\eta \approx 1\,\mathrm{mPa{\cdot}s}$.

2.1.5 Hydroxypropyl methylcellulose (HPMC)

A cellulose-derived hydrophilic polymer widely used in oral, ophthalmic, nasal, and topical pharmaceutical formulations.

Its primary use is as a binding agent in solution for wet granulation, but it is also employed in dry granulation, film-coating, and as a matrix for extended-release formulations.

Additionally, it serves as a suspending/thickening agent in liquid and topical preparations, and is used in capsules, cosmetics, and food products, (Rowe et al., 2006).

Its structural formula is shown in Figure 2.11.

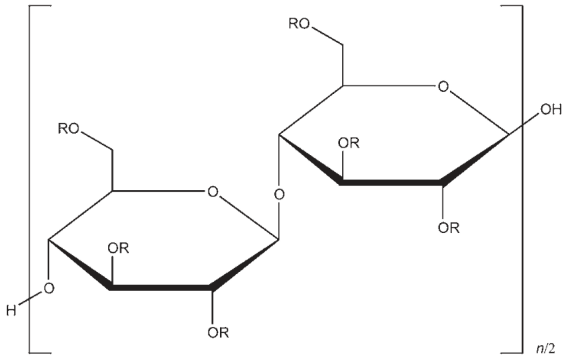

where R is H, CH_3, or $CH_3CH(OH)CH_2$

FIGURE 2.11: Structural formula of HPMC

It is commercially available in different molecular weight grades, which directly affect the viscosity of its aqueous solutions. In this work, a high-molecular-weight grade (nominal viscosity 100000 mPa·s at 2% w/w) was employed. Viscosity is commonly used as a practical proxy for molecular weight, since higher chain lengths lead to stronger polymer entanglement and so higher viscosity. At the investigated concentrations, HPMC solutions exhibit shear-thinning behavior, i.e., their viscosity decreases with increasing shear rate.

2.1.6 Silicone oil

A non-polar binder, that does not have pharmaceutical application, Newtonian with constant viscosity $\eta \approx 339.5$ mPa·s. Is used as a contrast system to investigate the role of binder polarity in wetting and mechanical response.

Summary table A summary of the investigated powders and binders is reported in Tables 2.1 and 2.2.

TABLE 2.1: Powders used in the study

Powder	**Grade**	**Notes**
Microcrystalline Cellulose (MCC)	Grade 101	Common in wet granulation; swells upon wetting
Calcium phosphate ($CaHPO_4$)	Anhydrous A12	Water-absorbing, limited structural change expected
Calcium phosphate ($CaHPO_4$)	Anhydrous A150	Same composition, coarser granulometry of A12
Silica Sand	Technical grade	Inert, non-porous, non-pharma; used for comparison

TABLE 2.2: Binders used in the study

Binder	**Concentration**	**Notes**
Water (H_2O)	Pure	Reference polar binder
HPMC solution	0.75% and 1.0% w/w	High-viscosity aqueous binder used in pharma
Silicone oil	Pure	Non-polar, non-pharma, liquid used for contrast with polar systems

2.2 Apparatus and methods

2.2.1 Laser diffraction particle size analyzer

The Mastersizer Hydro 2000SM (Malvern Instrument, UK) shown in Fig.2.12, is a fully integrated and automated laser diffraction particle size analyzer equipped with a wet dispersion unit which allows the determination of particle size and particle size distribution of pharmaceuticals (powders, granules, emulsions, etc), bulk chemicals and minerals. The instrument assured measurement performance in the dynamic range 200 nm - 2000 µm.

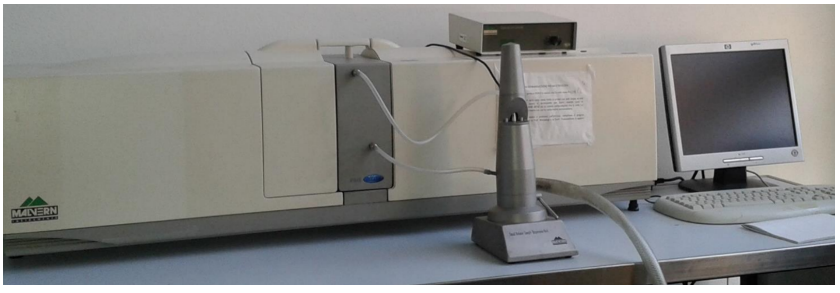

FIGURE 2.12: Mastersizer Hydro 2000SM laser diffraction particle size analyzer

The system operates by measuring the intensity of light scattered by particles suspended in a liquid medium. The angular distribution of the scattered light is then analyzed according to Mie theory to calculate the particle size distribution.

The obtained particle size distribution can be expressed in terms of volume or number, and characteristic diameters such as d_{10}, d_{50}, d_{90}, and $d_{3,2}$ are automatically calculated by the instrument software, providing a quantitative description of the sample's granulometric profile.

2.2.2 Environmental Scanning Electron Microscopy (ESEM)

The granules superficial structure was analyzed by ESEM (Environmental Scanning Electron Microscopy) using a scanning electron microscope (FEI Quanta 200, Philips, Austin, TX, USA) (Figure 2.13) operated at 20 kV. The instrument was equipped with back-scattered electron (BSE) detectors and an energy-dispersive X-ray spectroscopy (EDS) detector.

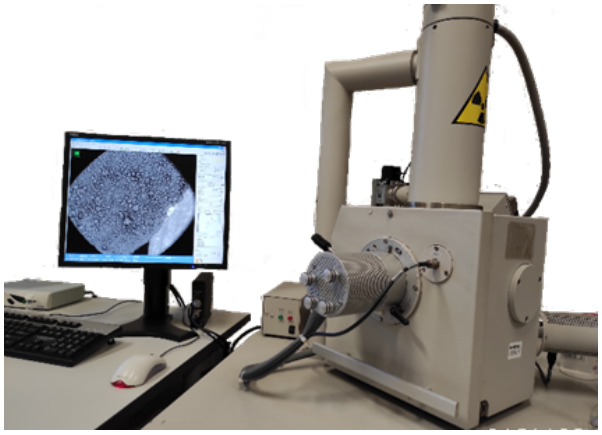

FIGURE 2.13: Environmental Scanning Electron Microscope (FEI Quanta 200 model, Philips, Austin, TX, USA).

Prior to analysis, a vacuum was applied to remove reactive gases such as oxygen. Then, a controlled flow of gas was introduced into the chamber to enable stable imaging under environmental conditions. Unlike conventional SEM, no gold sputter-coating was required, as the environmental mode prevents surface charging and allows direct observation of the sample.

The entire process was carried out at low temperatures to prevent sample damage.

2.2.3 Rotational rheometer

Since viscosity is fundamental in this study, it has been studied deeply.

Water and silicone oil are Newtonian fluids, with constant viscosity of $\eta_{H_2O} = 1$ mPa·s and $\eta_{\text{silicone oil}} = 339.5$ mPa·s, respectively. HPMC solutions, instead, are non-Newtonian liquids that exhibit shear-thinning behavior.

At low HPMC concentrations the non-Newtonian effects are negligible, as the polymer content is insufficient to form entangled networks. At higher concentrations, however, polymer entanglements cause pronounced shear-thinning. At low shear rates, entangled polymer chains increase resistance to flow, whereas at high shear rates these interactions are progressively disrupted, reducing viscosity. Importantly, no hysteresis effects were observed when shear was reduced.

Viscosity curves for HPMC solutions are reported in Fig.2.14, the internal plot represent the viscosity of the solution depending on the concentration of polymer in water, at maximum studied shear rate, useful to understand which is the general trend of the viscosity in function of HPMC concentration.

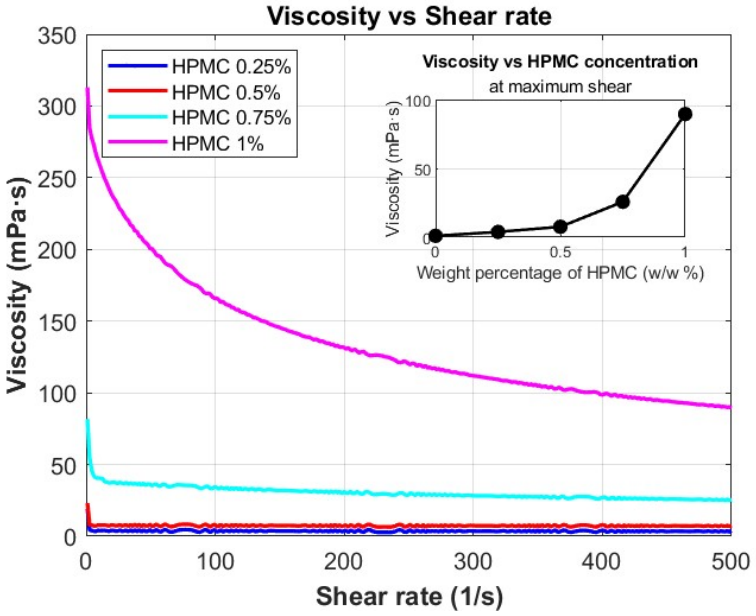

FIGURE 2.14: Viscosity curves for HPMC solutions

Since the need was to investigate the effect of binder viscosity on powder behavior, HPMC concentrations of 0.75% and 1.0% were selected, as they differ significantly from the viscosity of water.

The fluctuations in Fig. 2.14 are attributed to the measurement system, as they appeared consistently in all trials with the same amplitude and periodicity.

Viscosity measurements were carried out using an Anton Paar MCR 92 rheometer (Fig. 2.15). A concentric cylinder geometry was selected to obtain precise viscosity measurements varying shear rates.

FIGURE 2.15: Anton Paar MCR 92 rheometer

For each measurement, the binder sample was placed in a 17 *cc* stainless steel cup (right in Fig.2.16) and loaded into the rheometer. A linear shear ramp from 1 s^{-1} to 500 s^{-1} was applied in order to evaluate viscosity across a wide range of shear rates. Tests were performed at $T = 25°C$, consistent with the environmental conditions ($19°C$–$23°C$) of the indentation experiments.

FIGURE 2.16: From left to right: the internal cylinder, and the external one

2.2.4 Sessile drop method for surface tension

Surface tension of the used binders are summarized in Table 2.3. For the selected HPMC solutions the surface tension has been calculated using the sessile drop method, which theory has been presented on Chapter 1.2.2.1. Images of drops deposited on a Teflon surface (to minimize liquid–solid affinity) were analyzed using a custom Matlab® script.

As shown in Table 2.3, the sessile drop method displayed limited accuracy: small uncertainties in drop shape detection led to large variability in the estimated surface

TABLE 2.3: Surface tension values of the binders used in this study.

Binder	**Surface tension** [mN/m]	**Source / Method**
Water (H_2O)	72.8	Literature value at 20°C, (Doble, 1984)
HPMC solution (0.75% w/w)	48.5 ± 7.3	Sessile drop method
HPMC solution (1.0% w/w)	36.5 ± 11.2	Sessile drop method
Silicone oil	21.1	Manufacturer datasheet

tension. To minimize this effect, 10 independent measurements per binder were performed, and mean values were reported.

2.2.5 Torque rheometry

Torque rheometry provides a macroscopic measure of the resistance exerted by a powder bed against the rotation of mixing elements at controlled speed. The measured torque reflects the combined effects of interparticle friction, capillary cohesion, and viscous dissipation, thus offering an indirect but quantitative estimate of the bulk mechanical properties of the material. By progressively increasing the binder content, torque measurements allow for the identification of the transitions between the classical saturation regimes, pendular, funicular, capillary, and droplet.

In this work, a torque rheometer (MTR 3, Caleva Process Instrument, Dorset, UK) was used to characterize the pharmaceutical powder–binder combinations subjects of this study.

The MTR is specifically designed to monitor changes in cohesiveness and stickiness of powders upon liquid addition. It consists of a mixing chamber equipped with two contra-rotating blades. The chamber is free to rotate around the drive axis, while the torque is transmitted through an arm connected to a calibrated load cell (Fig.2.17). This configuration enables the direct measurement of torque variations occurring during the wetting of powders, thereby allowing the study of binder–powder interactions, (Santomaso et al., 2017).

Experiments were performed following the multiple addition method. Specifically, 12.5 g of MCC or 45 g of $CaHPO_4$ were introduced into the empty chamber and mixed at a shaft speed of 150 rpm. The binder was progressively added in discrete steps: 1 mL per addition. After each addition, the wet mass was mixed for 10 s when water was used as binder, or for 20 s in the case of HPMC solutions, to account for their higher viscosity and slower homogenization. Subsequently, the torque value was recorded for

15 s. The total liquid volume added depended on the powder–binder system and was adjusted to reach the overwetting condition.

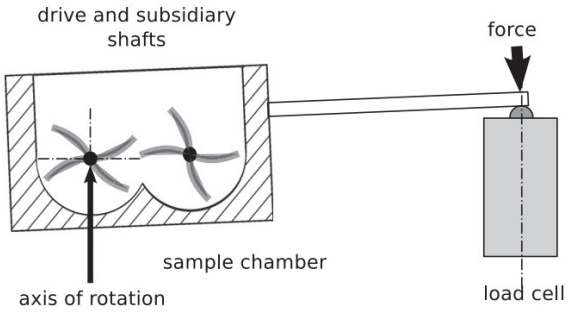

FIGURE 2.17: Schematic of the torque measurement system

A general example of a MTR study is reported in the top image of Figure 2.18, while on the bottom the respective on line torque measurement on an high shear granulator, the comparison between this two methods has been done from Santomaso and co-workers in order to retrieve the optimal granulation condition from torque measurements, (Chitu et al., 2011a).

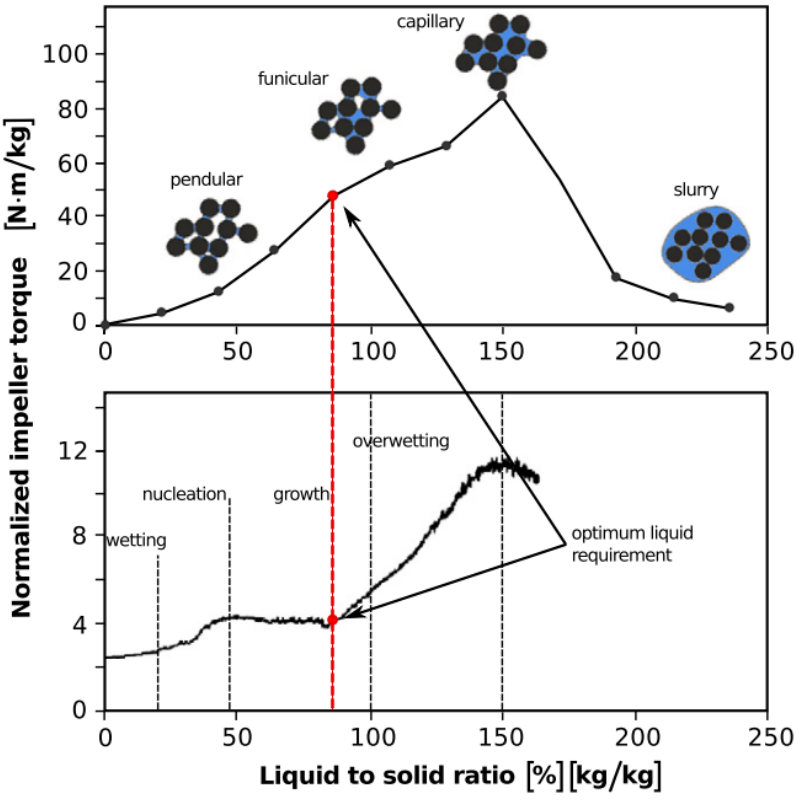

FIGURE 2.18: General torque profiles resulting from the addition of a binder to a powder: a) in MTR; b) on-line torque measurement in a high shear granulator, (Santomaso et al., 2017)

As shown in the MTR profile (Fig. 2.18(a)), the curve typically exhibits a bell-shaped trend: the torque increases to a maximum and then decreases rapidly. The different regions of this curve correspond to the characteristic saturation regimes of powders, and the optimal granulation point is usually located within the funicular state. This point is associated with an inflection in the torque curve, which is not always easy to identify.

For some systems, such as MCC–water (discussed later), this transition zone is evident and easily recognizable. In such cases, the profile is said to exhibit a "shoulder". However, this is not the general case. For most systems, such as $CaHPO_4$ in this study, the second derivative of the torque curve must be calculated to locate the inflection point (the first point where the second derivative is zero) (Santomaso et al., 2017).

2.3 Sample preparation and indentation apparatus

2.3.1 Sample preparation

The preparation of the sample and the indentation procedure are the most critical aspects of the ball indentation technique when applied to powders, as they can introduce significant errors in the results.

In their work on static ball indentation of dry powders, Zafar and co-workers proposed a standard operating procedure and defined an operational window to minimize variability of results. They investigated three different filling methods and demonstrated that the sieved filling technique provided the most uniform packing, with minimal void formation.

Moreover, they established practical limits for the indenter size: the minimum diameter should be larger than 16 times the mean particle size, while the maximum should be less than 0.65 times the bed diameter.

Finally, since ball indentation allows multiple measurements on the same sample, each indentation should be placed at a minimum distance of approximately 1.5 times the indenter diameter from both previous indents and the container walls, in order to minimize boundary effects, (Zafar et al., 2017). This recommendation arises from the fact that, as illustrated in Fig.1.10, the stress field generated by indentation extends well beyond the immediate contact zone.

Although the present work focuses on dynamic ball indentation, these guidelines have been taken into account to ensure the reliability and reproducibility of the results.

Operatively the workflow for the sample preparation began with weighting the powder and binder to achieve the desired relative amount, followed by mixing in a high-shear wet granulator (HSWG) to prevent binder heterogeneity.

First, the dry powder was loaded in the granulator and mixing was initiated at low speed. The binder was then added by means of a pipe directed on the center of the stirring system, point in which there is the higher turbulence, to promote uniform wetting.

The low speed phase minimized powder adhesion to the surfaces of the HSWG. After binder addition, the impeller speed was increased to $3000rpm$ for one minute to homogenize the mixture.

The wet powder was subsequently transferred into a Teflon cylinder, as recommended by Zafar et al. (Zafar et al., 2017), by pouring it through a sieve of appropriate mesh size.

The Teflon cylinder reduces boundary effects during indentation while the sieving promote pluviation, a deposition method in which particles settle by gravity and self-organize into a loosely packed bed. This method minimizes mechanical compaction and creates a reproducible initial porosity, which is essential for meaningful comparison. At high binder concentration, because of the higher powder cohesion, sieving under gravity was difficult; in these cases, the powder was manually forced through the mesh to complete the pluviation process.

Once the cylinder was filled, the procedure described by Santomaso in his work, (Santomaso, 2025) was followed. An excess of powder was first added, and the surface was leveled using a ruler. A Teflon piston, coaxial with the cylinder, was then positioned and loaded with the appropriate weight to achieve the target stress levels of 1, 5, and 9 kPa.

The piston was kept in place for approximately one minute to allow stress relaxation and minimize elastic recovery. After its removal, additional powder was added to restore the bed height to the cylinder rim, compensating for the volume reduction induced by compaction. This procedure was repeated until no further reduction in bed height was observed, indicating that the free surface remained flush with the upper edge of the cylinder.

2.3.2 Optics and image detection apparatus

In this section is presented the apparatus used for the indentation data acquisition and binders' surface tension evaluation.

The dynamic ball indentation method builds upon principles shared with conventional indentation techniques.

However, in contrast to quasi static methods, capturing the highly dynamic indentation process requires different instrumentation, capable of acquiring data with high temporal resolution.

For this reason, a high-speed camera capable of recording (at maximum frame rate) 204100 frames per second was used, for having a good balance between time resolution and image resolution the frame rate was set at 10500 fps. The frame rate need to be good enough to capture the rearrangement phenomena of the indented powder.

Achieving an accurate visualization of the indenter is essential for precise image tracking. Standard optical systems and lights suffer from perspective distortion, where objects put closer to the lens appear larger than if put farther away. This is particularly critical for DBI method, because if is not corrected, the conversion between pixel and length is not unique, and can cause problems when comparing different trials.

To overcome this limitation, the optical setup is made of a telecentric lens in combination with a telecentric backlight. Telecentric optics eliminate perspective errors by ensuring that the magnification remains constant regardless of the object's distance from the lens, (Opto Engineering, 2025). This setup guarantees accurate and undistorted measurements of the indenter position, diameter, and trajectory over time. The backlight further enhances edge detection by providing high-contrast of the sphere during motion.

All is kept at a fixed position by a robust structure that ensure the alignment between telecentric light and camera, this is crucial in this type of setup be cause a minimal misaligning lead to high loss on resolution.

The setup used for DBI method is shown in Fig. 2.19.

Explicitly the optic and the light comes from the company Opto Engineering, the models are respectively: TC3MHR036-C and LTCLHP036-G, while the camera is an i-speed 220 (IXCAMERAS LTD).

Indentation was performed using a chrome steel spheres with a diameter of $D_b = 8mm$ that was held on the top of the powder bed using an electromagnet, that has the function of a precise releasing, once the recording was started.

Once the indentation has been recorded by means of a dedicated software, the images are processed using Matlab®.

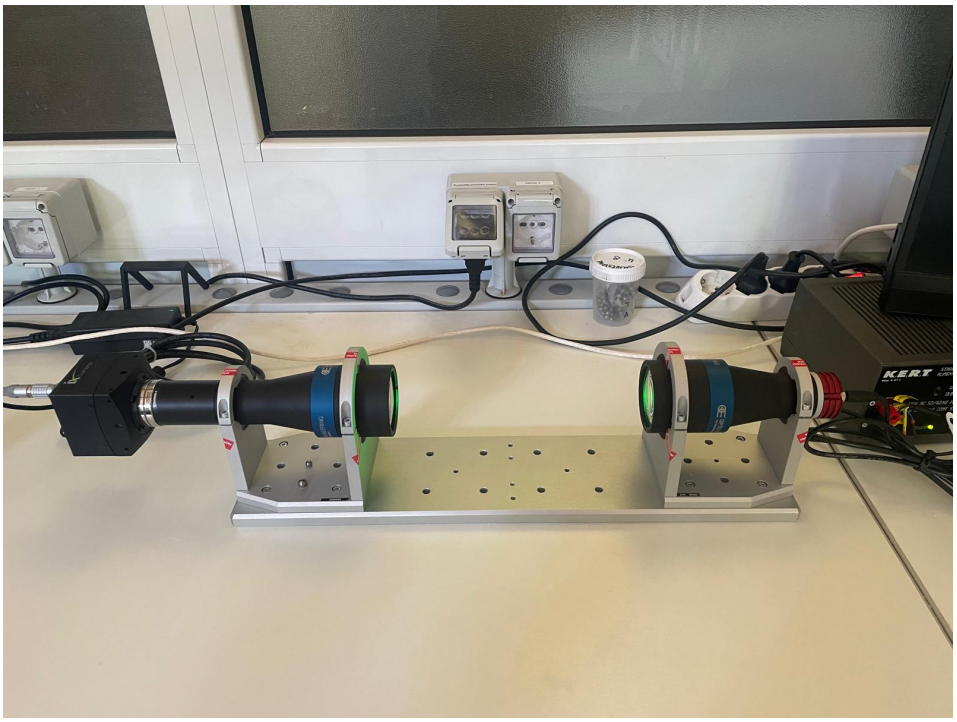

FIGURE 2.19: At the left the high-speed camera with the telecentric optic, at the right the backlight

2.4 Data acquisition and analysis procedure

After recording the indentation process, information can be extrapolated from the sequence of frames.

2.4.1 Image processing and position tracking

Ad hoc processing Matlab® code has been created in order to code the trajectory of the indenter, the script to run needs the folder path that contains the frames and the experiment information that are going to be stored afterword in a results matrix, those information are: powder and binder type used, consolidation pressure and binder percentage on the sample.

The first part of the analysis consist in an auto detection of the powder bed surface, since it can varies of some pixel from a trial to another, this can be caused for example by a different particle size. Taking the first frame of the sequence, shown for example in Fig.2.21(a), it analyses the figure starting from a first guess that is known to be a white line between the indenter and the sphere, and moving to the bottom of the figure it search for the first row that has 80% black pixels, this row will be saved for all the frame analysis as the bed surface, the 80% reference is set because is a compromise between a full black line and the first line which has at least one black pixel, that can be both

poorly representative of the powder bed, as shown in Fig.2.20. This criterion is necessary because the surface is not always perfectly smooth: the presence of a wet powder causes the material to form aggregates and makes the leveling operation challenging, leading to small surface irregularities and local imperfections in the bed.

FIGURE 2.20: Poorly representative bed line tracking

Since a lot of frames need to be analyzed once the powder line has been detected, the region considered in the next analysis is reduced from an upper boundary that has been chosen considering the diameter of the indenter, this is shown in magenta in Fig.2.21(a), the tracking of the sphere will start from the first frame in whitch the sphere has completely crossed the upper boundary in order to speed the frame analysis by the removal of a first part of recorded images.

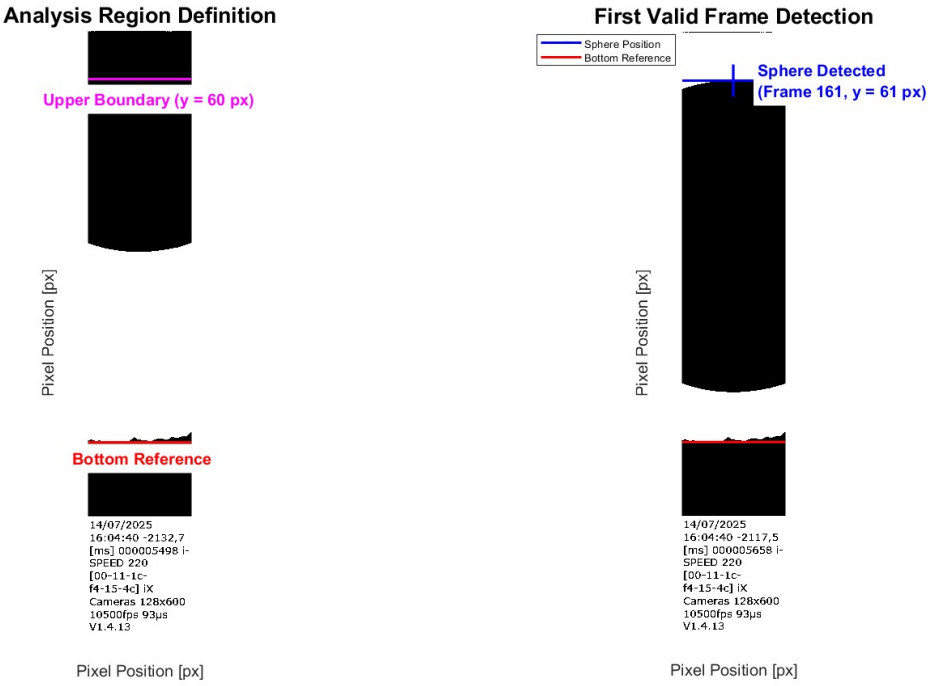

(a) Definition of the analysis region **(b)** First position saved

FIGURE 2.21: Frame analysis

Once the relative position of the sphere with respect to the bed line has been identified for each frame, the pixel coordinates can be converted into metric units. This conversion is performed using a calibration factor expressed in mm/pixel. The factor depends on the lens zoom but not on the distance between the indenter and the lens, since the use of telecentric optics eliminates distance-related optical distortions. Therefore, once a fixed region of interest (ROI) is defined for all trials, the mm/pixel ratio can be determined using image analysis software.

For this purpose, the software Fiji was employed. The conversion factor was obtained by selecting the sphere diameter as the reference length. Since the diameter is chosen manually, a small measurement error is introduced. To reduce this effect, multiple frames and independent experiments were analyzed, allowing a more accurate estimation of the conversion factor. The procedure is illustrated in Fig.2.22.

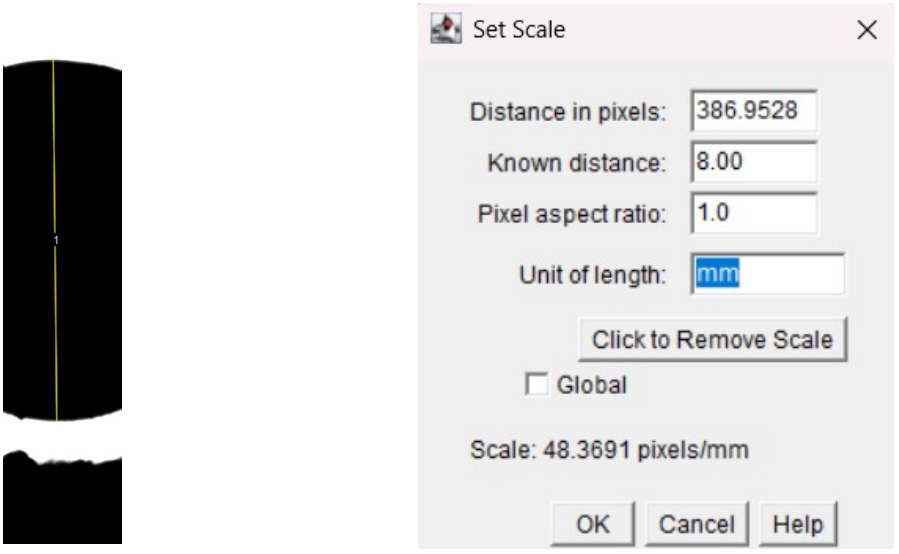

(a) Diameter selection **(b)** Scale factor

FIGURE 2.22: Scale factor definition

Once the indenter trajectory has been extracted, a critical point is the filtering of the position signal. The aim is to smooth the data while preserving key physical information, particularly during the impact phase, where sudden changes in velocity and acceleration occur. These regions are the most informative, as they reflect the material's response to the loading. However, standard filtering approaches often introduce distortions. For example, some low-pass filters can induce a phase shift, effectively delaying the signal and misaligning the measured impact point. This is unacceptable in dynamic indentation, where time alignment is crucial.

To address these limitations, a custom filtering procedure was implemented. The raw displacement data was first subjected to a moving average filter (with a small operating window), applied in both forward and reverse directions to prevent phase shift and preserve the temporal alignment of the signal. This provides a preliminary smoothing by reducing high-frequency noise. Subsequently, a zero-phase digital filter (filtfilt command in Matlab) was applied. This method performs a forward and reverse filtering operation, thereby eliminating phase distortion while ensuring consistent smoothing.

Once the signal has been filtered first and second time derivatives of the filtered displacement were computed numerically, yielding the velocity and acceleration profiles, respectively. These profiles are critical for interpreting the dynamics of the indentation and are later used to estimate the forces involved and derive mechanical properties. An example of the filtered data and its derivatives is shown in Fig.2.23.

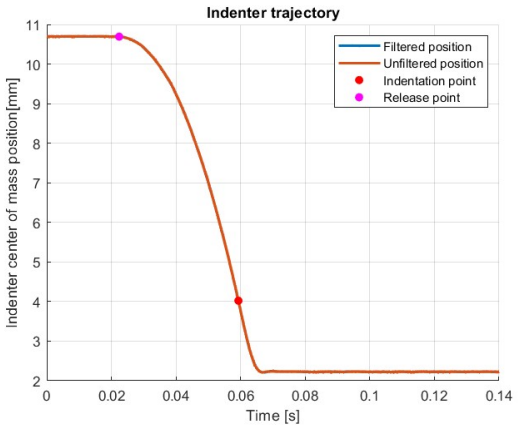

(a) Indenter trajectory

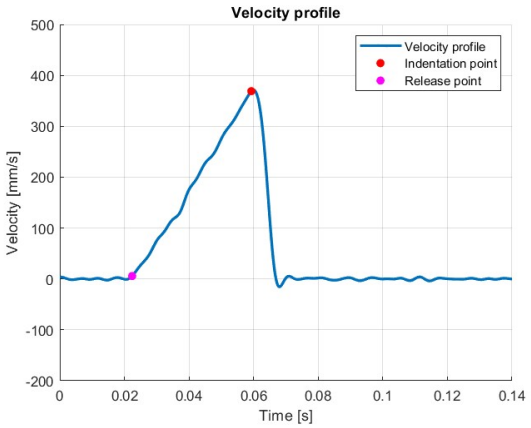

(b) Velocity profile

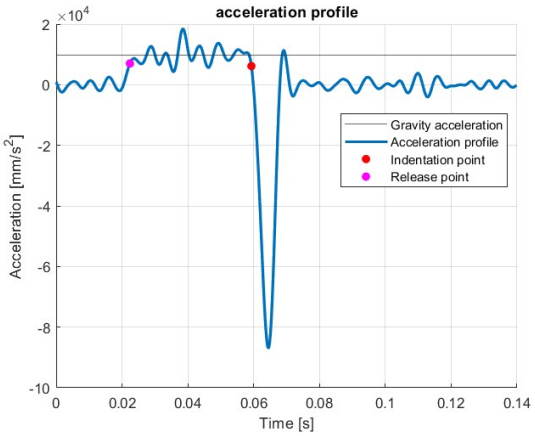

(c) Acceleration profile

FIGURE 2.23: Example of information retrieved from frame analysis

2.4.2 Force and hardness calculations

Once the acceleration profile has been calculated, by means of the second Newton's law the force profile is calculated as,

$$F_{net} = [a(t) - g]m \tag{2.1}$$

Where $a(t)$ is the instantaneous acceleration, g is the gravitational acceleration and m is the indenter weight. The net force is used in order to remove the mass force that always act, also when the indenter is at rest, obtaining a force profile that is purely given by the response of the powder to the penetration. Force profile is useful in order to assess how the resistance of the powder behave and to asses elastic rebound behaviors, (Santomaso, 2025).

Once the net force is determined, the hardness (H) can be evaluated. In conventional quasi-static ball indentation, hardness is defined as the ratio between the maximum applied load F_{max} and the projected contact area at the maximum penetration depth. In this case, the hardness reflects the material resistance under a static maximum load condition.

Similarly, in dynamic indentation, the maximum force can be identified from the force–displacement curve, and the dynamic hardness is calculated as:

$$H = \frac{F_{max}}{A_{cap}} \tag{2.2}$$

where A_{cap} is the surface area of the spherical cap at the penetration depth $h_{F_{max}}$, given by:

$$A_{cap} = \pi D_b h_{F_{max}} \tag{2.3}$$

with D_b the ball diameter and $h_{F_{max}}$ the indentation depth corresponding to F_{max}.

Beyond the evaluation at peak force, it is also possible to calculate a hardness profile over time, expressed as:

$$H(t) = \frac{F_{net}(t)}{A_{cap}(t)} \tag{2.4}$$

This formulation allows hardness to be analyzed at different stages of the impact. In particular, one interesting condition is hardness evaluated at the instant of maximum velocity, which occurs shortly after impact. At this stage, the penetration depth is still small and the confinement of the indenter is minimal, potentially providing complementary information on the initial powder response.

Chapter 3

Dynamic strength of partially saturated powders

3.1 Moisture content and saturation regimes

Before applying the dynamic ball indentation (DBI) method to investigate the dynamic response of powders to deformation, the different saturation regimes were first characterized as a function of binder content using torque rheometry (see Chapter 2.2.5 for a detailed description). This technique provides a macroscopic measure of the resistance opposed by the powder to blade rotation, capturing the combined effects of interparticle friction, capillary forces, and viscous dissipation. By gradually increasing the binder content, the torque curves allowed the identification of the classical regimes (pendular, funicular, capillary, and droplet), offering a quantitative framework for subsequent DBI analysis.

Experiments were carried out with a torque rheometer (MTR 3, Caleva Process Instrument, UK), specifically designed for monitoring powder–binder interactions. Two representative pharmaceutical excipients were studied: microcrystalline cellulose (MCC) and anhydrous calcium hydrogen phosphate ($CaHPO_4$), in grades A12 and A150. As binders, both water and hydroxypropyl methylcellulose (HPMC) solutions at different viscosities were employed. Measurements were performed via the multiple-addition protocol, and the torque values were averaged over three independent repetitions for each powder–binder system.

Torque values are going to be later compared with Hardness by DBI in Chapter 3.4.

3.1.1 MCC torque measurements

In figure 3.1, are presented the torque profiles for MCC powder with water and HPMC solutions as binders.

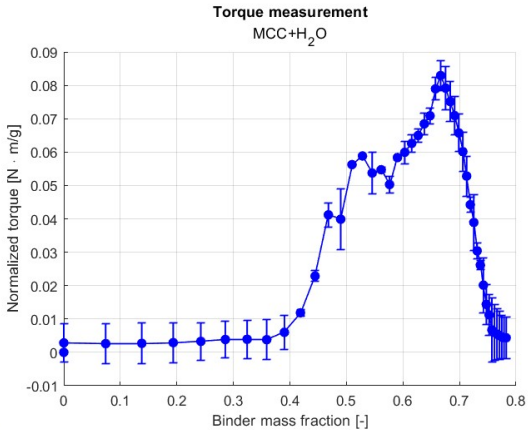

(a) MCC - H_2O

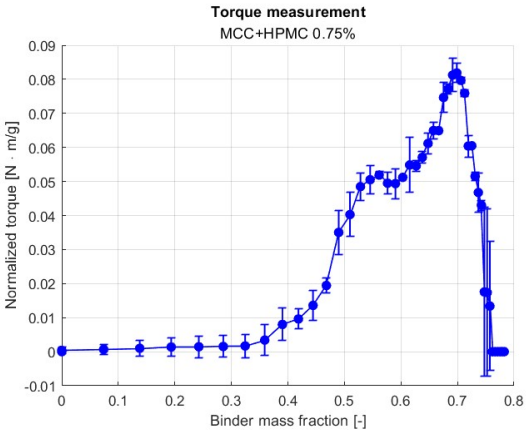

(b) MCC - HPMC 0.75%

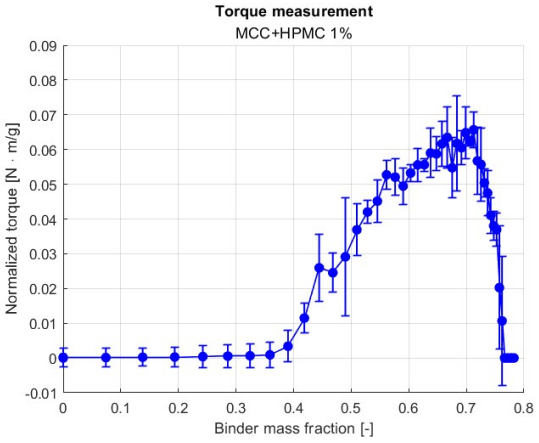

(c) MCC - HPMC 1%

FIGURE 3.1: Torque measurement for MCC powder

The profiles of MCC with water and HPMC 0.75% (Fig. 3.1(a) and 3.1(b) respectively) have a clear shoulder region (for $y_b = [0.5, 0.6]$), which is the transition zone between pendular and funicular regime, this region help to retrieve the optimal binder quantity for high shear granulation.

The optimal liquid fraction required for granulation, correspond to the funicular state, in the MCC cases its value is 0.6 for the mixture with water and HPMC 0.75%, while it decreases to 0.45 for the mixture with HPMC 1% (Figure 3.1(c)).

The formation of the shoulder is the reflection of the property of the MCC powder of adsorbing, retaining and release water during impacts.

The torque growth in HPMC 1% case is less sharp and more homogeneous with the addition of binder, this behavior may be attributed to the reduced absorption rate of the binder and the slower homogenization of the powder–binder mass both caused by the higher viscosity, which in turn leads to a less rapid increase in resistance.

Furthermore the HPMC 1% trial shows a reduced normalized torque, suggesting a decrease in cohesion at higher binder viscosity. This observation contrasts with previous findings in literature (Chitu et al., 2011b), which reported enhanced cohesion with increasing binder viscosity, this can be probably attributed to a lubricant feature of the HPMC solution, this phenomena is present for some types of HPMC, usually the high molar weight one.

3.1.2 $CaHPO_4$ A12 torque measurements

Usually, the identification of the optimal liquid fraction is not trivial, because the inflection point is not marked by a shoulder region. This is evident for $CaHPO_4$ A12, as shown in Fig. 3.2, where the torque profile does not exhibit a shoulder. Instead, the curve reaches a maximum and then sharply decreases.

In this cases the second derivative of the normalized torque help to identify the optimal binder fraction, as the first point where the second derivative becomes zero.

For all the $CaHPO_4$ A12 cases the optimal liquid fraction is around 0.13.

Differently to the MCC profiles the torque peak increases with the increasing viscosity of the binder, this seems reasonable, meaning that viscosity contribute in a direct way to the strength of the wet powder.

The absence of a shoulder in the torque profiles of $CaHPO_4$ indicates a markedly different binder–powder interaction compared to MCC. In this case, the binder is not absorbed within the solid matrix but remains mainly distributed around the particles, forming a superficial coating. This behavior is also reflected in the lower binder mass fractions required to reach the capillary state compared to MCC, highlighting both the lack of significant adsorption and the reduced porosity available for liquid penetration.

This phenomenon was consistently observed not only with pure water but also with HPMC aqueous solutions, suggesting that the key mechanism is governed by the intrinsic interaction of $CaHPO_4$ with aqueous media, rather than by the specific physicochemical properties of the binder. Furthermore, it is interesting to notice that the torque values measured for $CaHPO_4$ are significantly lower compared to MCC. This difference can be explained by the distinct nature of the interparticle interactions promoted by the binder in the two systems.

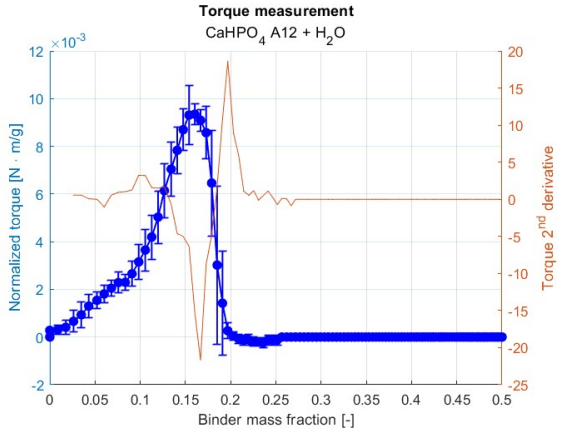

(a) $CaHPO_4$ A12 - H_2O

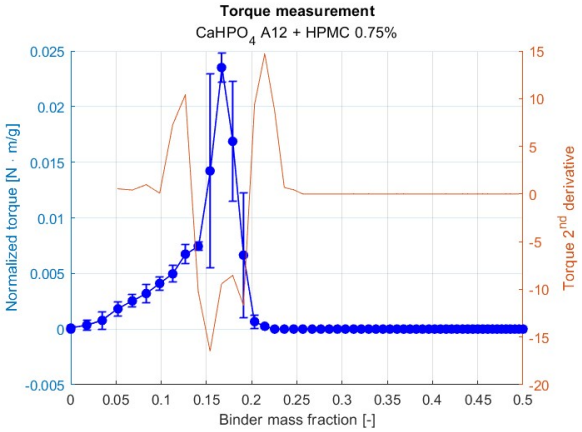

(b) $CaHPO_4$ A12 - HPMC 0.75%

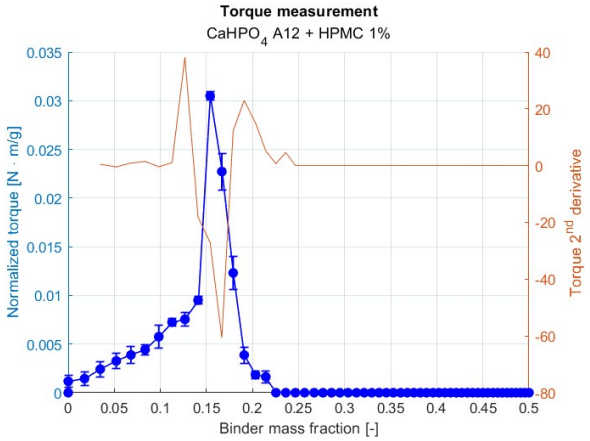

(c) $CaHPO_4$ A12 - HPMC 1%

FIGURE 3.2: Torque measurement for $CaHPO_4$ A12 powder

MCC is a cellulose-derived material with a polymeric and hydroxyl-rich surface. Upon binder addition, especially with water or aqueous solutions, MCC particles are able to establish multiple hydrogen bonds and mechanical interlocking between powder molecules. These connections increase the cohesiveness of the powder bed and translate into higher resistance to blade rotation, (i.e., higher torque values).

On the contrary, $CaHPO_4$ is a crystalline, inorganic material with limited capacity to establish hydrogen bonding or mechanical interlocking. The interactions are mainly governed by capillary bridges and, to a minor extent, by weak van der Waals forces. As a result, even at comparable binder content, the resistance of $CaHPO_4$ beds is much lower, leading to torque profiles with smaller amplitudes.

This comparison highlights how torque rheometry does not only depend on the amount of liquid present, but also strongly reflects the intrinsic physicochemical nature of the solid phase, which dictates the type and strength of the interparticle links

formed during wetting.

3.1.3 $CaHPO_4$ A150 torque measurements

As seen for $CaHPO_4$ A12, also for $CaHPO_4$ A150 the optimal binder quantity is not easily retrieved, and once again the second derivative of the torque curve was evaluated to identify it.

Especially for the H_2O mixture it is difficult to precisely determine the optimal liquid mass fraction, which fall in the range of 0.20–0.25. In the case of HPMC binders, the optimal fraction is slightly higher, around 0.25.

Similarly to $CaHPO_4$ A12, the torque profiles show an increase in granule strength with increasing binder viscosity, confirming that viscous contributions play a direct role in the mechanical response of wet granules to stresses.

Since the nature of this powder is the same as that of $CaHPO_4$ A12, it is reasonable to assume that the absence of a shoulder and the low torque values share the same underlying cause — namely, the very limited binder absorption capability and the reduced possibility of forming hydrogen bonds or mechanical interlocking between particles.

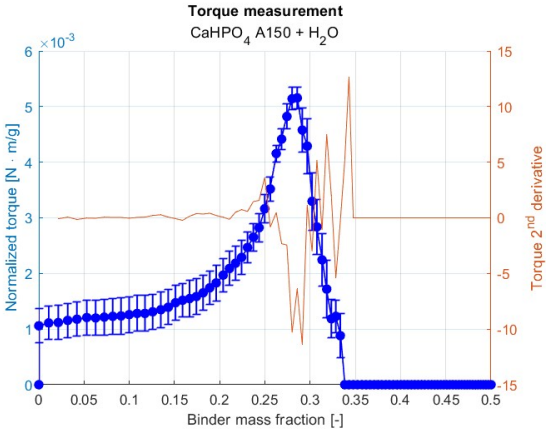

(a) $CaHPO_4$ A150 - H_2O

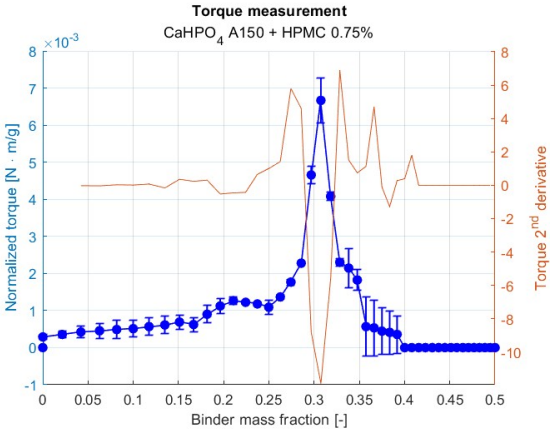

(b) $CaHPO_4$ A150 - HPMC 0.75%

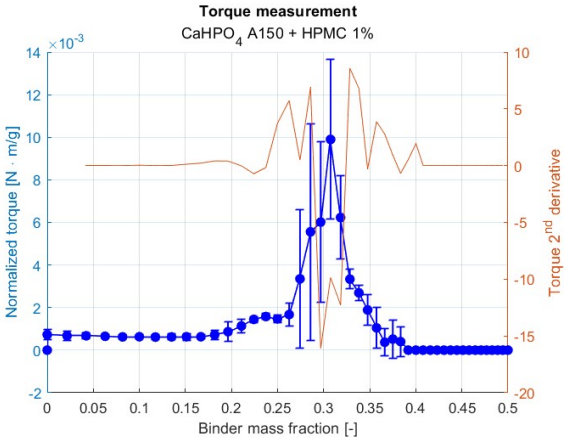

(c) $CaHPO_4$ A150 - HPMC 1%

FIGURE 3.3: Torque measurement for $CaHPO_4$ A150 powder

3.2 Hardness - strain rate relation

In order to investigate the rate-dependent mechanical response of partially saturated powders, the hardness values obtained from dynamic ball indentation were analyzed as a function of strain rate.

Hardness H is calculated as $H = \frac{F_{max}}{A_{cap}}$, and represents a measure of the resistance of the powder bed to localized penetration. While hardness is an intrinsic property of the system, its magnitude may vary depending on the rate at which the deformation is imposed, particularly in wet materials where there is a complex interaction between powder and binder.

The strain rate $\dot{\gamma}$ represents the rate of deformation applied to the powder during indentation. In literature several ways of describing the strain rate are proposed, Santomaso in his work (Santomaso, 2025), improved the usual definition adopted in ball

indentation method $\dot{\gamma} = \frac{v_0}{R_b}$ (which used the indenter radius R_b) by using the velocity and penetration of the indenter at the maximum force point, the new proposed definition is:

$$\dot{\gamma} = \frac{v_{Fmax}}{h_{Fmax}} \tag{3.1}$$

.

Defining the shear rate in this new way is highly relevant when comparing it with hardness which, by definition, is evaluated at the same force point.

The experimental results are presented in figures 3.4, 3.5, 3.6, 3.7, and are divided by powder type, in each plot different colors represent different binder quantity in the sample, while the shape of markers represents the consolidation pressure of the sample.

All powder-binder hardness vs strain rate curves present a linear trend, despite of the consolidation pressure and binder quantity (that is an intrinsic way of representing the wetting regimes), just $CaHPO_4$ A150 present a unique trend, in which there are two different linear functions, one in which are collected the points at low saturation ($y_b < [15\% - 25\%]$), and one line that collect points at higher saturation($y_b > [15\% - 25\%]$).

This could mean that $CaHPO_4$ A150 has a unique response to wetting with respect to the other studied powders.

It can be observed that, for indentation trials performed at the same binder content, higher hardness values are obtained at higher consolidation pressures. This highlights the general tendency of hardness to increase with increasing consolidation pressure: as expected, a more compacted powder offers greater resistance to indenter penetration.

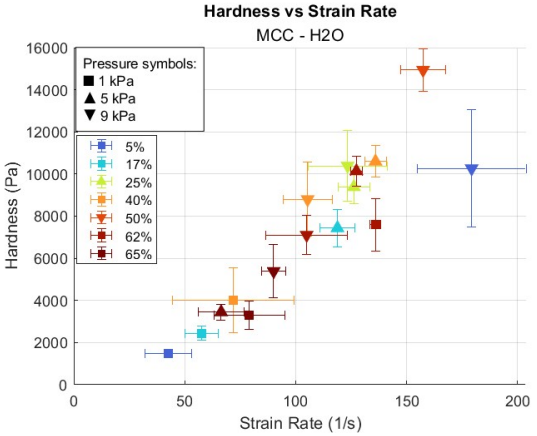

(a) MCC - H_2O

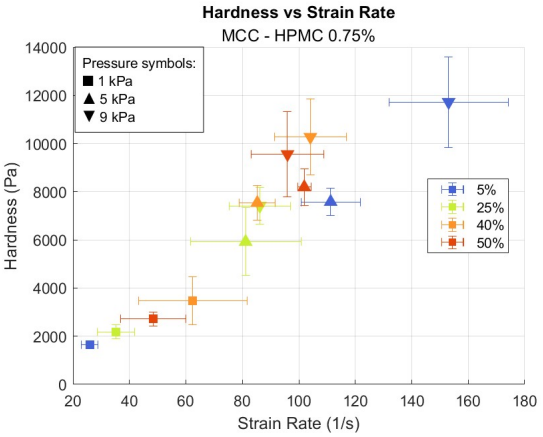

(b) MCC - HPMC 0.75%

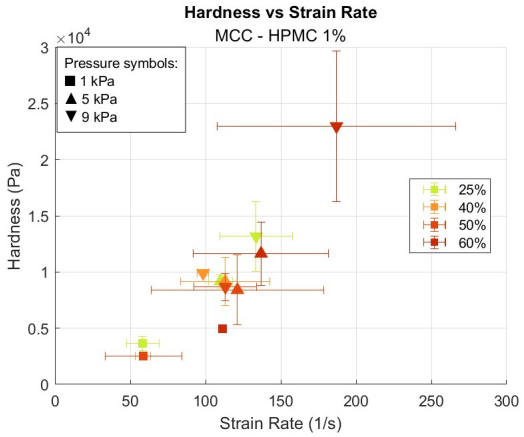

(c) MCC - HPMC 1%

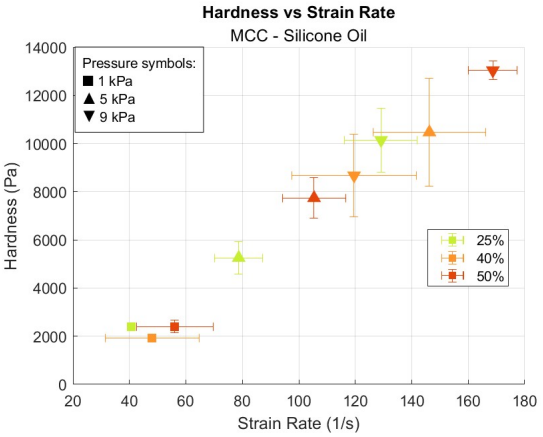

(d) MCC - Silicone oil

FIGURE 3.4: Hardness vs strain rate relation for MCC powder

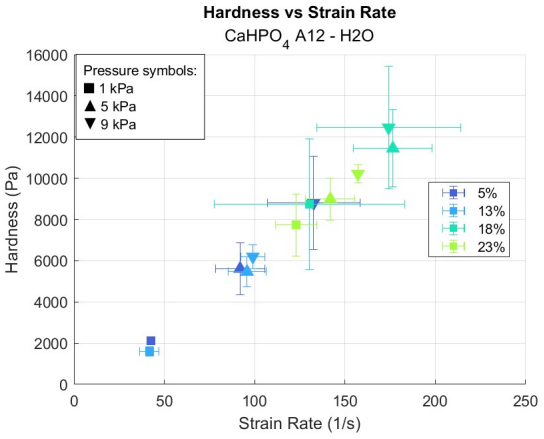

(a) $CaHPO_4$ A12 - H_2O

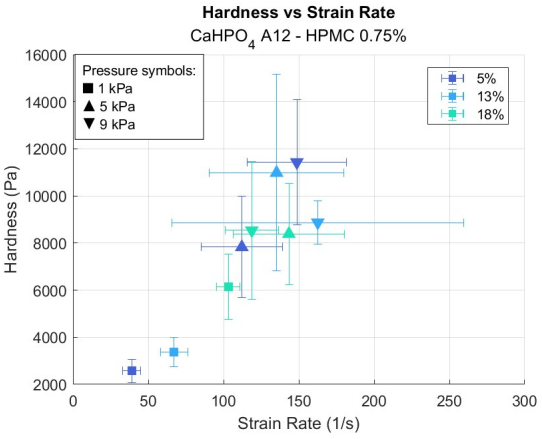

(b) $CaHPO_4$ A12 - HPMC 0.75%

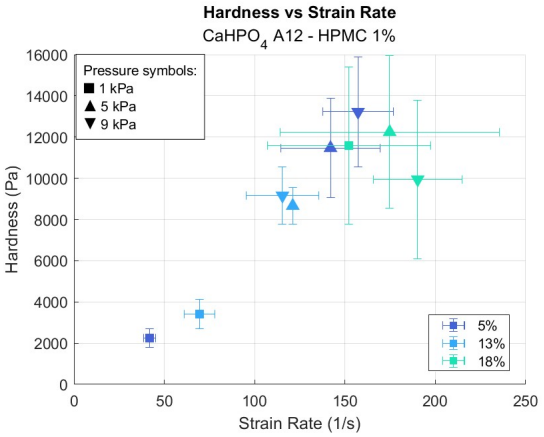

(c) $CaHPO_4$ A12 - HPMC 1%

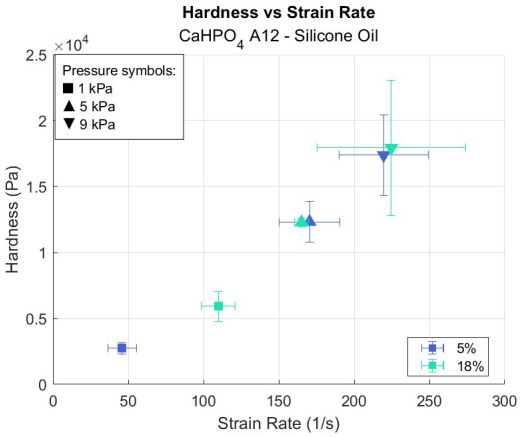

(d) $CaHPO_4$ A12- Silicone oil

FIGURE 3.5: Hardness vs strain rate relation for $CaHPO_4$ A12 powder

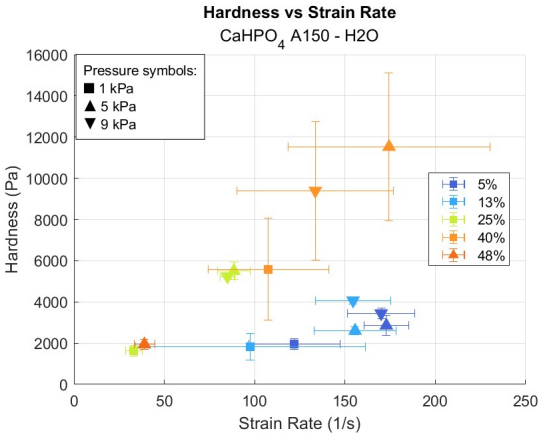

(a) $CaHPO_4$ A150 - H_2O

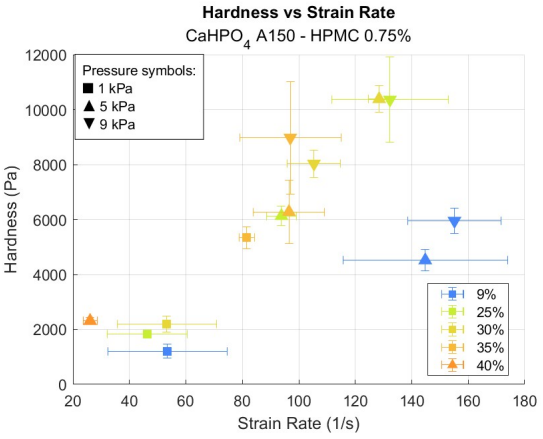

(b) $CaHPO_4$ A150 - HPMC 0.75%

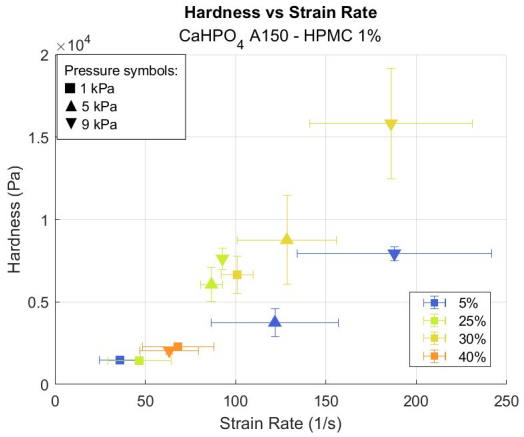

(c) $CaHPO_4$ A150 - HPMC 1%

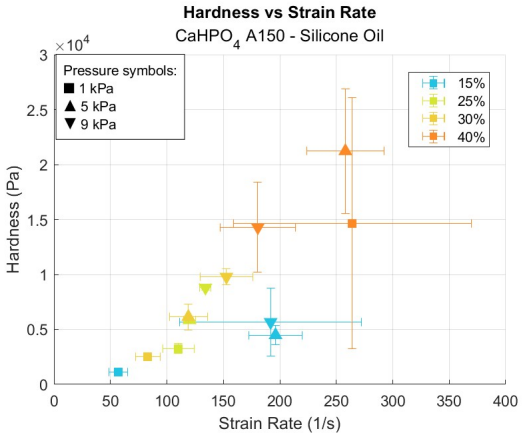

(d) $CaHPO_4$ A150 - Silicone Oil

FIGURE 3.6: Hardness vs strain rate relation for $CaHPO_4$ A150 powder

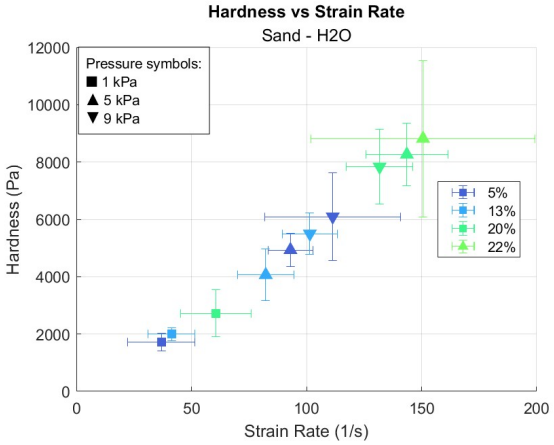

Sand - H_2O

FIGURE 3.7: Hardness vs strain rate relation for silica sand

Further analyzing the hardness data is interesting to notice, in Figure 3.8, that the standard deviation of the measured hardness exhibits a clear linear dependence with the hardness itself. This behavior can be understood from two perspectives. First, a constant relative error of the measuring instrument implies that the absolute standard deviation increases proportionally with the measured signal. Second, for granular materials, regions with different local strengths become more pronounced as the mean hardness increases, meaning that when hardness increases (for example, due to higher powder consolidation), some regions become much stronger while others remain weaker, amplifying the local differences and consequently increasing the spread of the measured values. Therefore, the observed linear growth of the standard deviation with hardness reflects both intrinsic material heterogeneity and the proportionality imposed by measurement limitations.

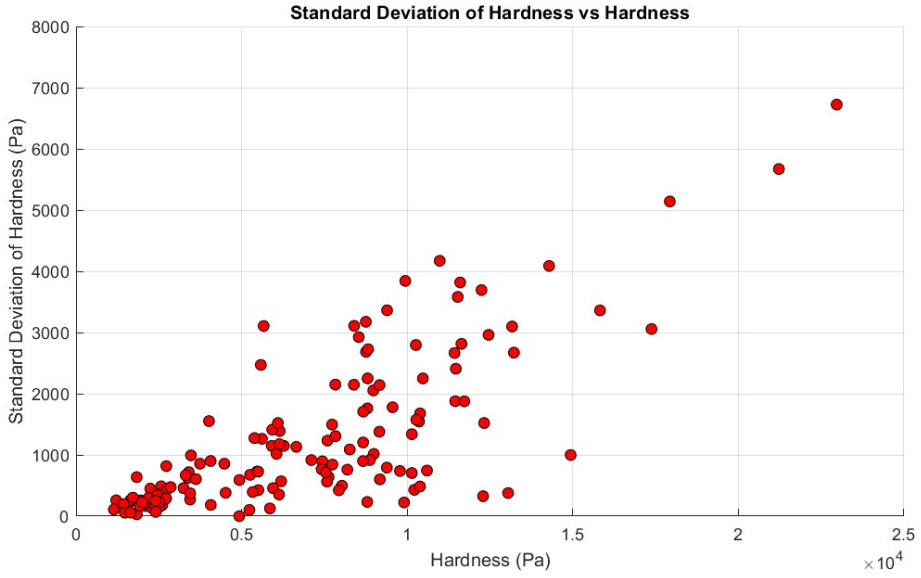

FIGURE 3.8: Hardness standard deviation vs Hardness

3.3 3D representation of hardness dependence

As observed in Fig. 3.6(a-d), for $CaHPO_4$ A150 Hardness does not exhibit a clear linear dependence on strain rate alone, in contrast to what is seen for other materials. A more informative representation is provided in the three-dimensional plot reported in Fig. 3.9, where the binder content (expressed as binder mass fraction $y_b = \frac{bindermass}{totalmass}$) is introduced as a third axis.

In this representation, the experimental points lie approximately on a plane, indicating that hardness increases linearly with both the strain rate and the binder quantity.

The quality of the fit is confirmed by the good coefficient of determination (R^2), and the corresponding plane equations are summarized in Table 3.1.

This behavior is not unique to $CaHPO_4$ A150. A similar trend is observed for MCC, $CaHPO_4$ A12, and sand, as illustrated in Figs. 3.5(a-d), 3.4(a-d), and 3.7. For all these systems, when binder content is incorporated as a third coordinate, the data collapse onto a plane that satisfactorily represents the experimental values. The fitted plane equations and statistical parameters for these materials are reported in the corresponding tables.

The fact that hardness can be described as a bilinear function of strain rate and binder fraction strongly suggests that the mechanical strength of partially saturated powders is governed by two independent, yet complementary, contributions: the rate-dependent frictional and inertial resistance of the particle assembly, and the cohesive forces induced by the amount of liquid binder present in the system. Such a combined description is not only physically consistent, but also provides a practical framework to predict powder strength across different moisture regimes. However, one important variable is not explicitly captured in this representation: the consolidation pressure. In Figs. 3.9, 3.11, 3.10, and 3.12, data from different consolidation pressures are shown, with points corresponding to each pressure connected by a line. This highlights that, while hardness can be reasonably predicted as a function of strain rate and binder fraction, the explicit dependence on consolidation pressure remains unresolved and requires further investigation.

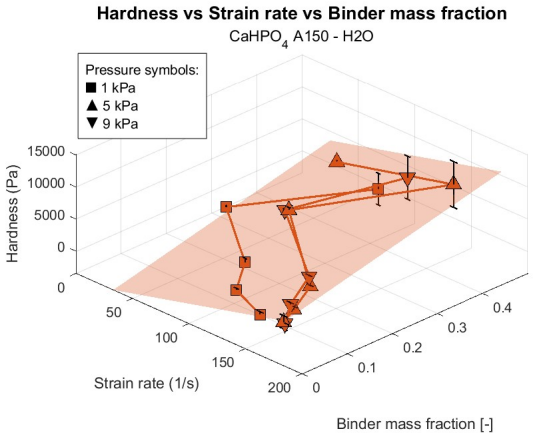

(a) $CaHPO_4$ A150 - H_2O

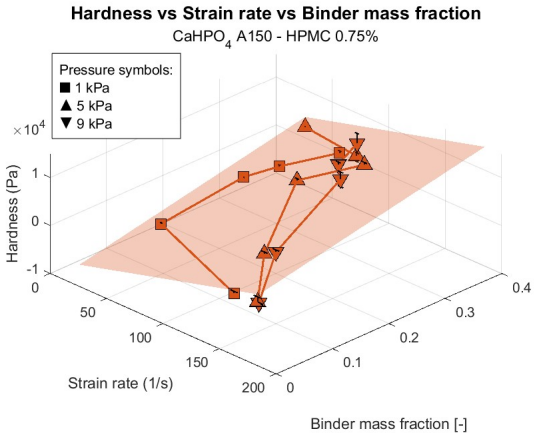

(b) $CaHPO_4$ A150 - HPMC 0.75%

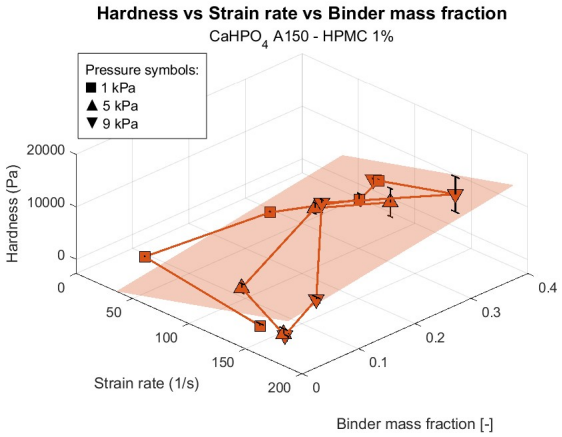

(c) $CaHPO_4$ A150 - HPMC 1%

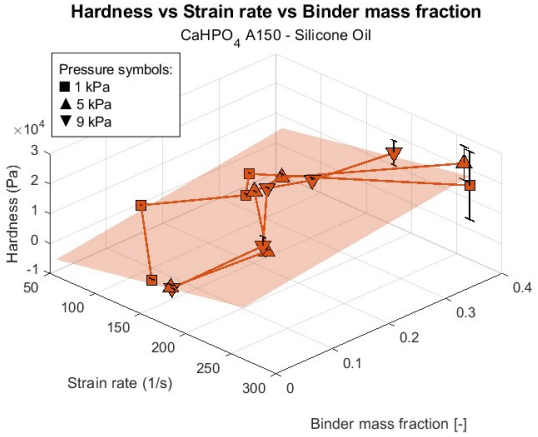

(d) $CaHPO_4$ A150 - Silicone oil

FIGURE 3.9: Hardness vs strain rate and binder mass fraction for $CaHPO_4$ A150 powder

Binder	**Plane equation**	R^2
H_2O	$H = 46.2538 \cdot \dot{\gamma} + 17258.7947 \cdot y_b - 4992.8899$	0.7437
HPMC 0.75%	$H = 65.4221 \cdot \dot{\gamma} + 24701.1353 \cdot y_b - 7163.2955$	0.7213
HPMC 1%	$H = 58.1135 \cdot \dot{\gamma} + 17115.4777 \cdot y_b - 4798.7641$	0.5605
Silicone oil	$H = 57.085 \cdot \dot{\gamma} + 25756.97 \cdot y_b - 7655.25$	0.8725

TABLE 3.1: Planes equation and R^2 for $CaHPO_4$ A150

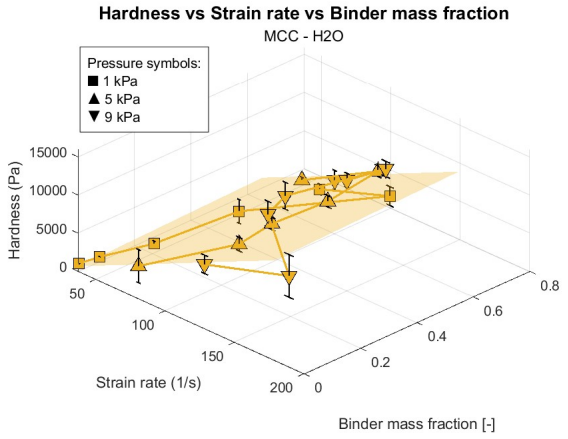

(a) MCC - H_2O

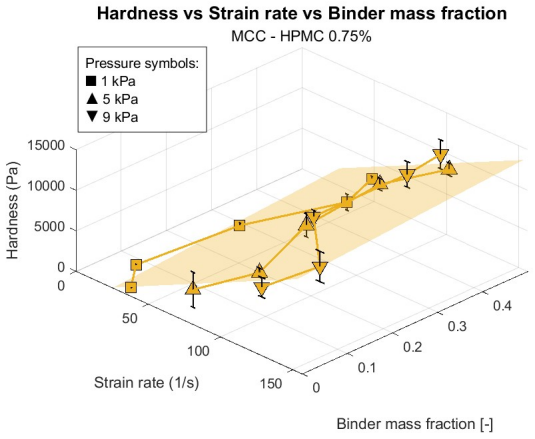

(b) MCC - HPMC 0.75%

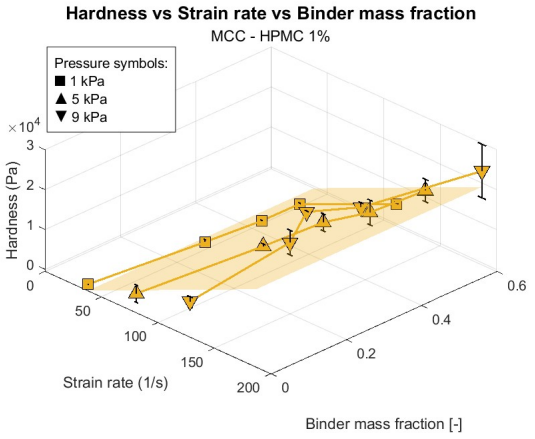

(c) MCC - HPMC 1%

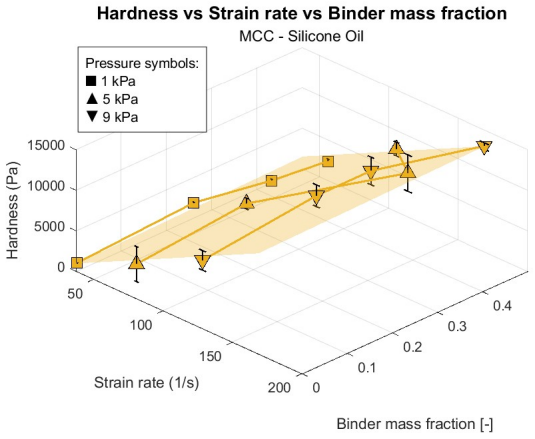

(d) MCC - Silicone oil

FIGURE 3.10: Hardness vs strain rate and binder mass fraction for MCC powder

Binder	**Plane equation**	R^2
H_2O	$H = 88.016 \cdot \dot{\gamma} + 1080.3 \cdot y_b - 2621.6$	0.8511
HPMC 0.75%	$H = 89.054 \cdot \dot{\gamma} + 4130.5 \cdot y_b - 2209.3$	0.9182
HPMC 1%	$H = 131.01 \cdot \dot{\gamma} - 4.6573 \cdot y_b - 5482.9$	0.8585
Silicone oil	$H = 87.208 \cdot \dot{\gamma} + 1128.2 \cdot y_b - 2288.4$	0.9814

TABLE 3.2: Planes equation and R^2 for MCC

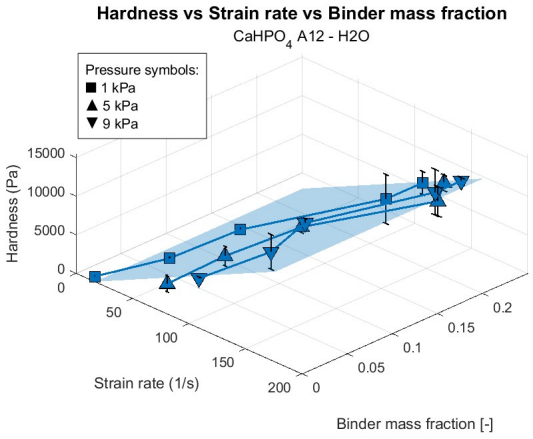

(a) $CaHPO_4$ A12 - H_2O

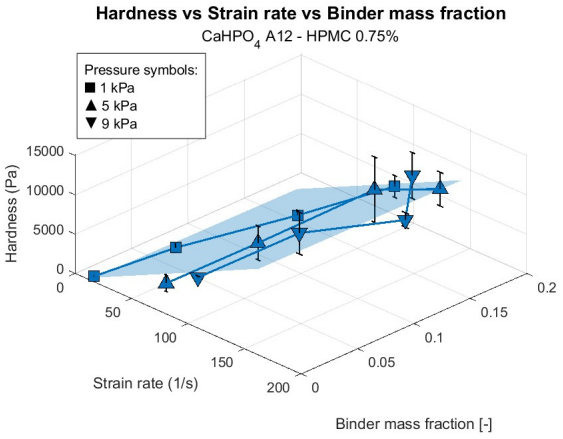

(b) $CaHPO_4$ A12 - HPMC 0.75%

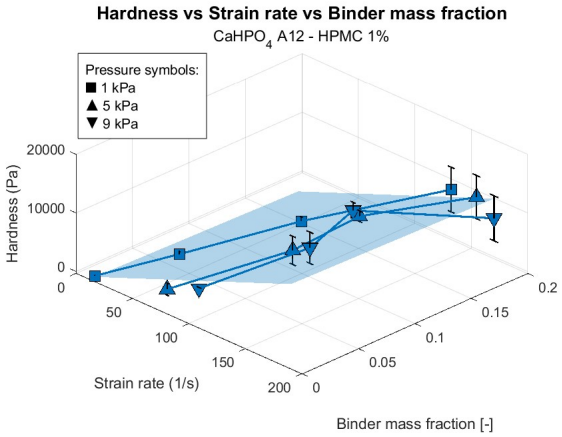

(c) $CaHPO_4$ A12 - HPMC 1%

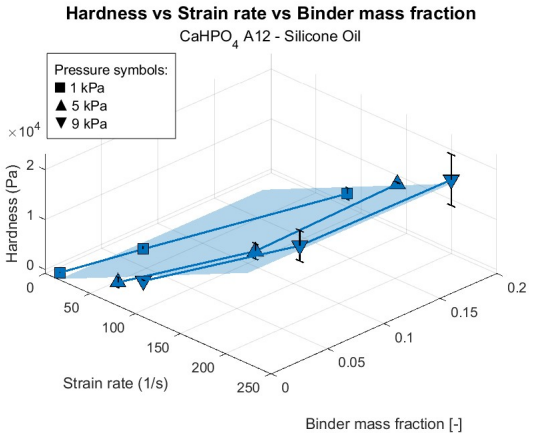

(d) $CaHPO_4$ A12 - Silicone oil

FIGURE 3.11: Hardness vs strain rate and binder mass fraction for $CaHPO_4$ A12 powder

Binder	**Plane equation**	R^2
H_2O	$H = 73.124 \cdot \dot{\gamma} + 432.47 \cdot y_b - 1223.6$	0.9851
HPMC 0.75%	$H = 71.594 \cdot \dot{\gamma} - 1148.3 \cdot y_b - 680.48$	0.8770
HPMC 1%	$H = 78.562 \cdot \dot{\gamma} - 4562.4 \cdot y_b - 817.14$	0.8718
Silicone oil	$H = 86.345 \cdot \dot{\gamma} - 1181.8 \cdot y_b - 2024.9$	0.9780

TABLE 3.3: Planes equation and R^2 for $CaHPO_4$ A12

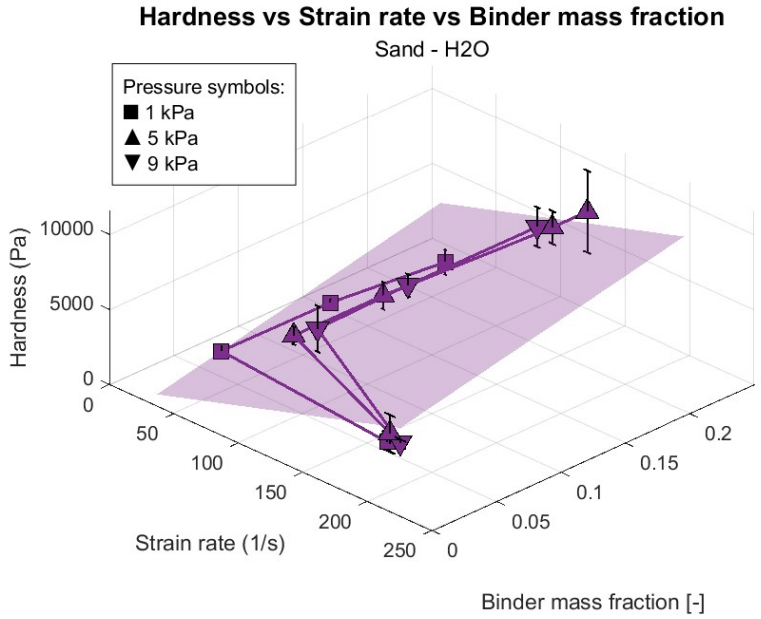

FIGURE 3.12: Hardness vs strain rate and binder mass fraction for sand powder

Binder	**Plane equation**	R^2
H_2O	$H = 27.035 \cdot \dot{\gamma} + 19053 \cdot y_b - 222.43$	0.6545

TABLE 3.4: Planes equation and R^2 for sand

Furthermore, it can be observed that the extrapolated planes predict negative hardness values when both $\dot{\gamma}$ and y_b approach zero. This outcome is physically unrealistic. A more plausible interpretation is that, at very low strain rates, the linear dependence assumed in the fitting model no longer holds. Instead, the response is expected to deviate from linearity and gradually curve, asymptotically approaching a hardness value close to zero.

For now this remain unknown since there are technical limitation in reaching low strain rate with the dynamic ball indentation, since there is no possibility in fixing the desired value of strain.

3.4 Torque and Hardness comparison

As anticipated in Chapter 3.1, the torque measured with the torque rheometer is compared with the hardness obtained from DBI measurements.

From a theoretical perspective, the hardness values obtained by dynamic indentation can be related to the torque measured by the rheometer. Both quantities represent measures of the material's resistance to deformation, although they are probed at different scales and under distinct loading conditions.

In torque rheometry, the measured torque reflects the overall resistance of the powder bed to shear induced by the rotating blades. This resistance arises from the combined contributions of interparticle friction, cohesive forces generated by liquid bridges, and the viscous effects of the binder. Conversely, indentation hardness H, defined as the mean pressure required to plastically deform the material beneath the indenter, is inherently a local property. It characterizes the response of a confined volume of material (the indented zone and the surrounding powder), which may not fully capture the bulk behavior. However, if the sample preparation ensures homogeneity and reproducibility, it is reasonable to assume that the indented region can serve as a representative element of the overall system.

Thus, while torque rheometry integrates the macroscopic response of a larger powder volume under continuous shear, indentation probes a localized response under concentrated loading.

Furthermore also time scales between this two methods are different, results given by torque rheometer are averaged over some seconds (15 seconds in our experiments), after an homogenization phase, this is done to remove fluctuations given by the non constant resistance of the powder, smoothing all the possible fast phenomena that occurs during the impact with the blades, doing this brings to a sort of steady value. On the other hand dynamic ball indentation's time scale is shorter, in the order of milliseconds and is never stationary, allowing to capture the fast phenomena that occurs during impacts.

Despite these methodological differences, the dominant physical mechanisms, frictional contacts, capillary cohesion, and viscous dissipation, are common to both approaches.

In Fig. 3.13 torque and hardness are compared on the base of the binder fraction in the sample, resulting in a qualitative correspondence.

This qualitative correspondence is clearly visible in Fig. 3.13(a–c), where higher torque values are associated with higher indentation hardness. Especially peaks occurs at the same binder quantity values.

It can therefore be stated that the general shape of the profiles appears to be independent of the measurement timescale. This suggests that the properties measured under steady conditions with the torque rheometer can effectively reflect the mechanical response of the powder bed during a rapid impact event. It would, however, be

interesting to investigate whether the magnitude of the hardness values could provide additional information compared to torque, as the DBI test more closely reproduces the dynamic conditions occurring in a high-shear wet granulator (HSWG). So far, only the qualitative correspondence between the two techniques has been addressed, but this aspect could represent a valuable direction for future studies.

Nevertheless, some caution must be exercised when directly comparing the two methods. The shapes of the torque profiles obtained from the rheometer are not always preserved in the corresponding indentation results, as shown in Fig. 3.13(d), this can have different explanations, the first one, is that the shape is not preserved because of a lack in points in the DBI curve, for example in Fig. 3.13(d) probably adding a point with binder mass fraction between 0.13 and 0.18 will have shown the peak that is seen on the torque profile, this is a simple and effective explanation, or another possibility is that the difference between the curves can be due to localized heterogeneity in the powder bed used in the dynamic ball indentation, this heterogeneity cause an error on the hardness value and mismatch between profiles, this should be avoided if the sample preparation is performed with caution, mixing, pouring and compacting the powder following the standard procedure.

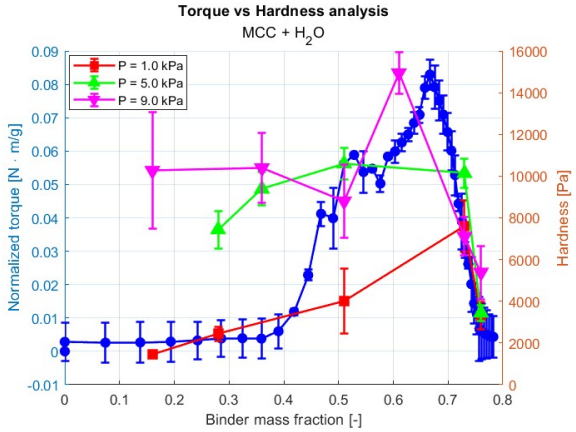

(a) MCC - H_2O

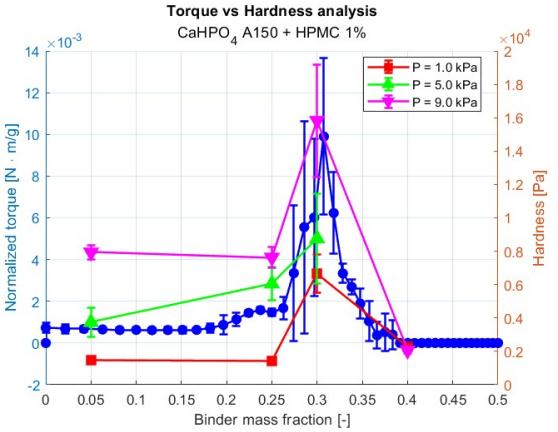

(b) $CaHPO_4$ A150 - HPMC 1%

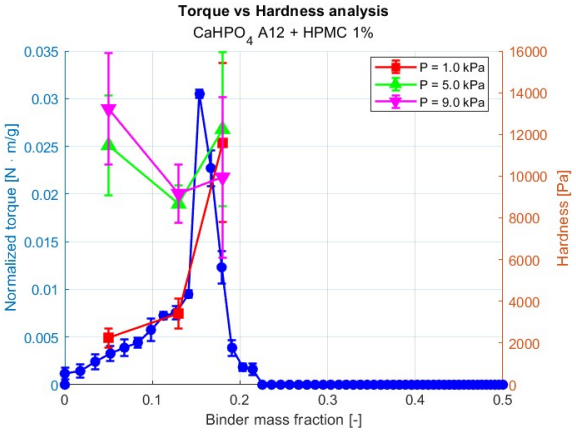

(c) $CaHPO_4$ A12 - HPMC 1%

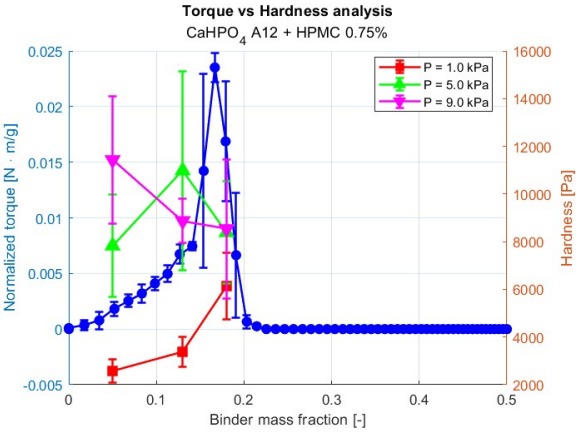

(d) $CaHPO_4$ A12 - HPMC 0.75%

FIGURE 3.13: Normalized torque vs hardness

Furthermore, torque rheometry provides a semi-continuous measurement across the entire range of binder additions, thus allowing high resolution on the profiles of powder resistance. In contrast, indentation requires discrete tests at each binder content: obtaining a complete curve would therefore be more time consuming, and identifying transitions (such as shoulders in the curve or inflection points where the second derivative is equal to zero) would become very difficult.

On the other hand, indentation offers an important advantage over torque rheometry: it allows a direct assessment of the effect of powder bed compaction. As shown in Fig. 3.13(a–d), indentation hardness can be evaluated at different consolidation stresses. In general, increasing the consolidation of the powder leads to higher hardness values, this is accentuated between low consolidation (1 kPa) and higher ones (5-9 kPa), while between 5 kPa and 9 kPa this trend is attenuated and sometimes curves overlap between each other.

The opportunity of evaluating response at different consolidation values provide crucial insights into the behavior of wet powders under compression. This aspect is highly relevant for operations where mechanical consolidation plays a key role, such as tableting, extrusion, or pelletization, and cannot be captured by torque rheometry alone.

3.5 Hardness–strain rate relation through the Inertial number

Returning to the characterization of the powder bed response under applied shear, an alternative way to interpret the hardness–strain plot is through the use of the inertial number (I), defined as

$$I = d_p \dot{\gamma} \sqrt{\frac{\rho_p}{P}} \tag{3.2}$$

where $\dot{\gamma}$ is the applied strain rate, d_p is the mean particle diameter, ρ_p is the powder density and P is the pressure that correspond at the evaluated penetration point, that can be calculated as $P = \rho_p g h_{F_{max}}$, where g is the gravitational acceleration and $h_{F_{max}}$ is the dimensionless penetration at the maximum force point.

The inertial number written in this particular way is useful in dynamic indentation because it accounts not only for the imposed strain rate, but also for the confining pressure of the powder that resists the indenter motion. Compared to the simpler dimensionless shear rate

$$\dot{\gamma}^* = \dot{\gamma} \sqrt{\frac{d_p}{g}} \tag{3.3}$$

the inertial number provides a more comprehensive description of the flow regime during indentation.

According to the granular flow framework (MiDi, 2004; Hurley & Andrade, 2015), three main flow regimes can be distinguished based on the inertial number:

- Quasi-static regime ($I < 10^{-3}$): deformation is nearly rate-independent and dominated by interparticle frictional contacts.
- Dense or intermediate regime ($10^{-3} < I < 10^{-1}$): both frictional and inertial mechanisms contribute to the response.
- Collisional regime ($I > 10^{-1}$): the behavior is dominated by collisions and inertial dynamics.

In literature, many studies have investigated the relationship between the effective friction coefficient, μ_f and the inertial number I, since this framework is widely used

to describe the rheological behavior of granular materials across different flow regimes. These works consistently show that in the quasi-static and dense regimes μ_f is nearly independent of I, while in the collisional regime it increases monotonically with I.

In this work, the effective friction coefficient was not measured. Instead, following the approach proposed by Santomaso (2025), the hardness H was analyzed as a function of the inertial number, with the aim of exploring whether the response of powders under dynamic indentation can be interpreted within the same inertial framework. It should be noted that in Santomaso's study a slightly different definition of I was adopted, namely $I = \dot{\gamma} d_p \sqrt{\frac{\rho_p}{H}}$, that used the values of hardness instead of pressure.

In Fig. 3.14 are reported all the points collected for the four powders, with the abscissa in logarithmic scale. Two different behavior can be identified. At low I the Hardness is almost constant, meaning that there is no inertial effect on the powder.

In this first region there is a higher density of point in which the consolidation pressure is $1kPa$, the lowest studied, this because there is an higher penetration due to the loose compaction that is reflected directly on the inertial number, and also indirectly in the shear rate. Differently for $CaHPO_4$ A150, in this initial region we find all the three studied consolidation pressures.

After this constant trend there is a linear dependence between H and I, the only material in which the points are more scattered in this second zone is $CaHPO_4$ A150.

The difference in behavior as a function of the inertial number can be attributed to different flow regimes, even if the transition zone is not unique but depend on the material.

When the hardness is not function of the Inertial number, the regime is quasi-static or intermediate and this means that in this regime the inertial contributions are negligible compared to interparticle friction.

In the collisional regime, hardness grows linearly with the inertial number reflecting the growing importance of collisional dynamics.

It is also worth noting that, in Fig. 3.14, the plotted points are values measured using different binder and saturation regimes (pendular, funicular, and capillary).

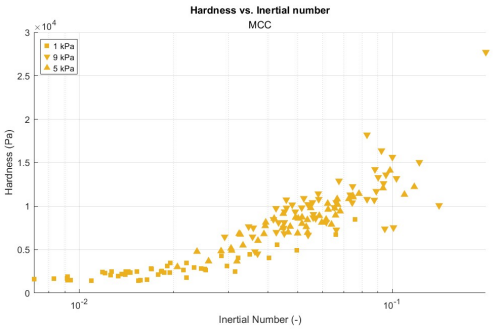

(a) MCC

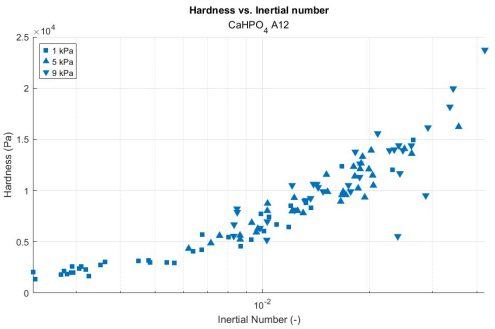

(b) $CaHPO_4$ A12

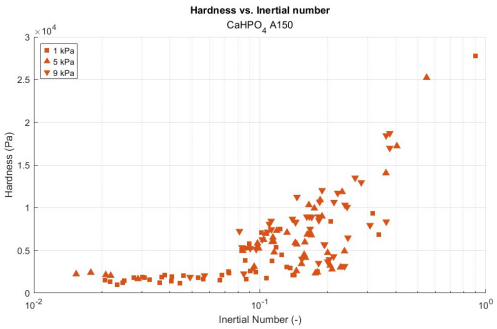

(c) $CaHPO_4$ A150

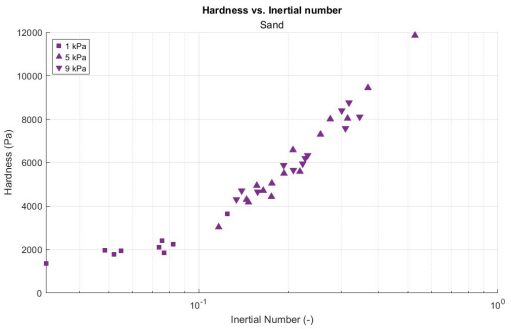

(d) Sand

FIGURE 3.14: Hardness vs Inertial number, divided by powder type

In Figure 3.15 are plotted all the four powders, marked by different colors.

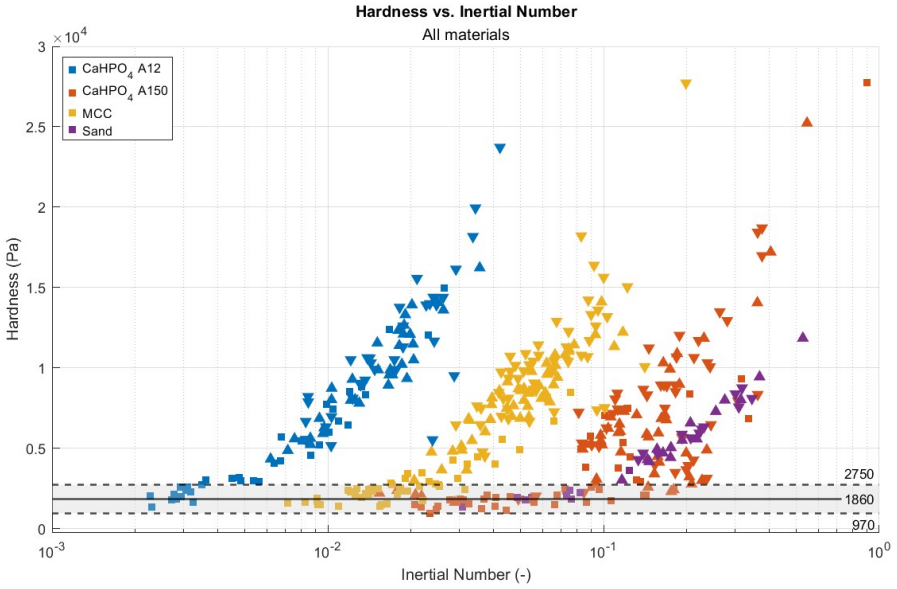

FIGURE 3.15: Hardness vs Inertial number, unified plot for all powder types

As can be seen, all the Hardness values in the quasi-static regime have approximately the same value (H=[970, 2750], that is a small range compared to the absolute scale

that cover the Hardness variable), this is interesting because means that in this regime the powder resistance to penetration is unique, despite of powder and binder characteristics and also consolidation pressure considering that $CaHPO_4$ have points at different consolidation pressure in this zone.

In future studies could be interesting modifying the Inertial number, substituting the powder diameter outside the squared root with another characteristic length with the aim of collapsing the data.

3.6 Dynamic force vs Capillary number

In this work the evaluated hardness H is also employed as an estimate of the dynamic yield stress, σ_D, a quantity that is relevant for predicting high–shear wet granulation behavior (see Chapter 1.2.5). Iveson and co-workers, (Iveson et al., 2002) listed the principal parameters that can affect the dynamic yield stress:

- mean particle size d_p,
- binder surface tension γ,
- binder viscosity η,
- solid–liquid contact angle θ,
- strain rate $\dot{\gamma}$,
- internal friction coefficient μ_f,
- packing fraction Φ,
- liquid saturation S.

They also suggested that shape of individual particles and shape of the entire particle size distribution will have a significant impact, but that they are also difficult to be incorporated in a single parameter.

After a dimensional analysis, Iveson proposed the relation:

$$\frac{\sigma_D d_p}{\gamma \cos\theta} = f\left(\frac{\eta\dot{\gamma} d_p}{\gamma \cos\theta}, \mu_f, S, \Phi\right) \tag{3.4}$$

where the left-hand side is the dimensionless strength Str^* and the first argument on the right-hand side is the capillary number Ca. In the present study, and following previous authors, complete wetting ($\cos\theta = 1$) was assumed; this simplifies the computation of both Str^* and Ca.

Furthermore in this work is assumed that particle diameter is not affected by binder addiction, that is reasonable for silica sand and calcium phosphate, while is a stronger assumption for MCC that can grow in size for the absorption of water.

Iveson and co-workers in their work observed that the relation between Str^* and Ca develops in two regions, the first at low Ca in which there is no effect of Ca on Str^*, and a second zone in which the relation between the two variables is exponential. Overall can be described by the equation

$$Str^* = 5.3 + 280Ca^{0.58} \tag{3.5}$$

this trend, reported for glass beads with different binders, is shown in Fig. 3.16.

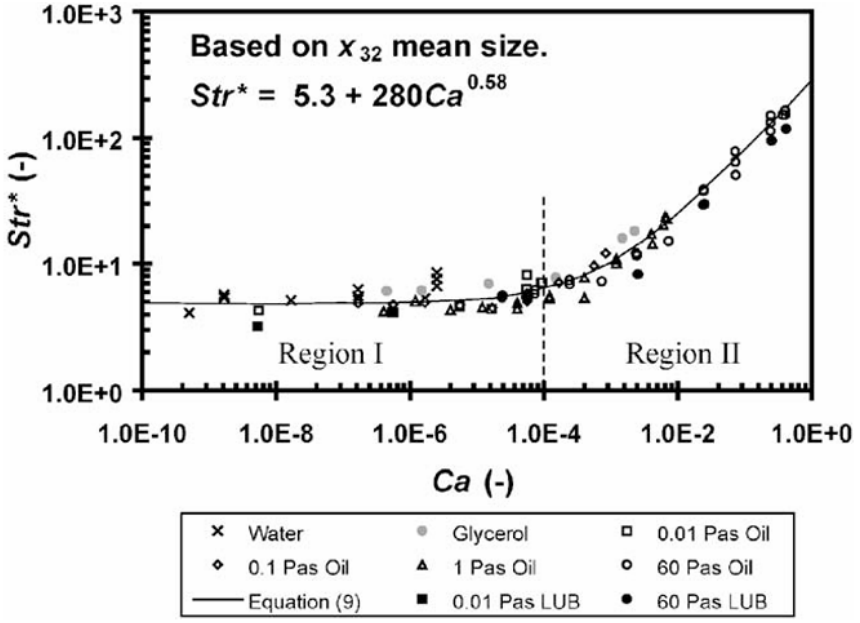

FIGURE 3.16: Str^* vs Ca relation for glass ballottini and several binders, from Iveson et al. (2002)

In literature a lot of variants of the capillary number are proposed, a comprehensive review of them all is provided by Guo et al.,(Guo et al., 2022), for the present work the definition provided by Iveson is keep without alteration, also to have a comparison already validated in literature.

Figure 3.17 shows the experimental results of this work, where each point represents the mean of three independent trials. Marker colour indicates the powder type, while marker shape identifies the binder. Iveson equation, (Eq.3.5), is reproduced as a black reference line.

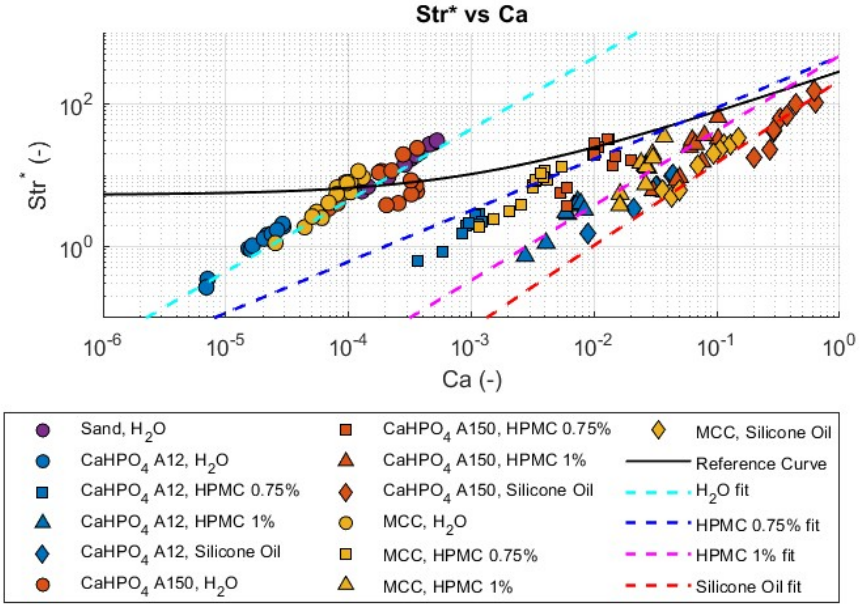

FIGURE 3.17: Experimental Str^* vs Ca relation compared with the Iveson correlation.

A first inspection of Fig.3.17 reveals that the trend reported by Iveson is not well captured. Instead, the points clearly separate according to the viscosity of the binder. This suggests that the dominant grouping factor is not the capillary number alone, but rather the viscous contribution of the binder. From this analysis data are fitted separately by the binder type, to understand better the relation between the variables.

Since the model is unknown, several candidate functions were tested, including linear and power-law relations. To objectively compare their performance, two statistical criteria were employed: the coefficient of determination (R^2) and the Akaike Information Criterion (AIC).

The R^2 indicates the fraction of the experimental variability explained by the model.

The AIC, on the other hand, evaluates the trade-off between fitting accuracy and model parsimony. It penalizes unnecessary complexity and enables direct comparison between different non-linear models or fitting strategies. Unlike R^2, the AIC has not an absolute scale, it ranges from $-\inf$ to $+\inf$. A lower absolute value of AIC value corresponds to a model that better reproduces the data, but its absolute value has meaning only when compared within the same dataset. Therefore, it is useful for selecting the best model, but it does not provide a direct quantification of the goodness of fit. For that purpose, R^2 is generally more informative, even though its interpretation is less straightforward for non-linear models.

Overall, combining R^2 and AIC allows for the identification of the most suitable model among those considered, while simultaneously providing a quantitative measure of its goodness of fit.

In table 3.5, are collected the best fitted equations with the R^2 and AIC.

TABLE 3.5: Fitted equations with relative R^2 and AIC

Binder	**Fitted equation**	R^2	**AIC**
H_2O	$Str^* = 44506 \cdot Ca$	0.751	144
HPMC 0.75%	$Str^* = 466 \cdot Ca^{0.72}$	0.687	112.45
HPMC 1%	$Str^* = 476 \cdot Ca^{1.05}$	0.703	133.1
Silicone oil	$Str^* = 218 \cdot Ca^{1.16}$	0.907	119.7

From this perspective, there is no master curve in which all data collapse, but there are instead 4 curves, that have approximately a linear trend, each associated with a different binder viscosity. Interesting to notice that even if the solutions with HPMC, especially at the higher concentration have a shear-thinning behavior, data including this binder dispose them self along a line, meaning that the non linear relation between viscosity and shear rate, shown in Fig.2.14 is attenuated.

The division of data by the viscosity of the binder suggest that in order to have a collapse of data, along one single line there is the needs of removing the viscosity from the abscissa, or attenuate its effect, this will be studied later on.

To reduce variability due to consolidation, Fig. 3.18 reports data averaged over different consolidation pressures.

This decision was taken in order to make the results more comparable with those of Iveson and co-workers, who prepared the compressed cylinders at constant bed porosity. In our case, averaging the trials at different consolidation pressures is equivalent, since consolidation pressure and bed porosity are directly correlated.

From Fig.3.18, the trials related to the sand powder have been removed since the dataset do not comprehend a variety of binder but just water, and so is not possible to retrieve any further information from the Str^* vs Ca curve for it.

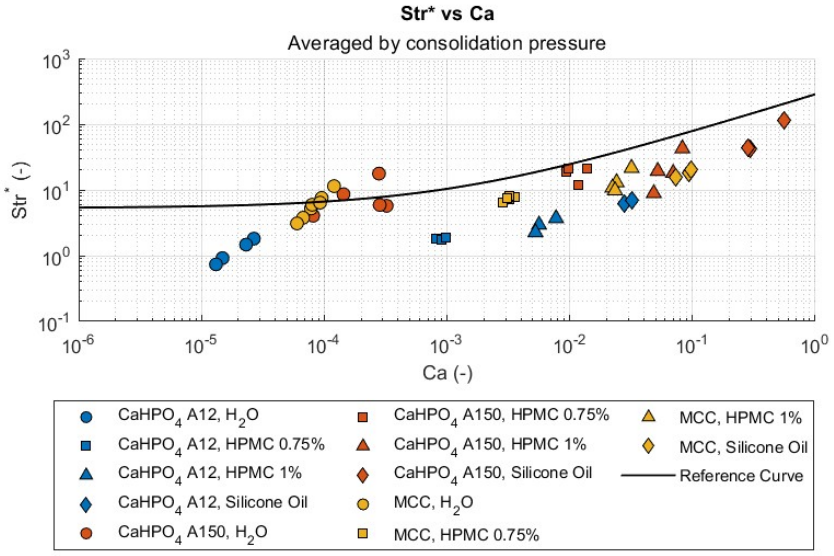

FIGURE 3.18: Str^* vs Ca averaged by consolidation pressure

The averaged dataset in Fig. 3.18 shows a clearer behavior, more in line with Iveson's original observations.

Furthermore if we average data over binder saturation, we get the result in figure 3.19, where at each point corresponds the mean between different consolidation pressures and binder saturation.

Also in this case, the procedure is intended to make the results more comparable with those of Iveson et al., since in their work the saturation of the samples was kept constant.

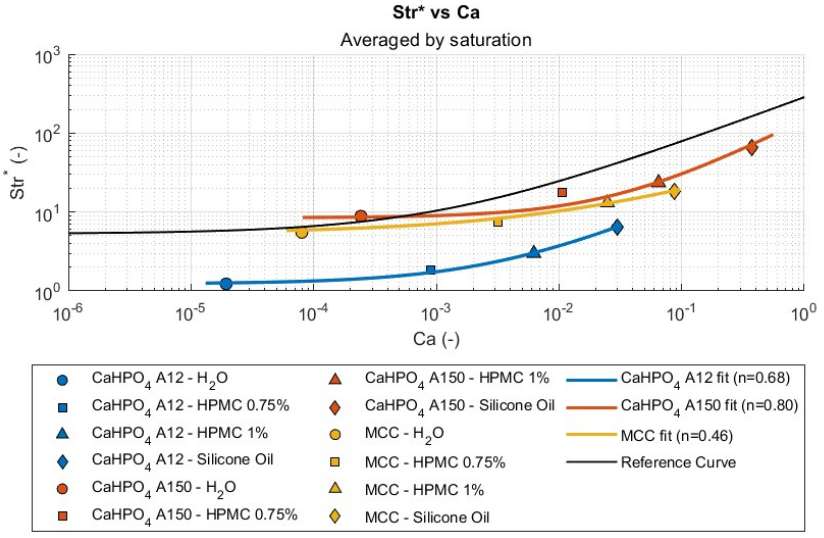

FIGURE 3.19: Str^* vs Ca averaged by saturation

The similarity of Fig. 3.19 to the trends reported by Iveson suggests that a power-law model is appropriate. Data were fitted using the form:

$$Str^* = k_1 + k_2\, Ca^n, \tag{3.6}$$

The coefficients of the retrieved curves are shown in Tab.3.6 divided by powder type

TABLE 3.6: Model parameters divided by powder, and R^2_{adj}

Powder	k_1	k_2	**n**	R^2_{adj}
$CaHPO_4$ A150	8.451	139.168	0.8	0.850
MCC	5.371	40.751	0.458	0.759
$CaHPO_4$ A12	1.229	57.267	0.680	0.970

This exponential dependence confirms Iveson's explanation: at low $Ca < 10^{-4}$, Str^* is constant and viscous effects are negligible, while at higher Ca viscous stresses significantly contribute to strength.

The fact that there is not a unique master curve, highlight the possibility of some missing parameters in the relation, in fact in other experimental campaigns Sweat et al. (2016, 2017), found that particle size distribution and aspect ratio of the studied powder has an influence on the position of the curves, this might be explaining the relative shift in position between powder types, but those were not verified and this could be a suggestion for future work.

In conclusion, the characteristic curve reported by Iveson was successfully reproduced. However, the present work emphasizes that both consolidation pressure and binder saturation must be considered in the formulation, since the measured Str^* values vary significantly with these parameters.

The Dynamic Ball Indentation (DBI) method offers the advantage of investigating powders over a wider range of saturation levels. This is possible because the powder is confined within a rigid cylinder, in contrast to Iveson's experiments, which relied on unconfined compressed powder compacts. In the latter case, sufficient cohesion was required to maintain the integrity of the powder bed, a condition that inherently limited the accessible range of consolidation pressures and saturation degrees.

3.7 Inertial number relation

From the analysis of Fig. 3.17, it was observed that neither consolidation pressure nor liquid saturation are well captured by the exponential relation typically used to correlate

Str^* and Ca. Instead, a clearer linear dependence emerges if viscosity is removed from the abscissa. To further investigate this behavior using a more established dimensionless number, the dimensionless strength Str^* was plotted against the inertial number I, that was introduced in Chapter 3.5, since I does not contains the viscosity among its variables. Starting from Eq. 3.2, and recalling that $P = \rho_p g h_{F_{max}}$ we have:

$$I = \dot{\gamma} d_p \sqrt{\frac{\rho_p}{\rho_p g h_{F_{max}}}} = \dot{\gamma} d_p \sqrt{\frac{1}{g h_{F_{max}}}} \tag{3.7}$$

where $\dot{\gamma}$ is the applied strain rate, d_p is the particle diameter, g is the gravitational acceleration, and $h_{F_{max}}$ is the penetration depth at maximum force.

A first attempt consisted in plotting $\log(Str^*)$ versus $\log(I)$ and applying a linear fit. As shown in Fig. 3.20, the experimental points display a clear linear trend, with $R^2 = 0.7858$. However, the data are separated by binder type along the vertical axis, indicating that viscosity must explicitly enter the formulation of Str to achieve a better data collapse.

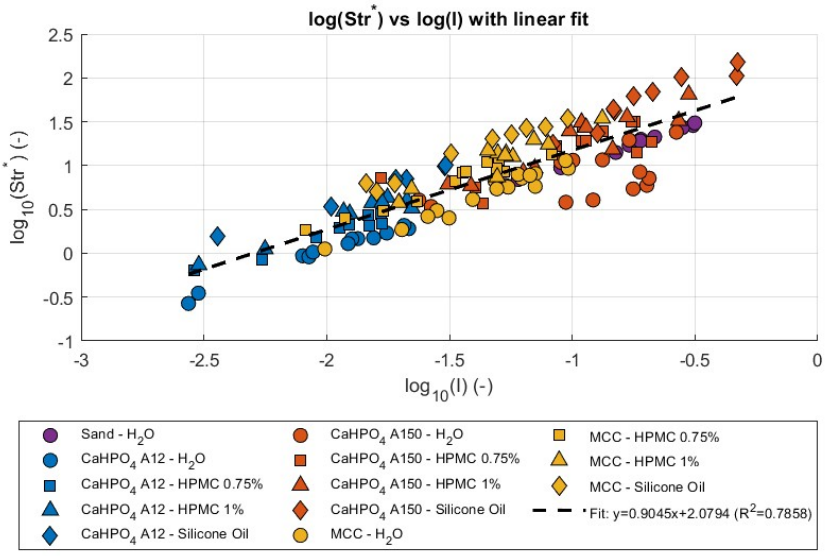

FIGURE 3.20: $\log(Str^*)$ vs $\log(I)$

The most rational choice to account for binder viscosity was to use the Capillary number Ca, as it explicitly depends on η:

$$(Str^*)^{\alpha} \cdot Ca^{\beta}$$

where $Ca = \frac{\eta\dot{\gamma}d_p}{\gamma\cos\theta}$ (variables and assumptions are explained in Chapter 3.6) and α and β are unknown exponents. A Matlab® code was used to determine the optimal values of α and β by maximizing the coefficient of determination R^2.

Two nested loops were employed: each incremented one of the coefficients, and for each combination the R^2 of the linear relation between $\log[(Str^*)^\alpha \cdot Ca^\beta]$ and $\log(I)$ was calculated and stored. A surface was then generated to identify the coefficient pair producing the best linear collapse of the data.

The resulting surface is shown in Fig. 3.21. The point $(0, 0)$ was removed to avoid an artificial perfect collapse.

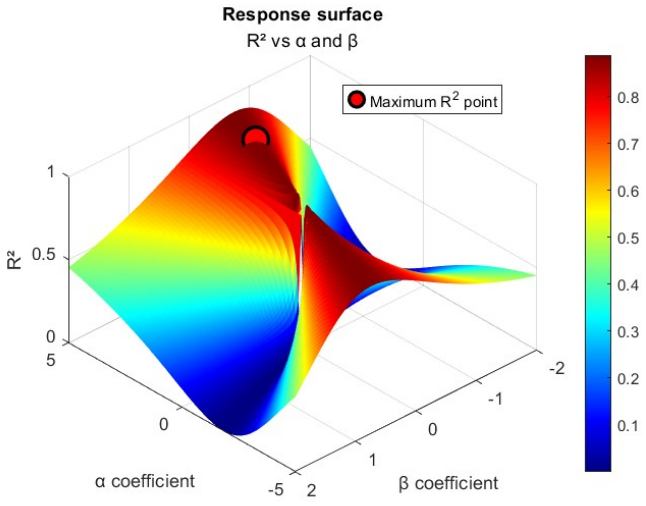

FIGURE 3.21: R^2 as a function of α and β

The optimization results allow several observations.

Even though a maximum is found at $(\alpha, \beta) = (3.4, -0.5)$ with $R^2 = 0.889$, this maximum is not sharp. Many coefficient pairs yield R^2 values close to the maximum, indicating a strong interrelation between α and β, which reflects the correlation between Str^* and Ca previously discussed in Chapter 3.6.

It is also noteworthy that the best coefficients always have opposite signs, indicating an inverse relationship between Str^* and Ca.

For easier visualization, the response surface was collapsed into a contour plot (Fig. 3.22), where the axes represent the coefficients and the color indicates R^2. Only positive values of α are shown, as they are physically meaningful (implying that higher resistance to deformation occur when I that depend on shear is increased). The maximum R^2 is highlighted as a red dot, and a magenta line fits the locus of maximum points ($R^2_{fitted\ line} = 0.994$).

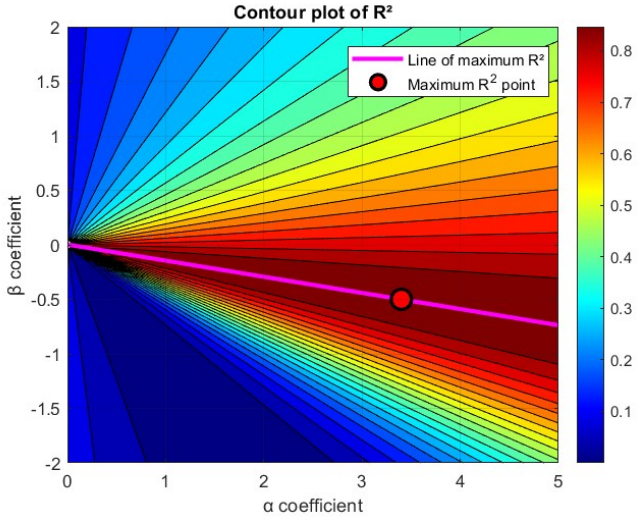

FIGURE 3.22: Contour plot of R^2 for different coefficient pairs.

From Fig. 3.22, it is evident that β has a small range of positive effect, indicating that the contribution of Ca is minor but still necessary for the collapse of data against I. The magenta line, $\beta = -0.148\alpha + 0.003$, represents the ridge of maximum R^2, the high $R^2_{fitted\ line}$ highlight that there is a strong interdependence between Str^* and Ca this arises partly from an intrinsic correlation between the two variables.

A physically motivated interpretation of the coefficients α and β is needed, since an infinite number of combinations can lead to an apparently good data collapse, as shown in Fig. 3.22. For instance, one may impose that α and β remain finite and of comparable magnitude, that their sum equals one ($\alpha + \beta = 1$), or that the exponents satisfy specific quadratic or cubic relationships.

Some representative pairs include:

- $\alpha = 1$, $\beta \approx -0.15$;
- $\alpha = 1.15$, $\beta = -0.15$, even if this combination does not correspond to the point of maximum R^2;
- $\alpha = \frac{3}{2}$, $\beta \approx -\frac{1}{4}$;
- $\alpha = \frac{5}{2}$, $\beta \approx -\frac{1}{3}$;
- $\alpha = 3$, $\beta \approx -\frac{1}{2}$.

Choosing among these combinations primarily affects the intercept and slope of the final relation between $\log[(Str^*)^\alpha \cdot Ca^\beta]$ and $\log(I)$. For stability in the fitting procedure, $\alpha = \frac{5}{2}$ and $\beta = -\frac{1}{3}$ were selected, as they lie in a zone in which R^2, is high even if α and β slightly change, avoiding sensitivity to fluctuations (can be seen in Fig.3.22).

The resulting corrected relationship is shown in Fig. 3.23.

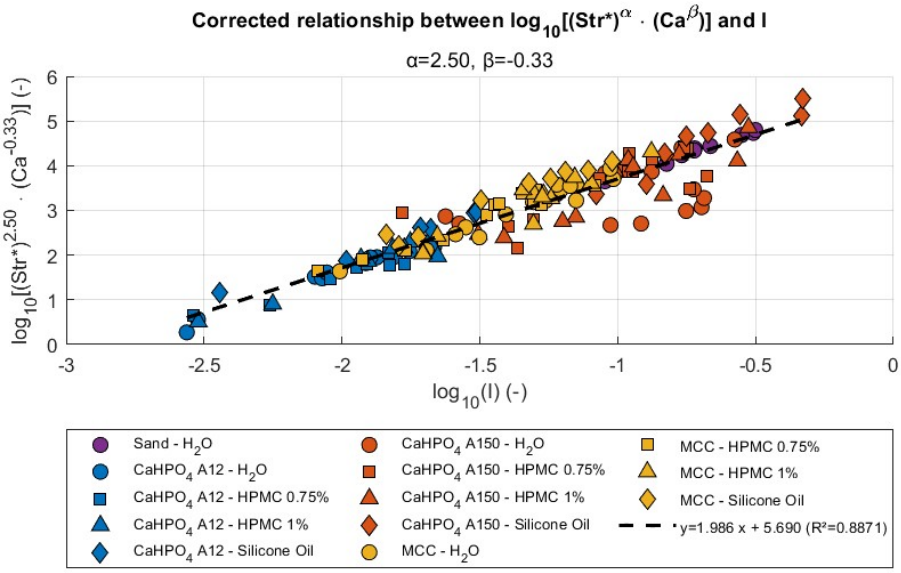

FIGURE 3.23: Corrected relationship between $\log[(Str^*)^\alpha \cdot Ca^\beta]$ and $\log(I)$

The analytical expression is

$$\log[(Str^*)^{2.5} \cdot Ca^{-0.33}] = 1.986 \cdot \log(I) + 5.69 \tag{3.8}$$

with the resulting coefficient of determination $R^2 = 0.8871$, improved of 0.1 over the uncorrected case (Fig.3.20).

It is interesting to repeat the same analysis at the point of maximum velocity, in order to investigate the relative contributions of forces at different stages of indentation. This point occurs shortly after the impact of the indenter.

At this stage, shear rate, hardness, indenter position, and viscosity (for shear-thinning fluids) differ from those at the point of maximum force.

The resulting optimization surface, as well as the line connecting the maximum points, are shown in Fig. 3.24(a-b), where only positive values of α are displayed. Overall, the shape of the retrieved response surface is similar to that in Fig. 3.21, with a maximum $R^2 = 0.9285$ at $\alpha = 3.6$ and $\beta = -0.55$. The magenta line (in Fig. 3.24(b)) representing the maximum points is also very similar, $\beta = -0.1531, \alpha + 0.0013$, with $R^2_{\text{fitted line}} = 0.9952$.

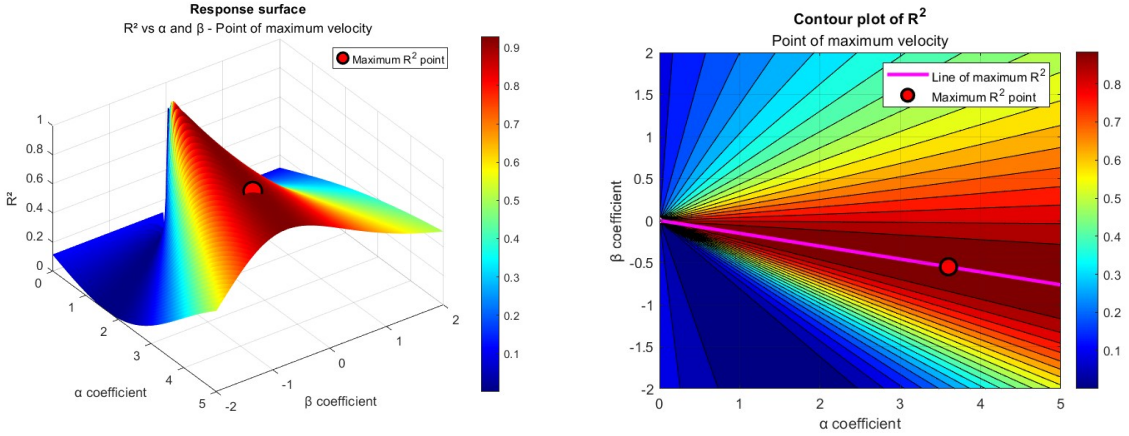

(a) Response surface

(b) Contour plot of R^2

FIGURE 3.24: Response surface and contour plot of R^2 in the point of maximum velocity

This indicates that the coefficients α and β can be considered the same at different stages of indentation.

The small differences observed between the two maximum-peak lines can, for now, be attributed to experimental uncertainty. A more thorough investigation would require a parametric study evaluating the relationship between α and β throughout the entire indentation process.

As in the previous case, multiple coefficient combinations are possible. For simplicity, and robustness the same values are retained here: $\alpha = \frac{5}{2}$ and $\beta = -\frac{1}{3}$.

The result is shown in Fig.3.25.

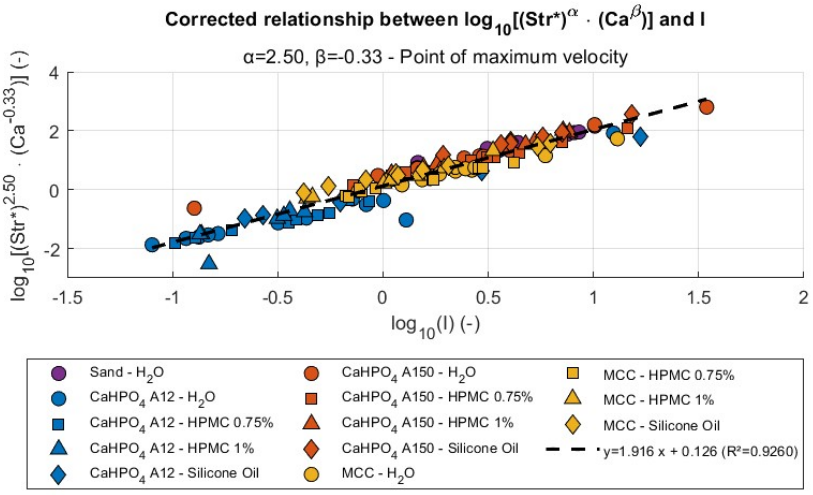

FIGURE 3.25: Corrected relationship between $\log[(Str^*)^\alpha \cdot Ca^\beta]$ and $\log(I)$, in the maximum velocity point

The fact that the coefficients are the same suggests that, at least at these two points, the relative contributions of Str^* and Ca are comparable, and that the viscosity correction remains significant even during the initial phases of indentation. What changes is the analytical expression of the linear fit, which becomes:

$$\log[(Str^*)^{2.5} \cdot Ca^{-0.33}] = 1.916 \cdot \log(I) + 0.126 \tag{3.9}$$

with $R^2 = 0.9260$, highlighting an optimal alignment of the data, (even better than at the point of maximum force).

The retrieved function provide a clearer understanding of the forces acting in the wet bulk. This new representation, based on both Ca and I, captures variations in consolidation pressure and saturation regime more accurately. In contrast, the previous representation (Fig. 3.17) required averaging both consolidation pressure and binder content to obtain a satisfactory correlation. Furthermore, the present function appears independent of PSD and particle aspect ratio, as no corrections based on these parameters are needed, unlike the relation by M.L. Sweat (Fig. 3.16) (Sweat et al., 2016, 2017) for Iveson and co-workers correlation.

Furthermore, comparing Fig. 3.20 and Fig. 3.25, it can be observed that the values along the abscissa differ significantly. At the very beginning, when the ball first impacts the powder bed, the system is in the collisional regime, with $I > 10^{-1}$, indicating an inertia-dominated response. As indentation progresses, I decreases, and the system transitions toward intermediate and quasi-static regimes. This highlights a key feature of the Dynamic Ball Indentation (DBI) method: it allows the investigation of the entire indentation profile and the evolution of mechanical regimes throughout the process.

Despite the improved data collapse with respect to 3.17, the true significance of this new relation is that it allows the powder force to be described not only by capillary and viscous effects but also by inertial contributions.

From the regression shown in Fig. 3.23, corresponding to the relation at maximum Force point

$$\log_{10}\left[(Str^*)^{2.5} Ca^{-0.33}\right] = 1.986 \log_{10}(I) + 5.69, \tag{3.10}$$

an empirical power-law dependence can be derived:

$$2.5 \log_{10}(Str^*) - 0.33 \log_{10}(Ca) = 1.986 \log_{10}(I) + 5.69$$

$$\log_{10}(Str^*) = \frac{1.986}{2.5}\,\log_{10}(I) + \frac{0.33}{2.5}\,\log_{10}(Ca) + \frac{5.69}{2.5}$$

$$\log_{10}(Str^*) \approx 0.794\,\log_{10}(I) + 0.132\,\log_{10}(Ca) + 2.276$$

$$Str^* = 10^{2.276}\,I^{0.794}\,Ca^{0.132} \approx 189\,I^{0.80}\,Ca^{0.13}$$

$$Str^* \approx 189\,I^{0.80}\,Ca^{0.13} \tag{3.11}$$

The visual result is reported in Fig. 3.26, where Str^* is plotted against $I^{0.80} \cdot Ca^{0.13}$ in logarithmic scales. The black dashed line represents the proposed analytical relation, $Str^* \approx 189\,I^{0.80}\,Ca^{0.13}$. The model shows an excellent agreement with the experimental data, with an $R^2 = 0.9221$, indicating that the new definition captures about 92% of the experimental variance. Overall, nearly all data points collapse onto a single master curve.

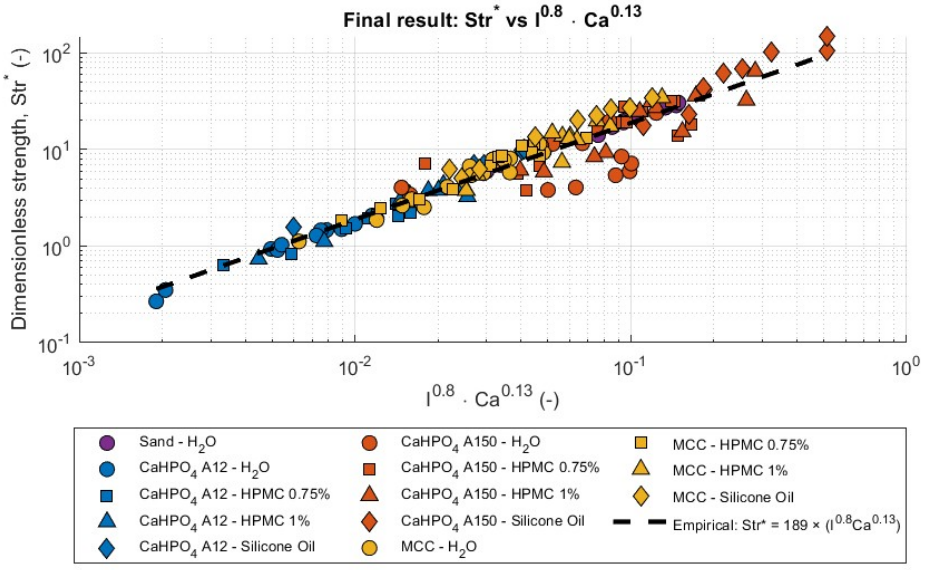

FIGURE 3.26: Str^* vs $I^{0.80} \cdot Ca^{0.13}$

The relatively large exponent associated with I (~ 0.8) in Eq.3.11, indicates that inertial effects dominate the mechanical response of wet powders. In practice, this means that as deformation becomes faster, particle collisions and local rearrangements increasingly contribute to the strength of the bed, leading to a sharp rise in resistance against indentation.

On the other hand, the weak but positive dependence on Ca (~ 0.13) reveals that viscous–capillary forces still influence the stress transmission although its role is comparatively secondary.

The fact that experimental data collapse along a single straight line when plotted as Str^* versus $I^{0.8} \cdot Ca^{0.13}$ confirms that the retrieved combination of parameters captures the essential physics of the system. It implies that the mechanical strength of wet powders under dynamic loading can be expressed through a single scaling law that simultaneously accounts for inertial and viscous–capillary forces.

In summary, the obtained scaling:

$$Str^* \propto I^{0.8}\, Ca^{0.13} \tag{3.12}$$

highlights that both inertial and capillary mechanisms contribute to the overall resistance of the wet bed, with inertia playing the leading role.

This finding provides a new quantitative framework for interpreting wet powder strength data, showing that capillary effects alone cannot account for the measured dimensionless strength, as suggested in literature. Instead, Str^* emerges from the combined contribution of inertial and capillary mechanisms, linking localized indentation behavior to the macroscopic flow response typically observed in wet granulation systems.

Chapter 4

Flowability analysis of dry powders

This chapter investigates the possibility of applying the Dynamic Ball Indentation (DBI) method to assess powder flowability.

To this aim, flow functions obtained from DBI are compared against the benchmark results provided by shear cell testing. The chapter is structured as follows: after a brief overview of the concept of powder flowability, conventional methods of characterization are discussed, followed by the proposed DBI approach and a direct comparison of results.

In this study, nine materials were analyzed, selected in order to span a broad range of physical properties and flowability levels:

- Microcrystalline cellulose (MCC)
- Calcium hydrogen phosphate anhydrous, grade A150 ($CaHPO_4$ A150)
- Calcium hydrogen phosphate anhydrous, grade A12 ($CaHPO_4$ A12)
- Lactose
- Maltodextrin
- Chestnut flour
- Sodium bicarbonate
- Glass beads silanized with a coating thickness $b = 212$ nm
- Glass beads silanized with a coating thickness $b = 50$ nm

4.1 Flowability definition

Powder flowability is defined as a material's ability to initiate and sustain motion under stress, (Santomaso, 2025). Flowability is a key property in many industrial processes such as mixing, granulation, tableting, and transport of particulate solids.

Several factors influence powder flowability, the most important being:

- Particle size and distribution: smaller particles exhibit higher surface area and increased cohesive forces (e.g. Van der Waals), which typically reduce flowability.
- Particle shape and roughness: irregular or angular particles interlock and resist rearrangement, whereas spherical particles promote easier flow.
- Moisture content: adsorbed water enhances capillary and adhesive forces, decreasing flowability.
- Bulk density and consolidation stress: powders under higher confining stress develop stronger interparticle contacts and higher yield strength.

4.1.1 Flowability characterization methods for powders

Several methods exist to characterize powder flowability, they are divided in direct and indirect methods.

Direct methods are the most used and reliable, they are more complete than the indirect one, but on the other hand are more expensive because of the sophisticated machines needed, and they are more labor intensive, they are based on measuring the mechanical response of the powder under applied forces.

The shear cell is the most used direct method in industry, it allows to predict the flowability of powders in a consolidation range $[1, 10]kPa$.

On the other hand indirect methods are less used and reliable, usually they allow to discriminate into a smaller range of flowability, but they are easier and less time consuming, furthermore they do not require investments since they are performed without complex machinery. Indirect tests are mainly empirical, and although they provide a first-order estimation of powder flowability, they do not account for the effect of consolidation stress, particle size distribution, or interparticle interactions. As a result, their predictive capability is limited, especially when powders are subjected to processing conditions different from those of measurement.

Examples of indirect methods are, the angle of repose, the Carr's Index, the Hausner ratio and the packing ratio.

For this reason, direct methods remain the benchmark for industrial applications. Among them, the shear cell has become the standard because it provides the flow function of a powder, i.e., the relation between unconfined yield strength and consolidation stress. This allows a quantitative assessment of flowability and its classification into cohesive, easy-flowing, or free-flowing powders.

However, shear cell testing also has limitations: it is time-consuming, requires relatively large sample quantities, and cannot be applied to saturated powder. In addition, it has a lower operating limit in terms of consolidation stress (typically around $1\,kPa$). This constraints are particularly critical in the pharmaceutical industry, where sometimes just a few grams of powder are available and knowledge of powder flowability at very low compaction stresses is essential for tableting operations.

4.2 Flow Function and Shear Cell Methods

The shear cell measures powder flowability under controlled consolidation by identifying the stress conditions at which failure occurs.

A general representation of the failure dynamic is shown in Fig 4.1, powder under confinement is consolidated by a stress $\sigma_{1_{cons}}$, that is the major principal consolidation stress, then the walls are removed and a different stress is applied, the stress that lead to the failure of the powder is called unconfined yield stress, f_c.

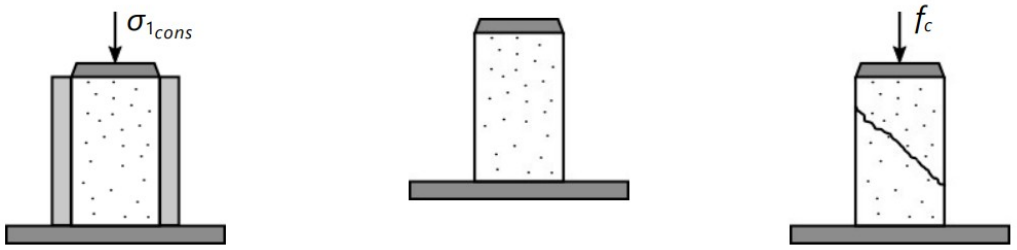

FIGURE 4.1: Failure of unconfined powder

As said previously in this chapter, flowability of powder is not only a function of their intrinsic nature, but also of its consolidation, this means that $f_c = f(\sigma_{1_{cons}})$, a qualitative example is presented in Fig 4.2, the higher the unconfined yield strength, the greatest the cohesive nature of the powder, meaning that it can resist to higher stress before starting to flow.

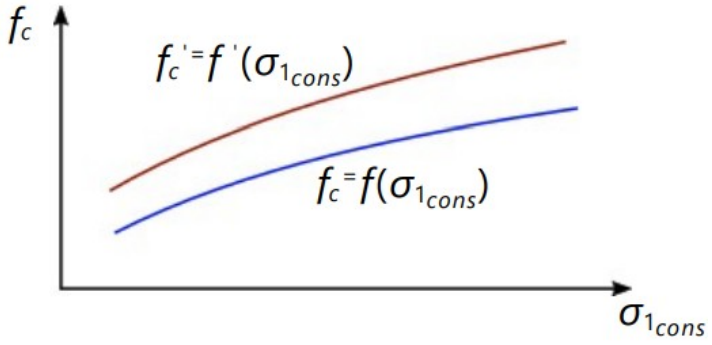

FIGURE 4.2: Example of flow functions

Figure 4.3 illustrates the operating principle of a shear cell test. The graph on the left shows the evolution of shear stress applied (τ) over time during a series of controlled tests at constant normal stress (σ). Each test begins with a preshear phase under high consolidation stress (σ_{pre}) to reach a steady state condition in order to eliminate internal tensional states.

Subsequent shear tests are performed at lower normal stresses (σ_{sh}), and each produces a peak shear stress to failure. These peak values define a set of shear points, which are plotted on the τ-σ plane shown in the right part of the figure.

By fitting these points, an internal yield locus is constructed (IYL). This curve represents shear-normal stresses that applied to the powder lead to yielding.

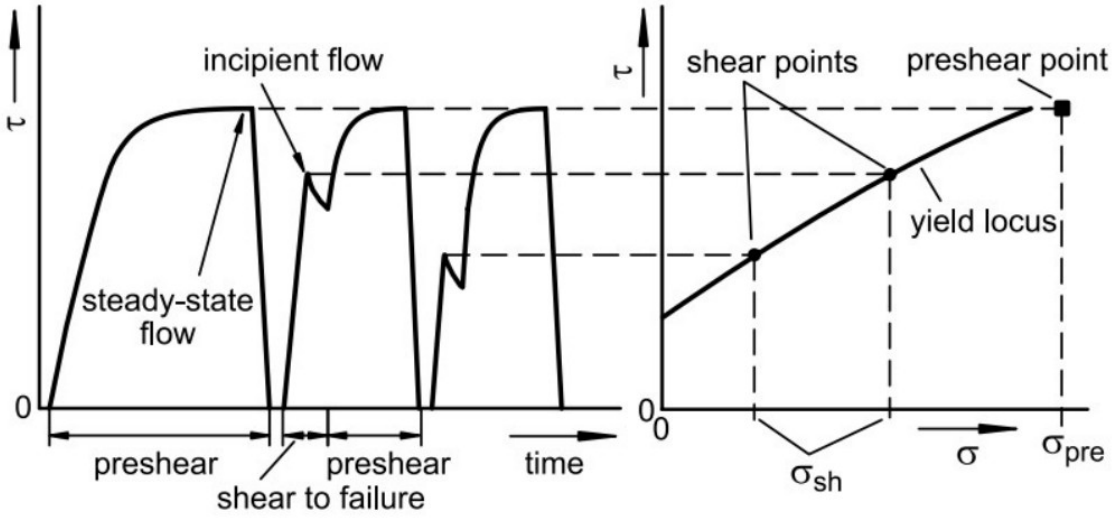

FIGURE 4.3: Schematic representation of a typical shear cell test. Left: shear stress evolution over time during preshear and subsequent shear-to-failure tests under different normal stresses. Right: corresponding yield locus construction from peak shear stresses,(from, Schulze (2008))

The IYL is well described by the Coloumb's law:

$$\tau = \mu_f \sigma + c \tag{4.1}$$

where $\mu_f = tan\phi$ is the coefficient of internal friction, and c is the cohesion of the powder, determined as the intercept of the yield locus.

Once the yield locus is constructed, two Mohr's circles are drawn to determine the stress state at failure and the major principal stress, an example is shown in Fig. 4.4.

The first circle tangent to the yield locus and passing through the origin defines the unconfined yield strength (f_c), the second one the circle tangent to the steady-state point (preshear point) from which is retrieved the consolidation stress identified as the major principal stress (σ_1).

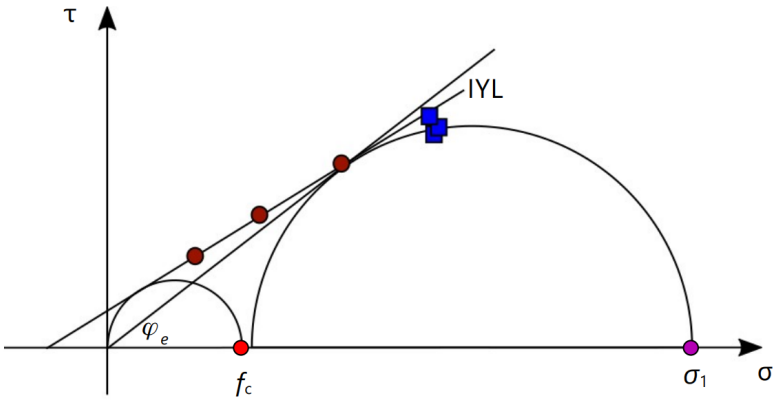

FIGURE 4.4: Example of Mohr's circles

The flow factor coefficient (ff_c) is then defined as the ratio between the major principal stress and the unconfined yield strength:

$$ff_c = \frac{\sigma_1}{f_c} \tag{4.2}$$

4.3 Dynamic ball indentation approach

From recent studies, (Santomaso, 2025), dynamic ball indentation represents an alternative method to study powder behavior under stress, in order to build the flow function of a powder. For retrieving the flowability from DBI we need to start from the extraction of the hardness (H) that is the resistance of the bed against localized deformation, as described in chapter 2.4.2.

Once the Hardness has been retrieved is possible to relate it to macroscopic flowability, by means of the constraint factor (C).

The constraint factor connects the hardness to the uniaxial yield strength f_c as:

$$H = C \cdot f_c \tag{4.3}$$

Is not yet well defined what impact on C and what are the values that it assumes, in literature as reported by Molerus (Molerus, 1975) for cohesive powders or by Tabor (Tabor, 2000) for ductile metals, the resistance to plastic deformation can be approximated to three times the material unconfined yield strength, meaning that for materials with minimal elastic recovery the constraint factor will be close to 3, this value has been confirmed for bicarbonate and ceramic powders in Santomaso's work, Santomaso (2025).

However, not for all the powder the latter remains true, Wang et al. in their work, (Wang et al., 2008) found that the constraint factor for three different pharmaceutical powders was not always equal to 3, in detail for lactose $C \approx 6$, the same results has been obtained by Zafar et al (Zafar et al., 2021), in which using Hardness from ball indentation and unconfined yield stress from shear cell a range of constraint factor varying from 2 to 7 has been retrieved, this is probably due to the inner characteristics of the powder that can deform plastically or exhibit a more elastoplastic behavior, impacting on the constraint factor value.

In order to compare the consolidation pressure of the indentation samples with the major principal consolidation stress of shear cell, it is assumed that in the upper powder layers of the bed, where indentation occurs, axial stresses are negligible due to the limited influence of wall effects. In this region, the vertical stress σ_z can be considered representative of a principal stress aligned with the applied load, while the perpendicular stresses σ_x and σ_y are expected to be small or close to zero, since no lateral loads are applied. Minor non-zero contributions may arise from friction at the cylinder walls, but these are minimized by the use of the Teflon cylinder. Although the stress distribution near the loading plate can be locally complex because of friction and stress concentrations, σ_z at the top surface remains the dominant stress. This allows σ_z to be reasonably approximated as the major principal stress governing deformation, making it directly comparable with shear cell results, where flow functions are expressed in this term, (Santomaso, 2025).

The method proposed in this thesis introduces a novel approach compared to those available in literature, as it allows for the decoupling of DBI from shear cell testing in

the determination of the constraint factor. This represents the first attempt to construct powder flow functions relying solely on DBI data.

The rationale builds on the definition of flowability, understood as a material's ability to initiate and sustain motion under stress. A key advantage of DBI is the possibility of extracting the entire hardness profile during indentation. The initial hardness can be associated with the onset of motion, while the hardness at later stages can be linked to the ability to sustain motion. Based on this reasoning, two characteristic points of the hardness curve were selected: the hardness at maximum force ($H_{F_{max}}$) and the hardness at maximum velocity ($H_{v_{max}}$). The former is related to the sustained response of the material, while the latter corresponds to the early stage of motion initiation.

Traditionally, the constraint factor C is obtained by combining hardness from DBI with the unconfined yield strength f_c derived from the shear cell, according to the relation:

$$C = \frac{H_{F_{max}}}{f_c} \tag{4.4}$$

This approach, however, requires two distinct experimental setups and inherits the limitations of shear cell testing.

Since the approach proposed here is novel, no theoretical or experimental framework exists in the literature.

Therefore, different analytical formulations were tested to obtain a meaningful definition of C, comparing the results against flow functions derived from shear cell experiments.

The simplest and most effective definition obtained is:

$$C = \beta \cdot \frac{H_{v_{max}}}{H_{F_{max}}} \tag{4.5}$$

where β is a dimensionless coefficient optimized by minimizing the mean squared error (MSE) between the shear cell flow function and a linear regression through the DBI-derived values.

The optimization yielded $\beta = 9$. This coefficient is dimensionless, since in Eq. 4.5 the hardness values themselves provide a natural way to make C dimensionless.

Values of $H_{v_{max}}$, $H_{F_{max}}$, and the corresponding constraint factors C obtained either purely from DBI or in combination with shear cell data are reported in Table 4.1.

TABLE 4.1: Mean values of $H_{v_{max}}$, $H_{F_{max}}$, DBI C, and traditional C for different powders and consolidation pressures.

Material	**Pressure [kPa]**	**Mean $H_{v_{max}}$ [kPa]**	**Mean $H_{F_{max}}$ [kPa]**	**C (DBI)**	**C (Traditional)**
Bicarbonate	1	4.2833	77.044	17.371	4.897
Bicarbonate	5	3.6217	81.649	18.625	2.445
Bicarbonate	9	3.3076	81.913	21.779	1.959
$CaHPO_4$ A12	1	2.7689	170.03	3.549	3.165
$CaHPO_4$ A12	5	1.5530	272.10	2.843	2.196
$CaHPO_4$ A12	9	1.2724	322.68	3.094	1.835
$CaHPO_4$ A150	1	3.9472	103.86	6.291	11.334
$CaHPO_4$ A150	5	1.7720	162.19	5.376	14.202
$CaHPO_4$ A150	9	1.5219	186.98	6.599	8.639
Chestnut flour	1	3.3880	111.70	10.157	2.322
Chestnut flour	5	1.6998	210.04	4.796	2.710
Chestnut flour	9	1.3771	247.05	6.012	2.411
Lactose	1	1.7141	179.94	8.728	8.161
Lactose	5	0.9989	311.83	4.585	7.058
Lactose	9	0.8532	339.07	8.028	5.650
MCC	1	3.1706	128.04	6.596	3.374
MCC	5	1.4783	259.24	3.385	3.847
MCC	9	1.1682	309.14	3.031	3.396
Maltodextrin	1	3.8386	101.76	9.559	5.430
Maltodextrin	5	1.7481	185.01	6.396	5.866
Maltodextrin	9	1.5836	204.17	5.180	4.062
Silanized b=212nm	1	1.9186	136.86	11.371	19.039
Silanized b=212nm	5	1.7398	143.98	17.209	10.625
Silanized b=212nm	9	1.7813	149.22	8.350	7.022
Silanized b=50nm	1	4.9792	159.70	9.655	10.231
Silanized b=50nm	5	4.9259	107.45	13.446	2.349
Silanized b=50nm	9	4.7470	111.68	15.696	1.317

In Fig. 4.5 a direct comparison is shown with a parity plot, between the constraint factor C obtained solely from the DBI method (Eq.4.5) and the traditional values derived from combining DBI and shear cell data (Eq.4.4). The dashed reference line represents the ideal case where the two approaches coincide, providing a visual benchmark for evaluating the agreement between methods. Furthermore error bars, provide an estimate of the uncertainty of the measured value.

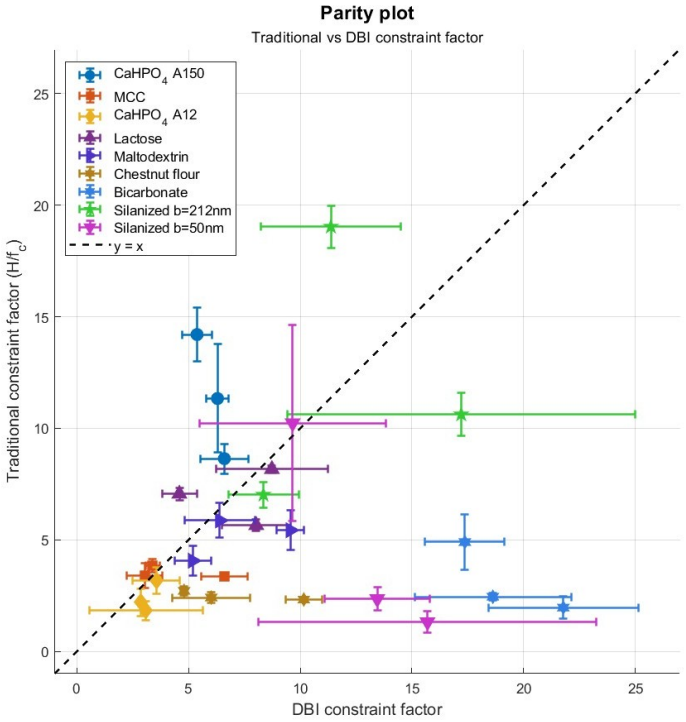

FIGURE 4.5: Comparison between constraint factor C obtained purely from DBI and the traditional C values (DBI + shear cell). The dashed line indicates the ideal 1:1 correspondence.

Overall, the agreement between the two approaches is satisfactory, confirming the robustness of the proposed method. However, noticeable deviations are observed for silanized glass beads, bicarbonate, and $CaHPO_4$ A150, where the traditional and DBI-derived C values differ more significantly. Interestingly, these materials are also the most free-flowing of the set, suggesting that reduced cohesiveness may accentuate the discrepancy between the two methods.

Furthermore, the error bars highlight that the uncertainty in measuring C with the proposed method is generally low, especially for values along the parity line. The highest error values correspond to silanized beads, possibly due to their unique characteristics compared to less "ideal" materials.

4.3.1 Stability of β

The stability of the 9 value used as a unique coefficient was assessed by analyzing the mean squared error (MSE) curves as a function of β. Figures 4.6 and 4.7 show the behavior: the optimal coefficient (β_{opt} corresponding to the minimum MSE) is marked in green, while the selected value $\beta = 9$ is highlighted in red.

There are 3 different shapes of this function, Fig.4.6(a-d), in which there is a clear minimum, between $\beta_{opt} = [4-10]$. For some powders [Figs. 4.7(a–d)], the curve presents a minimum followed by an asymptotic trend, meaning that $\beta = 9$ still provides a low error even if the optimum lies at higher values (e.g., $CaHPO_4$ A150 with $\beta_{opt} \approx 15.6$). The only exception is sodium bicarbonate [Fig. 4.7(e)], where the optimal value is close to $\beta_{opt} = 1$. Nevertheless, in this case the MSE remains consistently low across the tested range, so adopting $\beta = 9$ does not significantly increase the error.

Overall, these results demonstrate that the proposed formulation of C is robust across different powders, with $\beta = 9$ providing a stable compromise between DBI and shear cell flow functions.

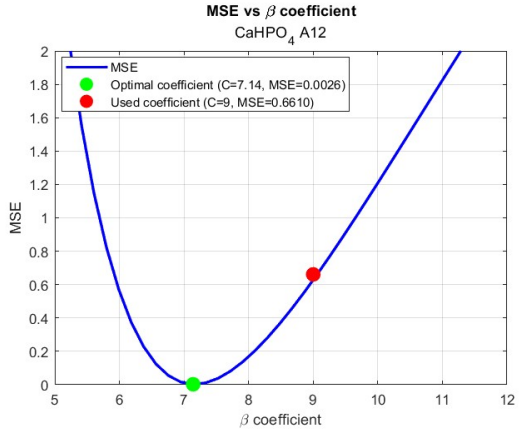

(a) $CaHPO_4$ A12

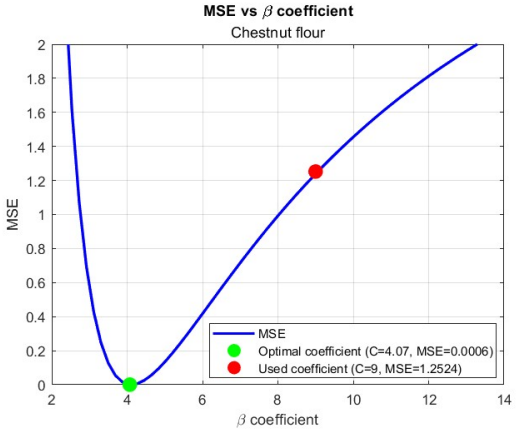

(b) Chestnut flour

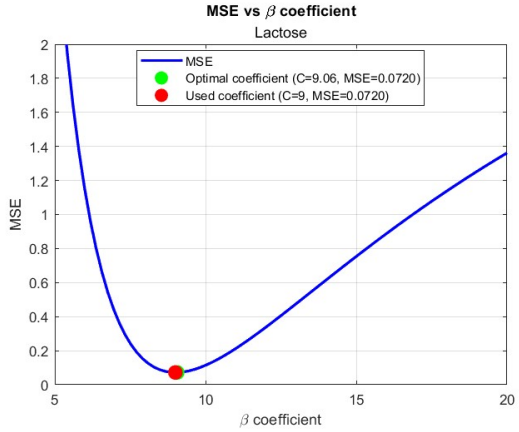

(c) Lactose

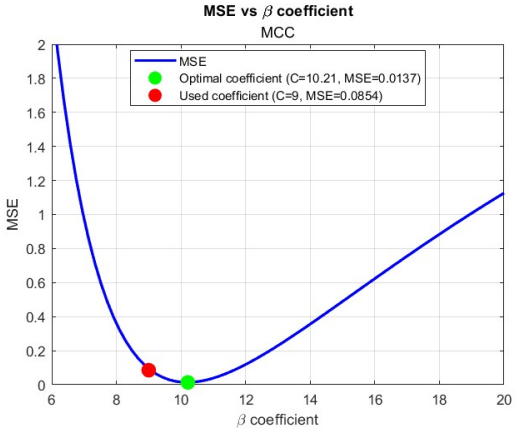

(d) MCC

FIGURE 4.6: MSE vs β coefficient for various powders

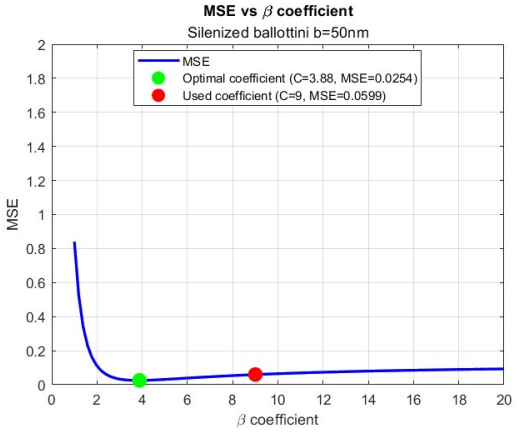

(a) Silanized ballottini b=50nm

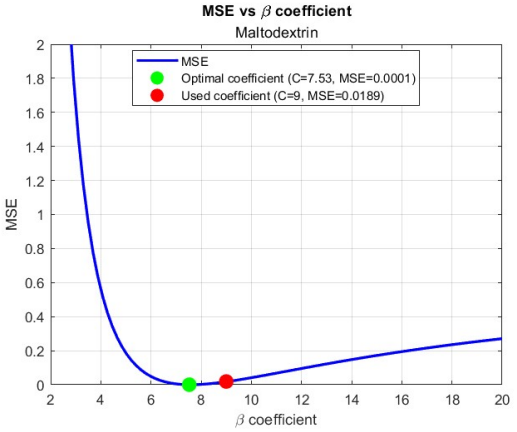

(b) Maltodextrin

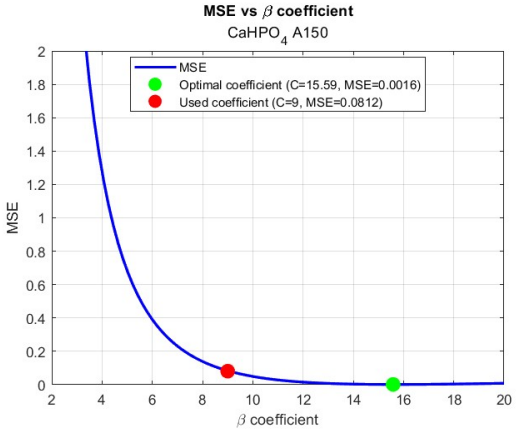

(c) $CaHPO_4$ A150

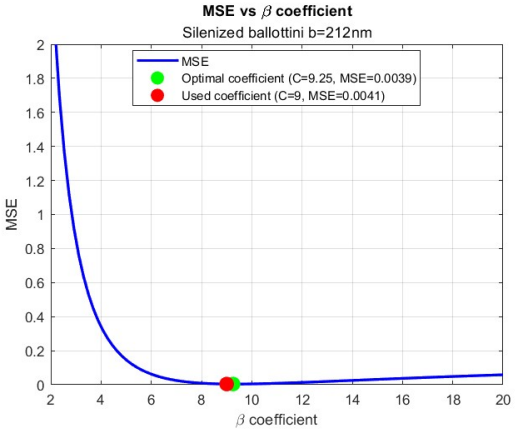

(d) Silanized ballottini b=212nm

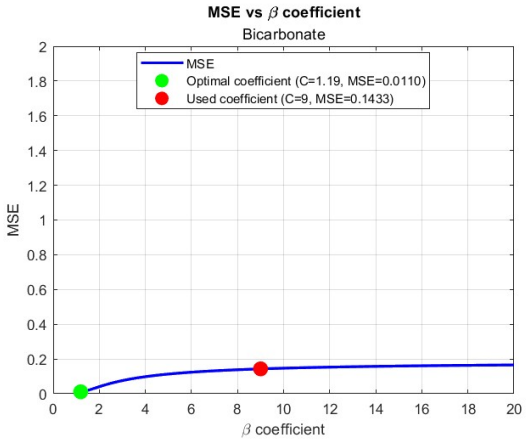

(e) Bicarbonate

FIGURE 4.7: MSE vs β coefficient for various powders

4.3.2 Comparison with shear cell flow function

After analyzing the stability of the coefficient, Figs. 4.8 and 4.9 compare the flow functions obtained with the DBI method against those measured with the shear cell, which is taken as the benchmark reference.

The figures are arranged from the most cohesive to the most free-flowing powders. The blue line represents the flow function measured with the shear cell, carried out in parallel with the DBI tests to ensure identical humidity conditions, since moisture strongly affects flowability.

In 7 out of 9 cases, the flowability classification obtained from DBI (with the new proposed method) agrees with the shear cell results. In two cases [Figs. 4.8(c) and 4.9(a)], a misclassification occurs, although the discrepancy is not large.

It is worth noting that the agreement is generally better at $\sigma_1 = 1\,\mathrm{kPa}$, where DBI predictions are more accurate and the errors smaller, compared to higher consolidation stresses.

Only two datasets [Figs. 4.8(a) and 4.8(b)] show significant error bars. Interestingly, these correspond to the most cohesive powders. This suggests that the increased variability may be linked to the cohesive nature of the material, although further investigations would be required to confirm this hypothesis.

Furthermore can be highlighted the fact that even if C error, represented by the error bars along the x axis in the parity plot, (Figure.4.5) are in some cases significant (e.g.silanized Ballottini), the error bars of f_c in the flow functions is low, this can be due to an error reduction when f_c is calculated as $f_c = \frac{H_{F_{max}}}{C}$.

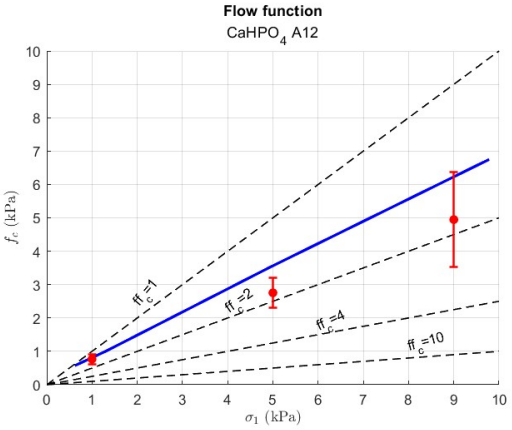

(a) $CaHPO_4$ A12

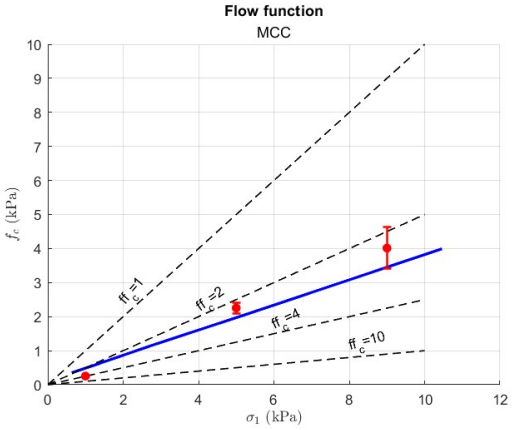

(b) MCC

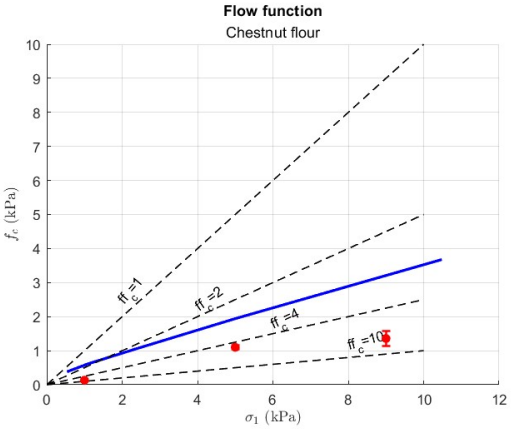

(c) Chestnut flour

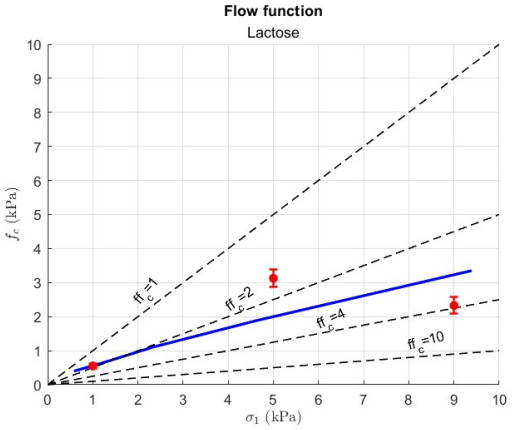

(d) Lactose

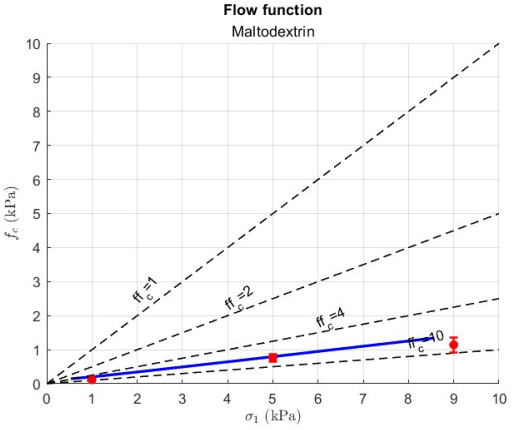

(e) Maltodextrin

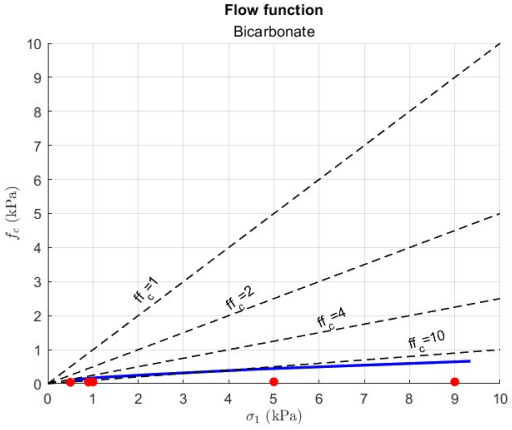

(f) Bicarbonate

FIGURE 4.8: Flow functions comparison, between shear cell (in blue) and DBI (red, with error bars)

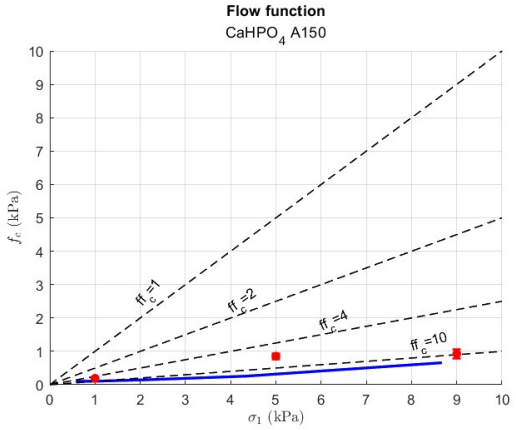

(a) $CaHPO_4$ A150

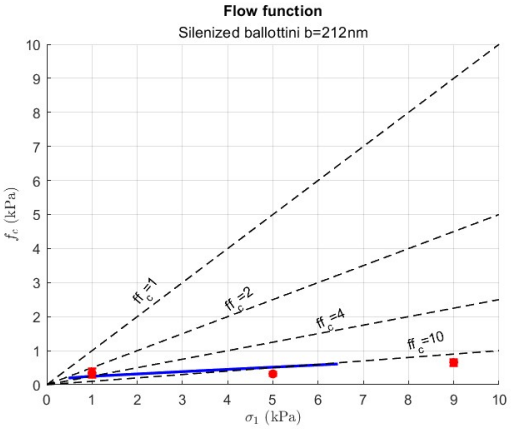

(b) Silanized ballottini b=212nm

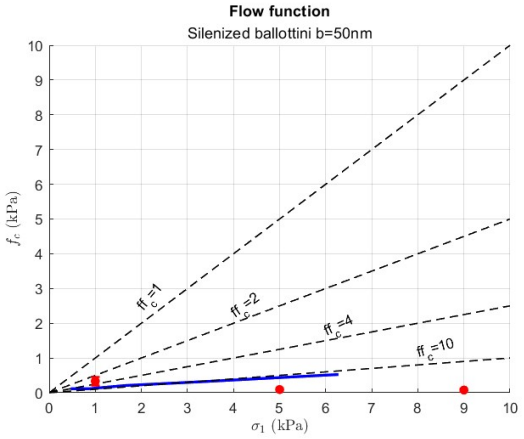

(c) Silanized ballottini b=50nm

FIGURE 4.9: Flow functions comparison, between shear cell (in blue) and DBI (red, with error bars)

The results confirm that DBI can be used to construct powder flow functions comparable to those obtained from shear cell testing. Although discrepancies remain to be understood, like the difference of C values for free-flowing powders compared to the constraint factor based on both shear cell and DBI (Fig.4.5), or the uncertainty in the flow functions for highly cohesive powders, the method showed, promise as a fast, less resource-intensive alternative, particularly useful for exploring the role of moisture in powder mechanics.

The possibility to further extend this study to low confinement states could provide a powerful tool in order to asses flowability in consolidation ranges that shear cell cannot study.

Chapter 5

Conclusions

5.1 Summary of main findings

- A qualitative correlation was established between the torque measured with the torque rheometer and the hardness obtained from the DBI method.
- The transition between the quasi-static and the intermediate flow regimes was identified through the inertial number.
- Hardness was found to increase linearly with both strain rate and binder content, leading to characteristic response planes specific to each powder–binder system.
- The Str^*–Ca relationship originally reported by Iveson and co-workers was successfully reproduced using a different technique, by adopting hardness as a measure of the dynamic yield stress σ_D.
- Saturation and consolidation pressure, which were not explicitly accounted for in previous studies, were shown to have a significant impact on the values of Str^* and Ca. A linear dependence between Str^* and Ca was also observed when values were normalized by viscosity.
- A collapse of experimental data was achieved by plotting Str^* against $I^{0.8} \cdot Ca^{0.13}$, highlighting that both the capillary number and the inertial number contribute to the definition of the bulk strength of wet powders. This emphasizes the complementary roles of viscous, capillary, and inertial forces in powder mechanics, improving upon the conventional definition of Str^*, which depends solely on Ca.
- In the study of dry powders, a new analytical definition of the constraint factor was proposed. This definition is grounded in the physical meaning of flowability

and enables the DBI method to reproduce shear cell flow functions effectively, without relying on external calibration.

5.2 Final remarks

This thesis represents the first systematic attempt to apply the Dynamic Ball Indentation (DBI) method to the study of wet powders. Several aspects of novelty emerge:

- For the first time, a qualitative relationship between torque values from torque rheometry and hardness from DBI has been identified.
- DBI has been applied for the first time to powders wetted with liquid binders, enabling a detailed study of binder–powder interactions. The method confirmed previous findings regarding the dependence of powder strength on viscous and capillary forces, while also extending the classical definition by incorporating the significant inertial effects, which contribute to a more complete description of the dynamic forces in wet powders.

Furthermore, the experiments conducted on dry powders demonstrated that the Dynamic Ball Indentation technique can also be used to:

- Perform a direct comparison with flow functions obtained from shear cell testing, entirely based on DBI-derived quantities.
- Propose a new analytical definition of the constraint factor, allowing DBI to reproduce shear-cell flow functions without requiring external calibration.

These results highlight the potential of DBI as an independent and versatile technique, capable of overcoming several limitations of conventional methods. While further validation and refinement are required, the present work demonstrates that DBI can serve as a powerful tool for powder characterization, bridging the gap between established approaches and new perspectives on powder mechanics.

5.3 Suggestions for future work

Several directions can be considered to further advance the development and validation of the Dynamic Ball Indentation (DBI) method:

- **Optimization of the indentation cylinder.** The geometry of the cylinder could be modified so that it is small enough to allow for a single indentation, yet large enough to avoid boundary effects. This would strengthen the idea that DBI can be applied even when only limited sample quantities are available, as is often the case in pharmaceutical testing.

- **Improvement of the compaction procedure.** The current manual loading and unloading of weights introduces operator-dependent variability. A more automated system, such as a texture analyzer, could provide more uniform bed compaction, minimizing heterogeneities in the bulk and reducing the variability of the indentation response.

- **Indentation with spheres of different masses.** By employing balls of different masses, it would be possible to expand the range of strain rates investigated. This would allow characterization of powders at lower Capillary numbers, verifying whether Iveson's granulation curves are reproducible also at low values, and clarifying whether hardness exhibits further regime transitions in the inertial domain, analogous to the change from quasi-static to dense regimes.

- **Comparison with torque measurements.** It would be valuable to confirm the observed parallelism between hardness and torque results, and to determine whether a quantitative relationship can be established between the two variables.

- **Granulation map validation.** Future studies should test whether the dimensionless strength values (Str^*) obtained from DBI correspond to granule formation boundaries as predicted by Iveson's granulation map.

- **Link between Str^*, Ca, and I.** The exact interrelation among the dimensionless strength, Capillary number, and Inertial number remains open. It is important to assess which couple of α and β coefficients are the best to describe Str^* as a function of both Ca and I. Thanks to the availability of full indentation profiles, it would also be interesting to analyze whether their contributions remain constant or vary dynamically during indentation.

- **Extension to low compaction pressures.** Investigations at consolidation pressures below 1 kPa should be performed, entering a regime not accessible to shear cell testing. Additional dry materials should also be tested, particularly those with very high flowability (large flow factors), to further strengthen the conclusions of this thesis.

- **Dependence of the coefficient β in flow function identification.** The nature of the coefficient β requires further study. For example, it may depend on indenter geometry or diameter, which would provide useful design guidelines for the method.

Although several open questions remain, this research has demonstrated that the Dynamic Ball Indentation technique can serve as a single, integrated method capable of characterizing the mechanical response of both dry and wet powders, eliminating the need for multiple instruments.

For wet powders, the introduction of a new relationship linking the dimensionless strength of powder compacts with both capillary and inertial numbers represents a promising step toward a unified framework for predicting granulation behavior.

In the field of dry granular matter the extension to consolidation pressures outside the operational limits of traditional devices positions DBI as a uniquely versatile and forward-looking tool in powder technology.

List of Symbols

A	Area
A_{cap}	Cap Area
a	Acceleration
α	Coefficient to be optimized
β	Coefficient to be optimized
Ca	Capillary number
c	Cohesion
C	Constraint factor
d_{crit}	Critical diameter
d_p	Powder mean diameter
D_b	Ball indenter diameter
$\mathcal{E}_{pore}$	Granule porosity
f_c	Unconfined yield stress
ff_c	Flow factor coefficient
F	Force
F_{cz}	Capillary force
F_g	Gravitational force
F_{max}	Max force
F_{net}	Net force
F_v	Viscous force
g	Gravitational acceleration
γ	Surface tension
γ_{LV}	Surface tension between liquid-vapour phases
γ_{SL}	Surface tension between solid-liquid phases
γ_{SV}	Surface tension between solid-vapour phases
$\dot{\gamma}$	Shear rate
$\dot{\gamma}^*$	Dimensionless shear rate
G_{ads}	Adsorption Gibbs free energy

H	Hardness
$H_{v_{max}}$	Hardness in the point of maximum velocity
$h_{F_{max}}$	Penetration depth in the maximum force moment
I	Inertial number
L	Length
m	Mass
μ_f	Coefficient of internal friction
η	Viscosity
Π	Equilibrium spreading pressure
π	constant $\pi = 3.14$
P	Pressure
ρ	Density
R_b	Ball indenter radius
R^2	Coefficient of determination
R^2_{adj}	Adjusted coefficient of determination
r	Radius
r_c	Capillary radius
S	Liquid saturation
σ	Normal stress
$\sigma_{x,y,z}$	Normal stress in a specific direction
σ_1	Major principal stress
SSA	Specific surface area
St_{def}	Stokes deformation number
Str^*	Dimensionless strength
τ	Shear stress
T	Temperature
t	Time
θ	Contact angle
U_c	Collision velocity
$v_{F_{max}}$	Indenter velocity in the maximum force moment
V	Volume
W	Work
ω	Mass fraction
y_b	Binder mass fraction
Y	Yield stress
Φ	Packing fraction

List of Figures

List of Tables

Bibliography

Cain, R. G., Page, N. W. & Biggs, S. (2000). Microscopic and macroscopic effects of surface lubricant films in granular shear. *Physical Review E* **62**, 8369.

Chitu, T. M., Oulahna, D. & Hemati, M. (2011a). Rheology, granule growth and granule strength: Application to the wet granulation of lactose–mcc mixtures. *Powder technology* **208**, 441–453.

Chitu, T. M., Oulahna, D. & Hemati, M. (2011b). Wet granulation in laboratory scale high shear mixers: Effect of binder properties. *Powder technology* **206**, 25–33.

Doble, M. (1984). *Perry's chemical engineers' handbook*. McGraw-Hill: New York, NY, USA.

Goh, H. P., Heng, P. W. S. & Liew, C. V. (2018). Comparative evaluation of powder flow parameters with reference to particle size and shape. *International journal of pharmaceutics* **547**, 133–141.

Goldman, A. J., Cox, R. G. & Brenner, H. (1967). Slow viscous motion of a sphere parallel to a plane wall—i motion through a quiescent fluid. *Chemical engineering science* **22**, 637–651.

Guo, H., Song, K. & Hilfer, R. (2022). A brief review of capillary number and its use in capillary desaturation curves. *Transport in Porous Media* **144**, 3–31.

Hassanpour, A. & Ghadiri, M. (2007). Characterisation of flowability of loosely compacted cohesive powders by indentation. *Particle & Particle Systems Characterization* **24**, 117–123.

Hurley, R. C. & Andrade, J. E. (2015). Friction in inertial granular flows: competition between dilation and grain-scale dissipation rates. *Granular Matter* **17**, 287–295.

Iveson, S. & Litster, J. (1998). Growth regime map for liquid-bound granules. *AIChE journal* **44**, 1510–1518.

Iveson, S. M., Beathe, J. A. & Page, N. W. (2002). The dynamic strength of partially saturated powder compacts: the effect of liquid properties. *Powder Technology* **127**, 149–161.

Kang, W., Feng, Y., Liu, C. & Blumenfeld, R. (2018). Archimedes' law explains penetration of solids into granular media. *Nature communications* **9**, 1101.

Lazghab, M., Saleh, K., Pezron, I., Guigon, P. & Komunjer, L. (2005). Wettability assessment of finely divided solids. *Powder technology* **157**, 79–91.

Litster, J. & Ennis, B. (2004). *The science and engineering of granulation processes*, vol. 15. Springer Science & Business Media.

MiDi, G. (2004). On dense granular flows. *The European Physical Journal E* **14**, 341–365.

Molerus, O. (1975). Theory of yield of cohesive powders. *Powder Technology* **12**, 259–275.

Navascues, G. (1979). Liquid surfaces: theory of surface tension. *Reports on Progress in Physics* **42**, 1131.

Nicklasson, F. & Alderborn, G. (1999). Modulation of the tabletting behaviour of microcrystalline cellulose pellets by the incorporation of polyethylene glycol. *European journal of pharmaceutical sciences* **9**, 57–65.

Oliver, W. C. & Pharr, G. M. (1992). An improved technique for determining hardness and elastic modulus using load and displacement sensing indentation experiments. *Journal of materials research* **7**, 1564–1583.

Opto Engineering (2025). Opto engineering – optics, cameras, illuminators and software for machine vision. `https://www.opto-e.com/`.

Pasha, M., Hare, C., Hassanpour, A. & Ghadiri, M. (2015). Numerical analysis of strain rate sensitivity in ball indentation on cohesive powder beds. *Chemical Engineering Science* **123**, 92–98.

Prandtl, L. (1920). Uber die harte plastischer korper. *Nachr. Ges. Wissensch, Gottingen, math.-phys. Klasse, 1920* , 74–85.

Rhodes, M. J. (2008). *Introduction to particle technology*. John Wiley & Sons.

Rowe, R. C., Sheskey, P. J., Weller, P. J. et al. (2006). *Handbook of pharmaceutical excipients*, vol. 6. Pharmaceutical press London.

Santomaso, A. C. (2025). Dynamic ball indentation: advancing powder flowability characterization through complete impact dynamics analysis. *Advanced Powder Technology* **36**, 104914.

Santomaso, A. C., Baggio, R., Zorzi, F., Salviulo, G., Realdon, N. & Franceschinis, E. (2017). Sugars with different thickening power in high shear granulation. *Powder Technology* **317**, 391–399.

Schulze, D. (2008). *Powders and bulk solids: behavior, characterization, storage and flow*. Springer.

Sweat, M. L., Parker, A. S. & Beaudoin, S. P. (2016). Compressive behavior of high-viscosity granular systems: Effects of viscosity and strain rate. *Powder Technology* **302**, 480–487.

Sweat, M. L., Parker, A. S. & Beaudoin, S. P. (2017). Compressive behavior of high viscosity granular systems: Effect of particle size distribution. *Powder Technology* **311**, 506–513.

Tabor, D. (2000). *The hardness of metals*. Oxford university press.

Tardos, G. I., Khan, M. I. & Mort, P. R. (1997). Critical parameters and limiting conditions in binder granulation of fine powders. *Powder Technology* **94**, 245–258.

Tirapelle, M., Santomaso, A. C. & Hare, C. (2020). Dynamic ball indentation for powder flow characterization. *Powder Technology* **360**, 1047–1054.

Wang, C., Hassanpour, A. & Ghadiri, M. (2008). Characterisation of flowability of cohesive powders by testing small quantities of weak compacts. *Particuology* **6**, 282–285.

Zafar, U., Hare, C., Hassanpour, A. & Ghadiri, M. (2017). Ball indentation on powder beds for assessing powder flowability: Analysis of operation window. *Powder Technology* **310**, 300–306.

Zafar, U., Hare, C., Hassanpour, A. & Ghadiri, M. (2021). Assessing powder flowability at low stresses using ball indentation method: Evaluation of constraint factor. *Powder Technology* **387**, 287–294.

Zisman, W. A. (1964). Relation of the equilibrium contact angle to liquid and solid constitution. ACS Publications.